Search for Charged Higgs Bosons in Multi-Lepton and Dijet Final States via Vector Boson Fusion with the ATLAS Detector

Haoran Zhao

A dissertation
submitted in partial fulfillment of the
requirements for the degree of

Doctor of Philosophy

University of Washington

2025

Reading Committee:

Shih-Chieh Hsu, Chair

Quentin Buat

Stephen R. Sharpe

Program Authorized to Offer Degree:

Physics

University of Washington

Abstract

Search for Charged Higgs Bosons in Multi-Lepton and Dijet Final States via Vector Boson Fusion with the ATLAS Detector

Haoran Zhao

Chair of the Supervisory Committee:
Shih-Chieh Hsu
Department of Physics

This thesis reports on two independent studies conducted using 140 fb^{-1} of proton–proton collision data at a center-of-mass energy of $\sqrt{s} = 13$ TeV, collected with the ATLAS detector during Run 2 of the Large Hadron Collider.

The first study focuses on the performance and calibration of quark/gluon jet discrimination techniques, which are essential tools for a wide range of physics analyses at the LHC. Two approaches are explored: a track-based tagger and a boosted decision tree combining multiple jet substructure observables. The tagging efficiencies are measured for jets with transverse momentum in the range of 500 GeV to 2000 GeV. Differences between data and simulation are quantified at various working points, and corresponding correction factors are derived to enhance the precision of future physics analyses. The second study presents a combined analysis of searches for singly and doubly charged Higgs bosons, $H^{\pm}$ and $H^{\pm\pm}$, produced through vector boson fusion processes. These searches target decay channels involving massive vector bosons, specifically focusing on fully leptonic final states containing electrons or muons. The analysis sets new limits on the product of the production cross-section and branching fraction for charged Higgs boson masses in the range of 200 GeV to 3000 GeV. The results are interpreted within the framework of the Georgi-Machacek model, establishing the most stringent constraints to date on its parameter space across the probed mass range.

To all those who have supported me on this journey,
whether bound by blood or joined by choice.

Acknowledgments

I would like to express my heartfelt gratitude to the University of Washington, particularly the Physics Department's staff and faculty, for their unwavering support and guidance throughout my academic journey. Their commitment to excellence in education and research has played a pivotal role in shaping my intellectual growth and personal development.

I am profoundly grateful to my research advisor, Shih-Chieh Hsu, whose mentorship has been the cornerstone of my academic journey. His insightful guidance and steadfast support during challenging times have enriched my research and inspired me to persevere and grow both academically and personally.

I would also like to express my sincere appreciation to my mentor, Quentin Buat, for his patience and guidance, which were instrumental in helping me begin my analysis. I am equally thankful to my committee members for their time, thoughtful feedback, and invaluable contributions to improving the quality of my research.

I am deeply appreciative of the postdoctoral researchers I had the privilege of working with: Ke Li, Yuan-Tang Chou, Yue Xu, and Elham Khoda, for their generosity in addressing my questions and sharing their expertise. Their insights have been invaluable throughout my research.

Thanks are due to my fellow graduate students, Alex Schuy, Ali Garabaglu, Charles Lewis, Miles Cochran-Branson and Bayley Burke, for the countless conversations we shared on physics, careers, life, and everything in between. These moments added joy and perspective to my academic journey.

I am especially grateful to the program advisor, Catherine Provost, for her unwavering support during the pandemic and her care during my recovery after surgery. I am also thankful to Marcel den Nijs for his professional academic advice and encouragement, which provided clarity and guidance at key moments.

I extend my sincere thanks to my collaborators in ATLAS, whose collective contributions were indispensable to this thesis: Xiangyang Ju, Daniel Munoz, Aram Apyan, and Wanyun Su. I am also grateful for the opportunity to visit LBNL in the summer of 2022, where I worked with Elisabetta Pianori and Timon Heim, gaining invaluable exposure to the world of electronics and detector operations.

My heartfelt gratitude is extended to my friends both within and beyond the collaboration—including Shan He, Yiyun Dong, Jay Chan, Hao Xu, Zhuolin Zhang, Xiulong Liu, Lang Xu, Kuai Wang, Yi Wu, Ran Xu, Qianni Jiang and many others—for the memorable experiences shared during my Ph.D. journey, from hiking and traveling to everyday moments of support and friendship.

I would like to express my deepest gratitude to my family for their unconditional love, support, and encouragement throughout this journey. Their steadfast belief empowered me to overcome challenges and persevere through difficult times. This achievement would not have been possible without their constant support and sacrifices.

Finally, reflecting on this Ph.D. journey, I am deeply grateful for the many people, challenges, and experiences that have shaped both my academic and personal growth. This chapter of my life has been transformative and unforgettable, and the lessons I have learned will continue to guide me in the years to come.

This work was supported by the following funding sources:

- National Science Foundation Grant No. 2110963: Accelerating Searches for Beyond the Standard Model Physics and the ATLAS Pixel Detector.
- National Science Foundation Grant No. 2117997: HDR Institute: Accelerated AI Algorithms for Data-Driven Discovery (A3D3).
- US ATLAS Center (ATC) Grant No. 339224.

Contents

List of Figures

List of Tables

Chapter 1

Introduction

The discovery of the Higgs boson in 2012 by the ATLAS and CMS collaborations at the LHC [1, 2, 3, 4] marked a significant milestone in particle physics, confirming the last missing piece of the Standard Model (SM). Despite its success, the SM fails to address several fundamental questions, including the lack of a quantum theory of gravity, the nature of dark matter, which constitutes approximately 27% of the universe, and the origin of neutrino masses, which require nonzero Yukawa couplings absent in the SM. These limitations strongly motivate the search for physics beyond the Standard Model (BSM). In particular, extended Higgs sectors provide a compelling framework to address these shortcomings. For instance, models such as Z'+two-Higgs-doublet model (2HDM) [5] and 2HDM+a [6, 7] introduce Higgs portal interactions that offer viable dark matter candidates, while the Type-II Seesaw mechanism, which requires Higgs triplets, provides a natural explanation for neutrino masses [8].

Charged Higgs bosons, a distinctive feature of extended Higgs sectors, emerge in numerous BSM scenarios. These models incorporate additional scalar fields, such as extra Higgs doublets [9, 10] or higher-isospin multiplets [11, 12, 13]. In the 2HDM, a charged Higgs boson, $H^\pm$, is predicted but does not couple to WZ bosons at tree level due to CP invariance, which forbids a $H^\pm W^\pm Z$ interaction [14]. However, models incorporating additional isotriplet scalars, such as the Georgi-Machacek (GM) model [15, 16], allow for tree-level $H^\pm W^\pm Z$ couplings, significantly altering the phenomenology of the Higgs sector.

The GM model extends the SM Higgs sector by introducing one real and one complex isotriplet scalar field, ensuring the preservation of custodial symmetry at tree level. Custodial symmetry, a residual global SU(2) × SU(2) symmetry that remains after the spontaneous breaking of the $\mathrm{SU}(2)_L \times \mathrm{U}(1)_Y$ gauge symmetry, plays a crucial role in maintaining consistency with electroweak precision measurements, particularly constraints on the electroweak ρ parameter [17]. The primary motivation for the GM model is to explore extended electroweak symmetry breaking mechanisms while preserving custodial symmetry. Unlike the SM, where the Higgs sector consists of only a single SU(2) doublet, the GM model incorporates additional scalar fields that allow for a tree-level $H^{\pm}W^{\mp}Z$ coupling, which is absent in 2HDM. This feature significantly alters the phenomenology of the Higgs sector and provides a unique experimental signature in searches for new scalar resonances at the LHC. The GM model predicts new scalar states organized into custodial multiplets, including a quintuplet consisting of $H_5^{\pm\pm}$, $H_5^{\pm}$, and H_5^0, which primarily couple to vector bosons and are fermiophobic. A key parameter, $\sin\theta_H$, determines the contribution of the isotriplet scalars to the W and Z boson masses, with the production cross-sections of the quintuplet states scaling as $\sin^2\theta_H$. At tree level, the physical states within the quintuplet are degenerate in mass, denoted by m_{H_5}. Although higher-order effects can induce small mass splittings, they are not considered in this analysis [18].

In the GM model, the $H_5^{\pm}$ and $H_5^{\pm\pm}$ bosons are produced in association with two quark-jets via the VBF processes. This production mechanism features two forward quark-jets that can be distinguished from gluon-jets, offering a promising avenue to enhance sensitivity. The development of robust quark/gluon-jet discrimination tools plays a critical role in leveraging the VBF topology, and one chapter of this thesis documents my contributions to the design and implementation of such a tagger.

Once produced, these Higgs bosons predominantly decay into $W^{\pm}Z$ and $W^{\pm}W^{\pm}$ final states, which, through their fully leptonic decay modes, provide clean and experimentally accessible signatures. This makes them highly suitable targets for collider searches, offering opportunities to probe the extended Higgs sector predicted by the GM model.

The analysis reported in this thesis uses the full Run 2 dataset collected by the ATLAS experiment, corresponding to an integrated luminosity of 140 fb^{-1} [19, 20], to search for $H_5^{\pm}$ and $H_5^{\pm\pm}$ production in the VBF topology. The data were collected in proton-proton collisions at a center-of-mass energy of $\sqrt{s} = 13$ TeV. Model-independent upper limits at 95% Confidence Level (CL) are set on the production cross-section times branching fraction for $H_5^{\pm} \to W^{\pm}Z$ and $H_5^{\pm\pm} \to W^{\pm}W^{\pm}$. These results are further interpreted within the framework of the GM model, placing constraints on the parameter $\sin\theta_H$ as a function of the Higgs quintuplet mass m_{H_5}.

The structure of this thesis is organized as follows. Section 2 introduces the GM model in detail, providing the theoretical framework for the analysis. Section 3 offers a brief overview of the ATLAS detector, emphasizing the key components relevant to this study. Section 4 defines the criteria for selecting physics objects—including electrons, muons, jets, and missing transverse momentum ($E_{\mathrm{T}}^{\mathrm{miss}}$)—in both data and Monte Carlo (MC) events. Section 5 describes the data and MC samples used in both parts of the analysis. Section 6 focuses on the development and calibration of quark/gluon jet taggers, which are motivated by the importance of distinguishing quark and gluon jets in VBF processes. Section 7 presents the combination of charged Higgs boson searches within the GM framework. Finally, Section 8 summarizes the findings and concludes the thesis.

Chapter 2

The Standard Model and Beyond

Particle physics aims to understand the basic components of our universe and their interactions. Currently, four fundamental forces are recognized: electromagnetic, strong, weak, and gravitational. Decades of research have led to the development of the Standard Model (SM), which effectively describes interactions among all known elementary particles, except gravity.

This chapter provides a brief introduction to the SM in Section 2.1, covering its theoretical foundations, significant achievements, and inherent limitations. The overview presented here establishes context and motivation for the analyses conducted in this thesis.

2.1 The Standard Model

The SM is a theoretical framework that describes the properties and interactions of elementary particles. It encompasses three of the four fundamental forces: electromagnetic, strong, and weak interactions, while gravity is excluded. Although various theories, such as string theory, aim to incorporate quantum gravity, gravitational interactions are negligible compared to the other three forces at the energy scales relevant to high-energy physics experiments discussed in this thesis. Therefore, gravity is not discussed further.

The SM is based on quantum gauge field theory with internal local symmetries described by the group $SU(3)_C \times SU(2)_L \times U(1)_Y$. All elementary particles within the SM are shown in Figure 2.1. Each particle corresponds to a quantum field, and particles are interpreted as excitations of these fields. Based on their spin, particles are classified into two categories:

fermions and bosons.

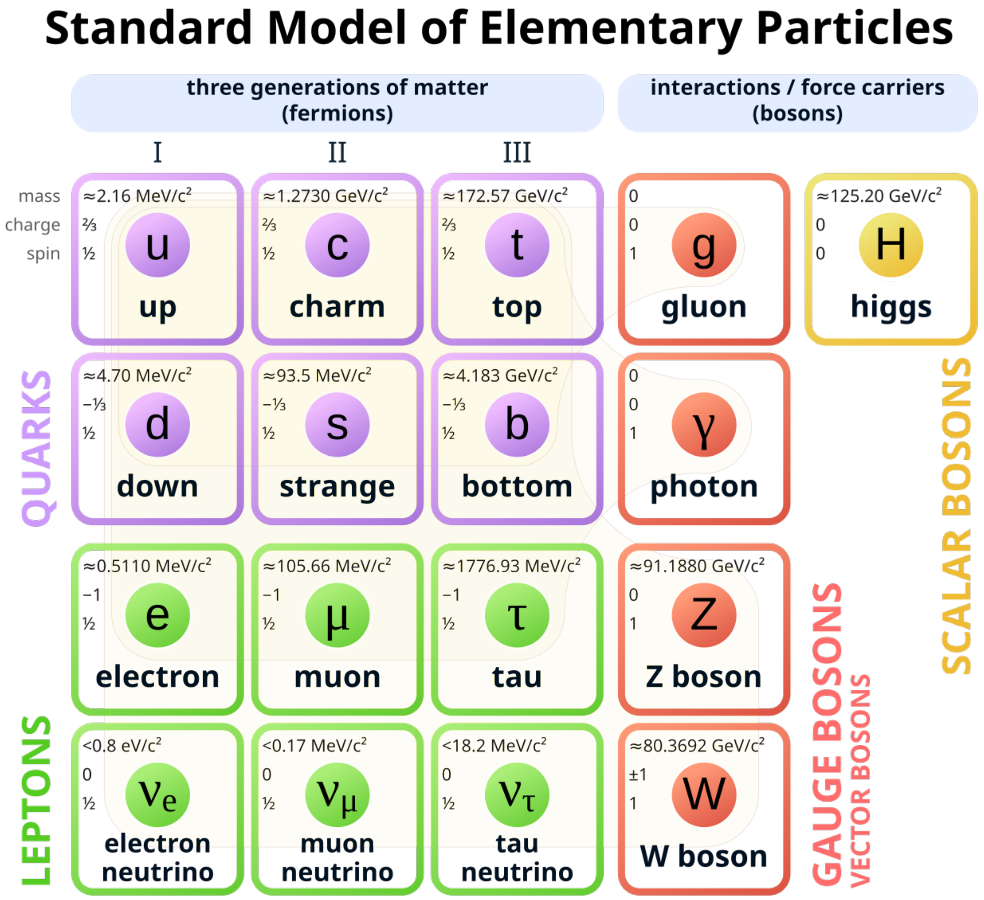

Figure 2.1: Elementary particles of the SM [21].

Fermions possess half-integer spin and constitute matter. They are divided into two groups: leptons and quarks. Both groups follow Fermi-Dirac statistics and are arranged into three generations. Each lepton generation includes a charged lepton and its corresponding neutrino. Neutrinos are electrically neutral and do not experience electromagnetic interactions. Quarks have fractional electric charges and carry color charges.

Bosons, characterized by integer spin, follow Bose-Einstein statistics. Within the SM, bosons include the force carriers and the Higgs boson. The gluon mediates the strong interaction and carries color charge. The photon mediates electromagnetic interactions between charged particles. The W and Z bosons mediate weak interactions. The Higgs boson, discovered in 2012, provides mass to elementary particles, including the W and Z bosons, through the Higgs mechanism.

The complete SM Lagrangian is composed of four terms:

$$\mathcal{L}_{\text{SM}} = \mathcal{L}_{\text{Strong}} + \mathcal{L}_{\text{EW}} + \mathcal{L}_{\text{Higgs}} + \mathcal{L}_{\text{Yukawa}}, \tag{2.1}$$

where the first term describes the strong interaction, the second term represents electroweak interactions, the third term includes kinetic and potential terms for the Higgs field, and the fourth term covers Yukawa interactions between fermions and the Higgs field. Each term's role is discussed briefly in the following sections.

2.1.1 Quantum Chromodynamics

Quantum Chromodynamics (QCD) is the theory describing the strong force. It is a non-Abelian gauge theory based on the symmetry group $SU(3)_C$. The QCD Lagrangian, $\mathcal{L}_{\text{Strong}}$, is expressed as:

$$\mathcal{L}_{\text{Strong}} = -\frac{1}{4} F^a_{\mu\nu} F^{\mu\nu}_a + \sum_f \bar{f}(i\not{D} - m_f)f, \tag{2.2}$$

where f denotes the Dirac spinor of the quark field for each quark flavor, and $F^a_{\mu\nu}$ is the gluon field strength tensor, defined as:

$$F^a_{\mu\nu} = \partial_\mu A^a_\nu - \partial_\nu A^a_\mu - g_s f^{abc} A^b_\mu A^c_\nu, \tag{2.3}$$

Here, A^a_μ are the gluon field components, $A_\mu = A^a_\mu t^a$ with $a = 1, \ldots, 8$, and f^{abc} are the structure constants for $SU(3)_C$. The term $\not{D} \equiv \gamma^\mu D_\mu$ represents the covariant derivative, defined by:

$$D_\mu = \partial_\mu - i g_s A_\mu, \tag{2.4}$$

where g_s is the QCD coupling constant, and t^a are the generators of $SU(3)_C$ in the fundamental representation.

QCD explains how quarks and gluons interact, which is crucial for understanding the physics in hadron colliders. A key feature of QCD is asymptotic freedom. Unlike other coupling constants, the strong coupling g_s becomes weaker at very high energies or short distances, allowing perturbation theory calculations. At lower energies, the coupling grows stronger, which explains why quarks are never observed as free particles in nature.

The energy dependence of the strong coupling constant α_s is governed by the renormalization group equation. At one-loop level, its running is given by [22]:

$$\alpha_s(|q^2|) = \frac{\alpha_s(\mu^2)}{1 + \frac{\alpha_s(\mu^2)}{12\pi}(11n - 2f)\ln(|q^2|/\mu^2)} \quad (|q^2| \gg \mu^2) \tag{2.5}$$

where μ is the renormalization scale, n is the number of colors in QCD (typically $n = 3$), and f represents the number of active quark flavors. This equation encapsulates the logarithmic running of the strong coupling constant, illustrating the asymptotic freedom of QCD.

At lower energies, where α_s becomes large, perturbation theory is no longer valid, and quarks and gluons are confined into hadrons through a process known as hadronization. Event generators such as Pythia model hadronization using phenomenological approaches. The most widely used scheme is the Lund string model[23], which describes the color field between quarks and antiquarks as a string-like flux tube. As the system evolves, the string stretches and eventually fragments, producing a cascade of hadrons. This model successfully explains many features of hadronic final states observed in collider experiments.

2.1.2 Quarks and Gluons: Properties and Differences

Quarks and gluons are the fundamental degrees of freedom in QCD, each with distinct properties arising from their roles in the SU$(3)_C$ gauge symmetry. Quarks are spin-$\frac{1}{2}$ fermions that carry color charge, flavor, and electric charge, while gluons are spin-1 bosons that mediate the strong interaction and carry only color charge. The self-interaction of gluons, a result of the non-Abelian nature of SU$(3)_C$, gives rise to unique phenomena such as confinement and asymptotic freedom.

A key theoretical distinction between quarks and gluons is their representation in the SU$(3)_C$ group. Quarks belong to the fundamental representation, while gluons belong to the adjoint representation. The strength of these interactions is quantified by the Casimir operator, defined as:

$$C_R\,\mathbb{I}_{\dim(R)\times\dim(R)} = \sum_{a=1}^{8} t^a\,t^a \tag{2.6}$$

where t^a $(a = 1, \ldots, 8)$ are the generators of the SU$(3)_C$ group.

For quarks in the fundamental representation, the Casimir value is:

$$C_F = \frac{N_c^2 - 1}{2\,N_c}, \tag{2.7}$$

where $N_c = 3$ is the number of colors in QCD. Substituting $N_c = 3$, we obtain:

$$C_F = \frac{4}{3}. \tag{2.8}$$

For gluons in the adjoint representation, the Casimir value is:

$$C_A = N_c, \tag{2.9}$$

which gives

$$C_A = 3. \tag{2.10}$$

The ratio of the Casimir values, often called the Casimir ratio, is:

$$\frac{C_A}{C_F} = \frac{3}{\frac{4}{3}} = \frac{9}{4}. \tag{2.11}$$

This larger color factor for gluons reflects their stronger effective self-interaction. When color factors enter branching probabilities and splitting functions, a higher Casimir value increases the probability of gluon radiation, leading to broader jets and higher particle multiplicities in gluon-initiated jets compared to quark-initiated jets.

The differences in Casimir values are not only theoretical distinctions but also have practical implications in QCD phenomena and high-energy collisions. These properties form part of the theoretical foundation for quark/gluon jet calibration techniques, as discussed in Section 6.

2.1.3 Electroweak Theory

The electroweak theory within the SM unifies electromagnetic and weak interactions using the gauge symmetry group $SU(2)_L \times U(1)_Y$. The electroweak Lagrangian is given by:

$$\begin{aligned}\mathcal{L}_{\text{EW}} &= \bar{Q}_i i\not{D} Q_i + \bar{L}_i i\not{D} L_i + \bar{e}_{R,i} i\not{D} e_{R,i} + \bar{\nu}_{R,i} i\not{D} \nu_{R,i} \\ &+ \bar{u}_{R,i} i\not{D} u_{R,i} + \bar{d}_{R,i} i\not{D} d_{R,i} - \frac{1}{4} W^a_{\mu\nu} W^{\mu\nu}_a - \frac{1}{4} B_{\mu\nu} B^{\mu\nu},\end{aligned} \tag{2.12}$$

where $Q_i = (u_L, d_L)^T$ and $L_i = (\nu_L, e_L)^T$ represent left-handed doublets of quarks and leptons for each generation, respectively. The fields u_R and d_R denote right-handed singlet up and down quarks, while e_R and ν_R indicate right-handed singlet leptons. The covariant derivative D_μ is defined as:

$$D_\mu = \partial_\mu + i\frac{g}{2}\tau^a W^a_\mu + i\frac{g'}{2} Y B_\mu, \tag{2.13}$$

where g and g' are the gauge couplings of $SU(2)_L$ and $U(1)_Y$, respectively. Here, W^a_μ represents the gauge fields of $SU(2)_L$, indexed by $a = 1, 2, 3$ in the weak isospin space, while B_μ is the gauge field of $U(1)_Y$. The weak hypercharge Y is assigned to each particle such that:

$$Q = T_3 + \frac{Y}{2}, \tag{2.14}$$

where Q denotes the electric charge, and T_3 is the third component of weak isospin.

The gauge field strength tensors describe the dynamics of the gauge bosons and are given by:

$$W^a_{\mu\nu} = \partial_\mu W^a_\nu - \partial_\nu W^a_\mu + g\epsilon^{abc} W^b_\mu W^c_\nu, \tag{2.15}$$

and

$$B_{\mu\nu} = \partial_\mu B_\nu - \partial_\nu B_\mu, \tag{2.16}$$

where ϵ^{abc} are the structure constants of $SU(2)_L$.

The Lagrangian $\mathcal{L}_{\text{EW}}$ describes the interactions between fermions and gauge bosons as well as the self-interactions of the gauge bosons. The first six terms represent the kinetic and interaction terms for the fermions, while the last two terms account for the gauge boson kinetic terms and self-interactions. These interactions govern a wide range of physical processes, such as beta decay and neutrino scattering, which are mediated by the $W^\pm$ and

Z bosons.

However, a key feature of this Lagrangian is the absence of mass terms for the gauge bosons. Explicit mass terms like $m^2 W_\mu^a W^{\mu a}$ or $m^2 B_\mu B^\mu$ would violate gauge invariance, as they are not invariant under local $SU(2)_L \times U(1)_Y$ transformations. This apparent shortcoming becomes evident in the experimental observation of massive $W^\pm$ and Z bosons. Additionally, the neutrinos described in the SM are initially massless in $\mathcal{L}_{\text{EW}}$, which contradicts experimental evidence for neutrino oscillations, suggesting a need for beyond-Standard-Model physics.

To address the gauge boson mass problem, the SM introduces a complex scalar field, the Higgs field Φ, which triggers spontaneous symmetry breaking via the Higgs mechanism [24]. The Higgs mechanism not only explains the masses of the $W^\pm$ and Z bosons but also provides a framework for fermion mass generation through Yukawa couplings. These concepts are discussed in detail in the next section on electroweak symmetry breaking.

2.1.4 Electroweak Symmetry Breaking and the Higgs Mechanism

While the electroweak theory provides a unified framework for describing electromagnetic and weak interactions, it inherently lacks mass terms for the gauge bosons. Explicit mass terms would violate gauge invariance, rendering the theory inconsistent with experimental observations of massive $W^\pm$ and Z bosons. Similarly, fermions and neutrinos would remain massless without additional mechanisms, contradicting the experimentally observed fermion masses and neutrino oscillations.

To address these issues, the Higgs mechanism was proposed in 1964 by Brout, Englert, and Higgs. It introduces a complex scalar field Φ, which triggers spontaneous symmetry breaking of the $SU(2)_L \times U(1)_Y$ gauge symmetry down to the electromagnetic subgroup $U(1)_{\text{EM}}$. This process gives rise to massive gauge bosons while preserving gauge invariance, and provides a framework for fermions to acquire mass through Yukawa couplings.

The Higgs field is represented as a complex doublet:

$$\Phi = \begin{pmatrix} \phi^+ \\ \phi^0 \end{pmatrix}, \tag{2.17}$$

where ϕ^+ and ϕ^0 are the charged and neutral components of the Higgs field.

The Lagrangian for the Higgs field consists of two main contributions:

$$\mathcal{L}_{\text{Higgs}} = \mathcal{L}_{\text{kinetic}} + \mathcal{L}_{\text{potential}}, \tag{2.18}$$

where the kinetic term is

$$\mathcal{L}_{\text{kinetic}} = (D_\mu \Phi)^\dagger (D_\mu \Phi), \tag{2.19}$$

and the potential energy term is

$$\mathcal{L}_{\text{potential}} = -\mu^2 \Phi^\dagger \Phi + \lambda (\Phi^\dagger \Phi)^2. \tag{2.20}$$

Here, μ^2 and λ are parameters of the potential, with $\mu^2 > 0$ ensuring the potential has a minimum at a non-zero value of Φ, while $\lambda > 0$ ensuring the stability of the potential at large field values. The covariant derivative in the kinetic term ensures gauge invariance and is defined as:

$$D_\mu \Phi = \left(\partial_\mu + ig W_\mu^a \frac{\tau^a}{2} + i \frac{g'}{2} B_\mu \right) \Phi, \tag{2.21}$$

where g and g' are the gauge couplings of the $SU(2)_L$ and $U(1)_Y$ gauge groups, respectively. The fields W_μ^a ($a = 1, 2, 3$) are the gauge bosons of $SU(2)_L$, B_μ is the gauge boson of $U(1)_Y$, and τ^a are the Pauli matrices.

When $\mu^2 > 0$, the Higgs potential develops a nonzero vacuum expectation value (VEV), breaking the $SU(2)_L \times U(1)_Y$ gauge symmetry down to the electromagnetic subgroup $U(1)_{\text{EM}}$. The VEV of the Higgs field is:

$$\langle \Phi \rangle = \frac{1}{\sqrt{2}} \begin{pmatrix} 0 \\ v \end{pmatrix}, \tag{2.22}$$

where $v \approx 246\,\text{GeV}$ is determined experimentally. To analyze the particle spectrum after symmetry breaking, one can choose the unitary gauge, in which the Higgs field is parametrized as:

$$\Phi(x) = \frac{1}{\sqrt{2}} \begin{pmatrix} 0 \\ v + H(x) \end{pmatrix}, \tag{2.23}$$

where $H(x)$ represents the physical Higgs boson, corresponding to quantum fluctuations around the VEV.

Through this process, three of the four degrees of freedom in $\Phi(x)$ are reinterpreted as the longitudinal components of the massive gauge bosons $W^\pm$ and Z, while the remaining degree of freedom corresponds to the physical Higgs boson. Specifically:

- The charged Goldstone bosons ($\phi^\pm$) are absorbed by W^+ and W^-, each gaining one longitudinal degree of freedom.
- The neutral Goldstone boson (ϕ^0) is absorbed by the Z boson, giving it its longitudinal component.
- The photon (γ) remains massless due to the unbroken $U(1)_{\text{EM}}$ symmetry.

The gauge bosons W^a_μ and B_μ mix to produce the physical states:

$$W^\pm = \frac{1}{\sqrt{2}}(W^1 \mp iW^2), \tag{2.24}$$

$$Z = \cos\theta_W W^3 - \sin\theta_W B, \tag{2.25}$$

$$\gamma = \sin\theta_W W^3 + \cos\theta_W B, \tag{2.26}$$

where θ_W is the weak mixing angle (Weinberg angle), defined as:

$$\tan\theta_W = \frac{g'}{g}. \tag{2.27}$$

Experimentally, $\sin^2\theta_W \approx 0.231$.

The masses of the $W^\pm$ and Z bosons are generated as:

$$m_{W^\pm} = \frac{gv}{2}, \tag{2.28}$$

$$m_Z = \frac{\sqrt{g^2 + g'^2}\, v}{2}, \tag{2.29}$$

with experimentally measured values $m_{W^\pm} \approx 80.385\,\text{GeV}$ and $m_Z \approx 91.1876\,\text{GeV}$. The photon remains massless due to the unbroken $U(1)_{\text{EM}}$ gauge symmetry.

In addition to generating gauge boson masses, the Higgs mechanism provides a way for fermions to acquire mass through Yukawa interactions. The Yukawa coupling term in the Lagrangian is written as:

$$\mathcal{L}_{\text{Yukawa}} = -\sum_f y_f\, \bar{f}_L \Phi f_R + \text{h.c.}, \tag{2.30}$$

where f_L and f_R are the left-handed and right-handed components of the fermion field f, y_f is the Yukawa coupling constant, and "h.c." denotes the Hermitian conjugate. Substituting the Higgs field from Equation 2.23 into this term leads to fermion masses:

$$m_f = \frac{y_f v}{\sqrt{2}}. \tag{2.31}$$

Thus, the mass of each fermion is directly proportional to its Yukawa coupling y_f. For example, the top quark, with $m_t \approx 173\,\text{GeV}$, has the largest Yukawa coupling, $y_t \approx 1$, indicating a strong interaction with the Higgs field, while lighter fermions like the electron ($m_e \approx 0.511\,\text{MeV}$) have much smaller Yukawa couplings ($y_e \approx 2.9 \times 10^{-6}$).

The remaining term $H(x)$ in Equation 2.23 corresponds to the Higgs boson, with its mass determined by the self-coupling λ:

$$m_H = \sqrt{2\lambda}\, v. \tag{2.32}$$

The experimentally measured Higgs boson mass is $m_H \approx 125.09\,\text{GeV}$, allowing us to infer $\lambda \approx 0.13$.

The form of $\mathcal{L}_{\text{potential}}$ given above is the simplest form, but it can be extended in various Higgs extensions, such as multi-Higgs doublet models or composite Higgs models, to explore new physics beyond the SM.

2.2 The Georgi-Machacek Model

Given the current uncertainties in Higgs boson coupling measurements, electroweak symmetry breaking mechanisms with extended Higgs sectors remain a compelling area of research. While the SM Higgs mechanism successfully generates the masses of gauge bosons and fermions, it is restricted to the simplest scalar sector and leaves open the possibility of exploring richer scalar structures. Extended Higgs models, such as the Georgi-Machacek (GM) model [25, 26], offers a framework for investigating the phenomenology of larger Higgs representations and custodial symmetry, while maintaining consistency with precision electroweak measurements. The following chapter draws heavily on the theory papers and Theoretical Advanced Study Institute (TASI) lectures [27, 28, 29]. This chapter begins by explaining how custodial symmetry is preserved through the introduction of two additional scalar triplets in Section 2.2.1. It then explores the phenomenological implications of the model in

Section 2.2.2, concluding with its application in collider physics searches in Section 2.2.3.

2.2.1 The ρ Parameter and Custodial Symmetry

The ρ parameter was introduced to describe the relative strength of neutral-current and charged-current weak interaction processes at low momentum transfers [29]. Defined as the ratio of neutral to charged current strengths, it is expressed as:

$$\rho = \left(\frac{g^2}{c_W^2 M_Z^2}\right) \times \left(\frac{g^2}{M_W^2}\right)^{-1} = \frac{M_W^2}{c_W^2 M_Z^2}. \tag{2.33}$$

In the SM, substituting the expressions for M_W and M_Z gives:

$$M_W^2 = \frac{g^2 v^2}{4}, \qquad M_Z^2 = \frac{(g^2 + g'^2)v^2}{4} = \frac{g^2 v^2}{4 c_W^2}, \tag{2.34}$$

leading to $\rho = 1$ automatically. This unity value of ρ arises from an approximate global symmetry of the SM called *custodial SU(2) symmetry*, which is a remnant global SU(2) symmetry that prevents radiative corrections driving the SM ρ away from 1 after spontaneous symmetry breaking. Experimental measurement reports $\rho = 1.00039 \pm 0.00019$ from Partile Data Group [30].

When extending the SM, the electroweak ρ parameter must remain close to unity to satisfy experimental constraints. A single triplet extension cannot achieve this condition; therefore, the GM model introduces **two** scalar triplets:

- A complex triplet $\chi = (\chi^{++}, \chi^{+}, \chi^{0})^T$ with hypercharge $Y = 2$,
- A real triplet $\xi = (\xi^{+}, \xi^{0}, \xi^{-})^T$ with hypercharge $Y = 0$.

These triplets, together with the SM Higgs doublet $\Phi = (\phi^{+}, \phi^{0})^T$ reinterpreted as a bi-doublet, form a custodially symmetric structure:

$$\Phi = \begin{pmatrix} \phi^{0*} & \phi^{+} \\ -\phi^{+*} & \phi^{0} \end{pmatrix}, \quad X = \begin{pmatrix} \chi^{0*} & \xi^{+} & \chi^{++} \\ -\chi^{+*} & \xi^{0} & \chi^{+} \\ \chi^{++*} & -\xi^{+*} & \chi^{0} \end{pmatrix}.$$

Different from the SM, the gauge boson masses need to take into account the additional triplet contributions, writing out the kinetic Lagrangian in the GM model,

$$\mathcal{L}_{\text{kin}} \supset (\mathcal{D}_\mu \Phi)^\dagger (\mathcal{D}^\mu \Phi) + \frac{1}{2}(\mathcal{D}_\mu \xi)^\dagger (\mathcal{D}^\mu \xi) + (\mathcal{D}_\mu \chi)^\dagger (\mathcal{D}^\mu \chi), \tag{2.35}$$

where $\mathcal{D}_\mu$ is the covariant derivative. The mass of W and Z boson, in this context, are expressed by

$$M_W^2 = \frac{g^2}{4}(v_\phi^2 + 4v_\xi^2 + 4v_\chi^2), \qquad M_Z^2 = \frac{g^2 + g'^2}{4}(v_\phi^2 + 8v_\chi^2) = \frac{g^2}{4c_W^2}(v_\phi^2 + 8v_\chi^2), \tag{2.36}$$

To impose the custodial symmetry at the tree level in the presence of the $Y = 0$ and $Y = 1$ triplets, we have

$$\rho \equiv \frac{M_W^2}{c_W^2 M_Z^2} = \frac{v_\phi^2 + 4v_\xi^2 + 4v_\chi^2}{v_\phi^2 + 8v_\chi^2} \tag{2.37}$$

To ensure $\rho = 1$ at tree level, custodial symmetry imposes the condition:

$$v_\xi = v_\chi. \tag{2.38}$$

Now the total electroweak VEV is constrained by:

$$v^2 = v_\phi^2 + 8v_\chi^2 \approx (246\,\text{GeV})^2. \tag{2.39}$$

A useful parameter is the mixing angle θ_H, indicating the contributions of v_ϕ and v_χ to the mass of gague bosons, defined as:

$$\cos\theta_H = \frac{v_\phi}{v}, \quad \sin\theta_H = \frac{2\sqrt{2}v_\chi}{v}. \tag{2.40}$$

Similar to the SM Higgs, some constrains can be obtained by minimizing the potential:

$$V(v_\phi, v_\chi) = \frac{\mu_2^2}{2}v_\phi^2 + 3\frac{\mu_3^2}{2}v_\chi^2 + \lambda_1 v_\phi^4 + \frac{3}{2}(2\lambda_2 - \lambda_5)\, v_\phi^2 v_\chi^2 + 3(\lambda_3 + 3\lambda_4)\, v_\chi^4 - \frac{3}{4}M_1 v_\phi^2 v_\chi - 6M_2 v_\chi^3. \tag{2.41}$$

Here, μ_2^2 and μ_3^2 are mass parameters, λ_1 to λ_5 are dimensionless quartic couplings that control the strength of interactions between the scalar fields, and M_1, M_2 are mixing parameters. Together, these parameters define the vacuum structure and scalar mass spectrum of the model.

2.2.2 Phenomenological Implications

The scalar states in the GM model can be categorized based on their transformation properties under the custodial symmetry group $SU(2)_C$. The SM Higgs doublet and the introduced triplets transform as follows:

- **Bi-doublet**: Φ transforms as a $2 \otimes 2$ representation under $SU(2)_L \times SU(2)_R$, which decomposes into $3 \oplus 1$ under the custodial $SU(2)_C$.
- **Bi-triplet**: X transforms as a $3 \otimes 3$ representation under $SU(2)_L \times SU(2)_R$, breaking down into $5 \oplus 3 \oplus 1$ under $SU(2)_C$.

From these transformations, the physical scalar states are organized into custodial multiplets:

- **Singlets**: Two custodial singlets (transforming as 1 under $SU(2)_C$) mix to form the states h^0 (the SM-like Higgs) and H^0.
- **Triplet**: The custodial triplet (transforming as 3 under $SU(2)_C$) contains the Goldstone bosons (G^+, G^0, G^-), along with a custodial triplet of physical states (H_3^+, H_3^0, H_3^-).
- **Quintuplet**: The custodial quintuplet (transforming as 5 under $SU(2)_C$) consists of the physical states $(H_5^{++}, H_5^+, H_5^0, H_5^-, H_5^{--})$.

The physical states can be expressed as linear combinations of the scalar fields in the bi-doublet and bi-triplet:

$$
\begin{aligned}
H_5^{\pm\pm} &= \chi^{\pm\pm}, \\
H_5^{\pm} &= \frac{\chi^{\pm} - \xi^{\pm}}{\sqrt{2}}, \\
H_5^{0} &= \frac{\sqrt{2}\xi^{0,r} - \chi^{0,r}}{\sqrt{3}}, \\
H_3^{\pm} &= -\sin\theta_H \phi^{\pm} + \cos\theta_H \frac{\chi^{\pm} + \xi^{\pm}}{\sqrt{2}}, \\
H_3^{0} &= -\sin\theta_H \phi^{0} + \cos\theta_H \chi^{0,i}.
\end{aligned}
\tag{2.42}
$$

The custodial quintuplet H_5 is custodially symmetric and fermiophobic, coupling exclusively to vector bosons. This fermiophobic nature arises because H_5 is composed entirely of components from the scalar triplets, and the scalar doublet, which enables Yukawa couplings to fermions, does not contribute to the quintuplet. This makes H_5 particularly promising for studies involving vector boson fusion (VBF) processes. In contrast, the custodial triplet H_3 mixes with the SM Higgs doublet and has non-zero couplings to fermions. These unique features give rise to rich phenomenological opportunities for probing the extended scalar sector in collider experiments.

2.2.3 `H5plane` as a Benchmark

To explore the experimental implications of the GM model, the `H5plane` benchmark is often adopted [31]. This framework assumes that the triplet states H_3 and H are significantly heavier than the quintuplet H_5, resulting in the exclusive decay of H_5 bosons into vector boson pairs. In this scenario:

- The singly charged $H_5^{\pm}$ and doubly charged $H_5^{\pm\pm}$ bosons are degenerate in mass (M_{H_5}).
- The decay widths of H_5 into WW, WZ, and ZZ are proportional to $\sin^2\theta_H$, representing the contribution of the triplet VEV to the gauge boson masses.
- The production of H_5 states is dominated by VBF processes due to their enhanced couplings to vector bosons.

Under the `H5plane` benchmark, the branching ratios of H_5 bosons to vector boson pairs are assumed to be 100%. This makes H_5 states ideal candidates for searches in VBF channels. Representative Feynman diagrams for the production and decay of $H_5^{\pm}$ and $H_5^{\pm\pm}$ bosons are shown in Figure 2.2.

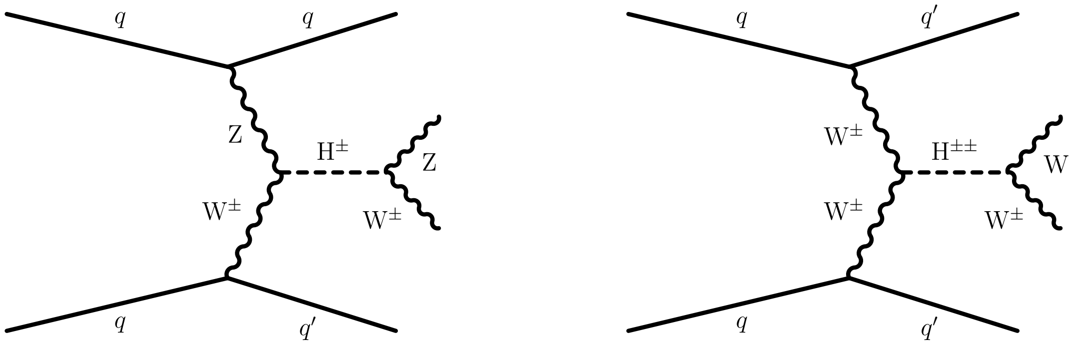

Figure 2.2: Representative Feynman diagrams showing the production of $H_5^{\pm}$ and $H_5^{\pm\pm}$ charged Higgs bosons via VBF.

Chapter 3

The LHC and the ATLAS Experiment

This chapter delineates the experimental infrastructure, establishing the technical foundation for analyses presented in subsequent chapters. Section 3.1 characterizes the Large Hadron Collider (LHC) accelerator complex with essential terminology. Collision data acquisition systems are addressed through the ATLAS detector architecture detailed in Section 3.2. Furthermore, Section 3.3 outlines strategic computing upgrades designed to enhance the detector's physics reach during future operational phases for HL-LHC.

3.1 The Large Hadron Collider

The LHC, located at Conseil Européen pour la Recherche Nucléaire (CERN) near Geneva, Switzerland, is the world's most energetic particle accelerator. Designed to achieve a center-of-mass energy of $\sqrt{s} = 14$ TeV, the LHC consists of a 26.7-km circular tunnel buried 50–175 m underground, straddling the Franco-Swiss border. Within this ring, counter-rotating hadron beams are accelerated to relativistic speeds ($\beta \approx 1$) before being brought into collision at four primary interaction points (IPs), each equipped with a major detector: ATLAS and CMS (general-purpose experiments), LHCb (dedicated to flavor physics), and ALICE (focused on heavy-ion collisions). This study considers only pp collision data and does not include heavy-ion results.

One of the primary objectives of the LHC in its early operational phase (2010–2012) was the search for the Higgs boson, the final missing component of the SM. The Higgs boson is crucial for explaining the mechanism by which elementary particles acquire mass.

In 2012, both the ATLAS and CMS collaborations reported the discovery of a new particle consistent with the Higgs boson, with a measured mass of approximately 125 GeV. This discovery, announced on July 4, 2012, was based on data from Run 1 and achieved a statistical significance of 5σ, satisfying the threshold for a discovery in particle physics. This milestone confirmed a key prediction of the SM and represented a major success of the LHC program.

The operational history of the LHC is divided into distinct phases: Run 1, Run 2, Run 3 (currently), and the upcoming HL-LHC era.

- **Run 1 (2009–2013)**: The initial phase of the LHC operated with a nominal collision energy of 7 TeV, corresponding to 3.5 TeV per beam. In 2012, the beam energy was increased to 4 TeV, yielding a center-of-mass energy of 8 TeV. Run 1 concluded in 2013 with the start of Long Shutdown 1 (LS1), during which extensive maintenance and upgrades were conducted on both the accelerator and the detectors.

- **Run 2 (2015–2018)**: Following LS1, the LHC resumed operations in 2015 with an increased beam energy of 6.5 TeV, resulting in a center-of-mass energy of 13 TeV. This period also saw significant improvements in luminosity, with data collection surpassing the total of Run 1 by 2016. Run 2 concluded at the end of 2018, initiating Long Shutdown 2 (LS2) for further upgrades.

- **Run 3 (2022–2026)**: Run 3 commenced after LS2, with operations projected to accumulate an integrated luminosity exceeding that of Runs 1 and 2 combined. This phase, ongoing at the time of writing, aims to explore higher precision measurements and new physics searches.

- **High-Luminosity LHC (HL-LHC, 2029–2038)**: Following Long Shutdown 3 (LS3) starting in 2026, the LHC will transition into the HL-LHC era, targeting a luminosity increase by a factor of ten compared to the original design. Some preparatory modifications for HL-LHC were already implemented during LS2.

These successive upgrades enable the LHC to probe increasingly rare processes, enhance precision in SM measurements, and extend searches for new physics beyond the SM.

3.1.1 The Accelerator Complex

Protons destined for collisions in ATLAS or other LHC detectors originate from hydrogen atoms. These atoms undergo ionization in an electric field, stripping them of their electrons to yield free protons. The acceleration process begins in Linac 2, where the protons are accelerated to 50 MeV. Subsequently, they are sequentially injected into a series of accelerators: the Proton Synchrotron Booster, the Proton Synchrotron, and the Super Proton Synchrotron, reaching energies of 1.4 GeV, 25 GeV, and 450 GeV, respectively. Finally, the protons enter the LHC through two separate beam pipes, where they are further accelerated to their final energy of 6.5 TeV. One proton beam circulates clockwise while the other moves counterclockwise, resulting in head-on collisions at designated interaction points with a total center-of-mass energy equal to the sum of the two beam energies. This acceleration chain is illustrated in fig. 3.1.

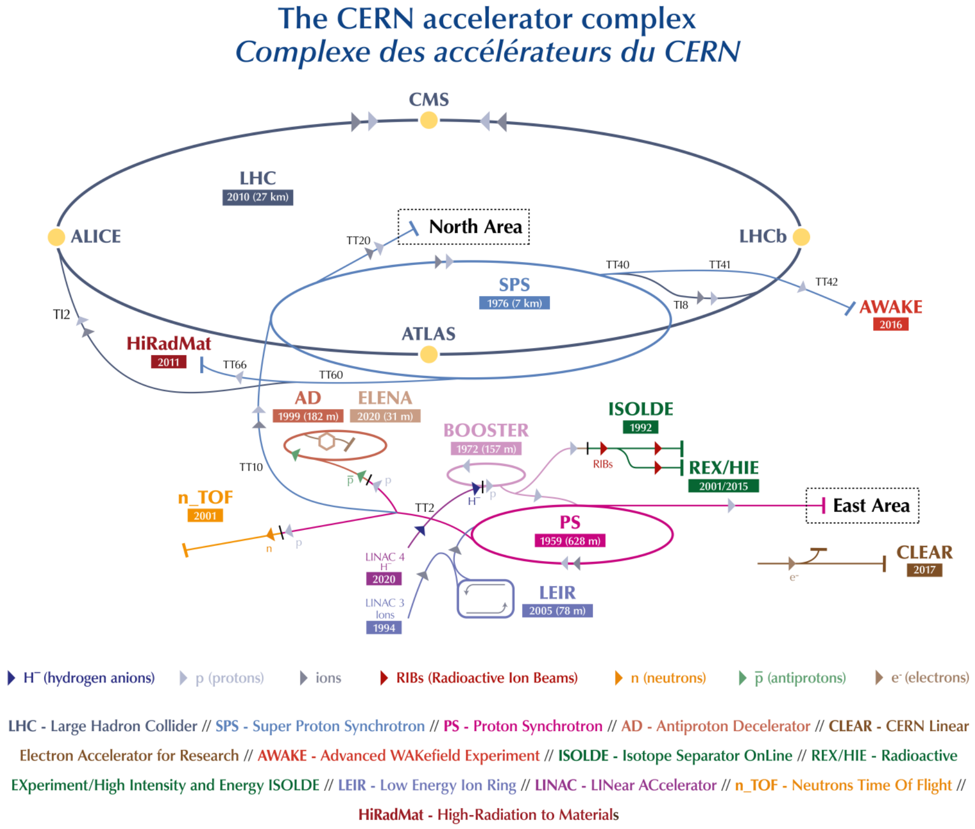

Figure 3.1: Schematic representation of the LHC accelerator complex, showing the sequential acceleration stages from Linac 2 to the LHC [32].

As the proton beam traverses each accelerator ring, it interacts with radiofrequency (RF) cavities that generate a longitudinally oscillating voltage. This interaction causes the protons to cluster into discrete *bunches*, which are confined within RF potential wells known as *buckets*. The arrangement of filled and empty buckets follows a specific *filling scheme*, which dictates the beam structure.

For *pp* collisions, the nominal filling scheme employs a 25 ns bunch spacing. Initially, in the Proton Synchrotron, protons are grouped into six bunches, which are subsequently split into 18 bunches within 21 available buckets—leaving three buckets empty. The protons are then accelerated to 25 GeV and undergo further splitting, forming 84 buckets, 72 of which are populated. Prior to LHC injection, the protons are organized into 39 batches, each containing 72 bunches per beam. Within a batch, bunches are spaced by 25 ns, while larger gaps between batches accommodate the powering cycle of the SPS and LHC magnetic elements. This scheme ultimately results in a total of 2808 filled bunches in the LHC.

The bunch structure directly influences the collision pattern observed in the LHC detectors. When bunches from opposing beams overlap at an interaction point, the resulting *bunch crossing* can be classified as *paired*, *unpaired*, or *empty*. A paired bunch crossing occurs when both beams contain filled bunches, allowing for potential collisions. In contrast, an unpaired bunch crossing features only one filled bunch, while an empty bunch crossing involves two unfilled bunches, producing no interactions.

3.1.2 Luminosity

Luminosity quantifies the collision rate of protons in a paired bunch crossing, governed by the accelerator's operational parameters. It is expressed as the number of interactions per unit area per unit time and is defined as the ratio of the inelastic collision rate, R_{inel}, to the inelastic *pp* collision cross-section, σ_{inel}:

$$\mathcal{L} = \frac{R_{\text{inel}}}{\sigma_{\text{inel}}}. \tag{3.1}$$

The rate R_{inel} can be further expressed in terms of accelerator-specific parameters:

$$\mathcal{L} = \frac{\mu n_b f_r}{\sigma_{\text{inel}}}, \tag{3.2}$$

where μ represents the average number of inelastic interactions per bunch crossing, n_b is the number of bunches per beam, and f_r denotes the revolution frequency of the collider. Further decomposition of μ and σ_{inel} leads to an expression incorporating bunch-specific parameters:

$$\mathcal{L} = \frac{n_b f_r n_1 n_2}{2\pi \Sigma_x \Sigma_y} F, \tag{3.3}$$

where n_1 and n_2 are the proton populations in the colliding bunches, while Σ_x and Σ_y represent the horizontal and vertical beam profile widths. The geometric factor F accounts for the crossing angle of the beams. Intuitively, increasing the proton count or focusing the beams to a smaller transverse area enhances the collision probability. The luminosity unit is cm^{-2}s^{-1}, and the total integrated luminosity—representing cumulative delivered luminosity over time—is typically expressed in inverse femtobarns (fb^{-1}), where 1 barn $= 10^{-24}$ cm^2 and 1 fb $= 10^{-15}$ barn. The total integrated luminosity recorded during Run 2 is depicted in fig. 3.2.

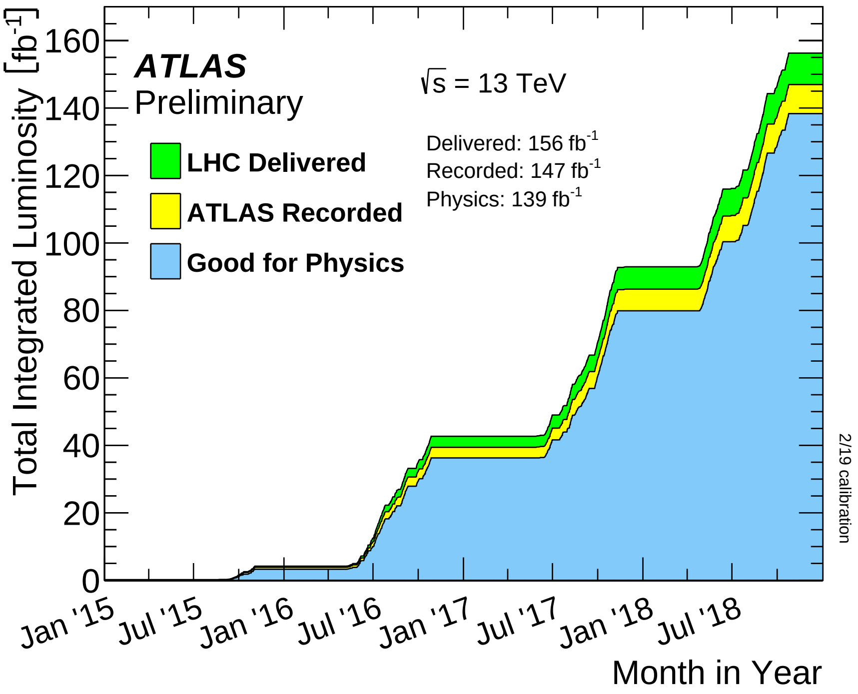

Figure 3.2: Cumulative integrated luminosity recorded by ATLAS during Run 2, showing delivered luminosity over time with data quality criteria applied.

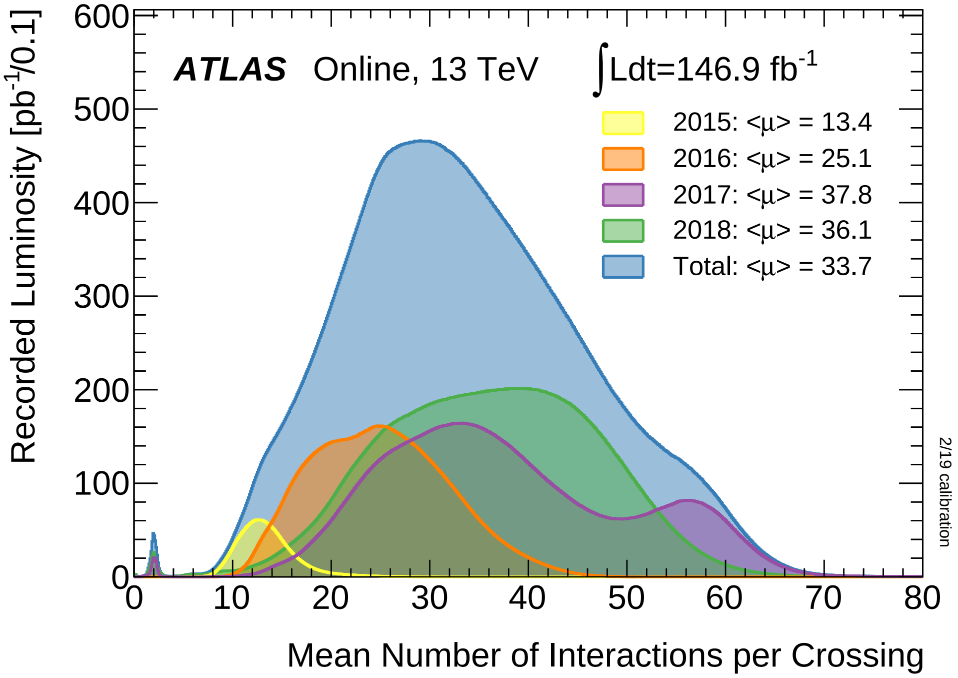

Figure 3.3: Distribution of the average number of interactions per bunch crossing ($< \mu >$) recorded during Run 2, presented separately for each year.

3.1.3 Pileup

Pileup refers to the occurrence of multiple inelastic interactions within a single bunch crossing. It is directly related to the parameter μ in eq. (3.2), which represents the average number of inelastic interactions per bunch crossing. As the luminosity increases, so does the probability of multiple simultaneous interactions. Consequently, pileup levels varied across the different years of Run 2, as illustrated in fig. 3.3. Throughout Run 2, the average pileup value was approximately 33.7 interactions per bunch crossing. Understanding the pileup distribution in data is crucial for accurately simulating Monte Carlo (MC) samples, as events must be reweighted to match the observed distribution.

3.2 The ATLAS Detector

The ATLAS detector, illustrated in fig. 3.4, is a highly sophisticated instrument designed for high-energy physics experiments at LHC. It measures 44 meters in length, 25 meters in diameter, and has a total weight of approximately 7000 tons.

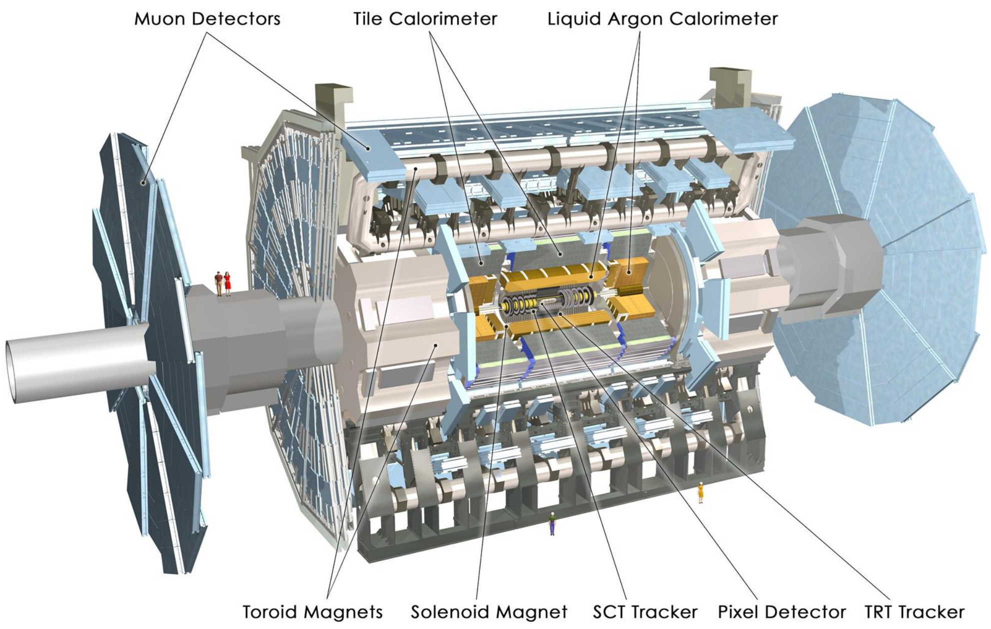

Figure 3.4: The ATLAS detector with labeled subdetectors [33].

The ATLAS detector employs a well-defined coordinate system, as depicted in fig. 3.5. The origin is set at the nominal interaction point of the proton-proton collisions. In the Cartesian coordinate system, the x-axis points from the interaction point towards the center of the LHC ring, parallel to the Earth's surface. The y-axis extends vertically upward, while the z-axis aligns with the beamline, oriented counterclockwise along the LHC ring as viewed from above. In the cylindrical coordinate system, the spatial variables x and y are replaced by the azimuthal angle $\phi \in [-\pi, \pi]$ and the polar angle $\theta \in [0, \pi]$, where $\phi = 0$ aligns with the x-axis and $\theta = 0$ corresponds to the z-axis.

A commonly used alternative to the polar angle θ is the pseudorapidity, defined as $\eta = -\ln \tan(\theta/2)$. This variable is Lorentz-invariant under boosts along the beamline and provides a useful measure of angular displacement. The pseudorapidity takes values from $\eta = 0$ (perpendicular to the beamline) to $\pm\infty$ (parallel to the beamline). The detector is conventionally divided into the *barrel* and the *endcaps*, with the transition typically defined in terms of η. The region with $z > 0$ is referred to as the A-side, while $z < 0$ corresponds to the C-side.

The ATLAS detector consists of three primary subsystems arranged in concentric layers around the beamline: the Inner Detector, the calorimeters, and the Muon Spectrometer. This arrangement is crucial for particle identification and precise energy measurements.

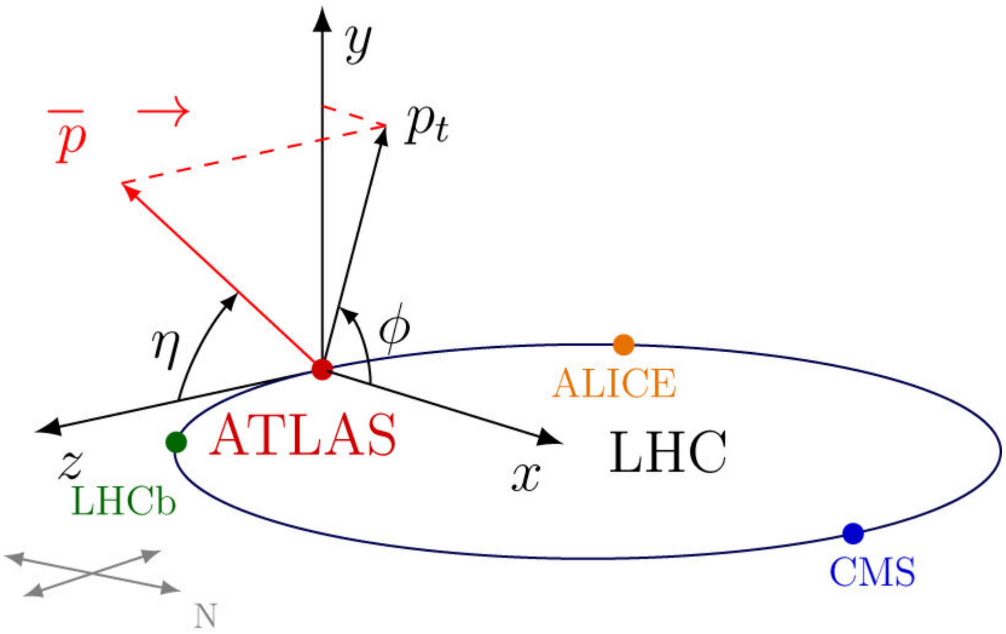

Figure 3.5: The coordinate system of the ATLAS detector [34].

3.2.1 Inner Detector

The ID records the trajectories of charged particles, enabling measurements of charge and momentum. It comprises three subdetectors, each employing distinct technologies, as shown in fig. 3.6. The innermost layer is the silicon pixel detector, followed by the SemiConductor Tracker (SCT), and finally the Transition Radiation Tracker (TRT). The pixel and SCT detectors provide high-resolution tracking at small radii, while the TRT extends tracking capability to larger radii, enhancing pattern recognition. The ID spans a radius of 2.3 meters and a length of 7 meters and operates within a 2 T solenoidal magnetic field. This magnetic field ensures sufficient bending of charged particles, facilitating precise momentum measurements. The pixel and SCT detectors provide tracking coverage up to $|\eta| < 2.5$, with the TRT extending coverage to $|\eta| < 2.0$.

Silicon Pixel Detector

The silicon pixel detector consists of three cylindrical layers in the barrel region and three disks on each endcap. The barrel layers are positioned at radii of 50.5 mm, 88.5 mm, and 122.5 mm, while the disks are located at $z = \pm 495$, ± 580, and ± 650 mm. Each module comprises 46080 pixels, with a pixel size of 50×400 μm in the barrel and 50×250 μm in

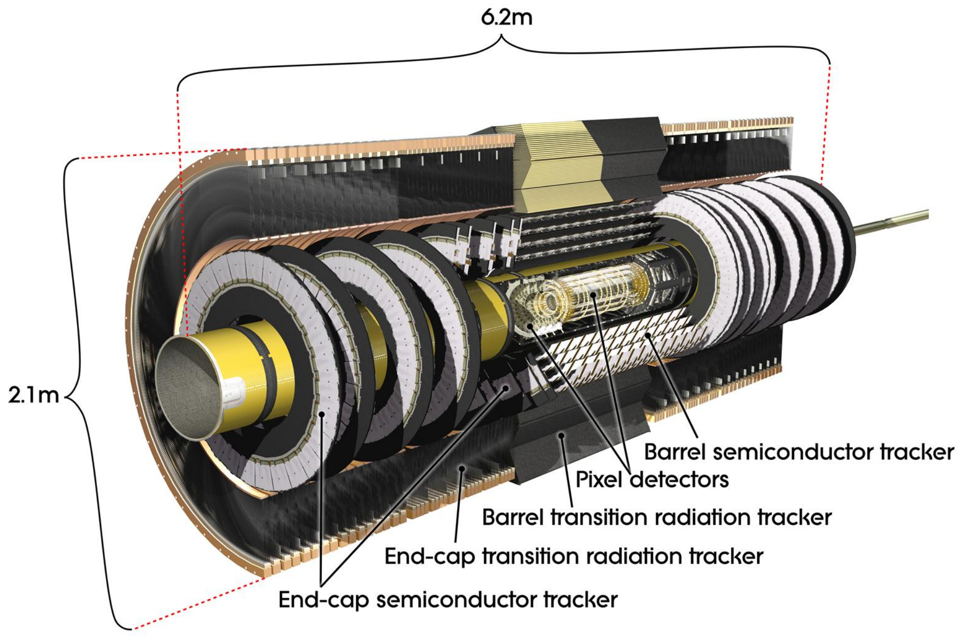

Figure 3.6: Schematic of the ATLAS inner tracker [33].

the Insertable B-Layer (IBL), an additional layer installed during LS1 to maintain tracking performance in high-luminosity conditions.

SemiConductor Tracker

The SCT is composed of silicon microstrip sensors arranged in four cylindrical layers in the barrel and nine disks in the endcaps. These layers provide high-precision tracking, with a spatial resolution of approximately 17 μm in the barrel and 16 μm in the endcaps. The SCT ensures precise measurements of charged-particle trajectories over a large detector volume.

Transition Radiation Tracker

The TRT consists of gas-filled drift tubes, or straws, which are 4 mm in diameter and contain a gas mixture of xenon (70%), CO_2 (27%), and O_2 (3%). These tubes detect transition radiation and contribute to electron identification. The TRT covers the range up to $|\eta| < 2.0$ and provides additional tracking information at large radii.

The combination of these three subdetectors allows the ATLAS ID to achieve excellent tracking performance, enabling precise vertex reconstruction, momentum measurement, and particle identification.

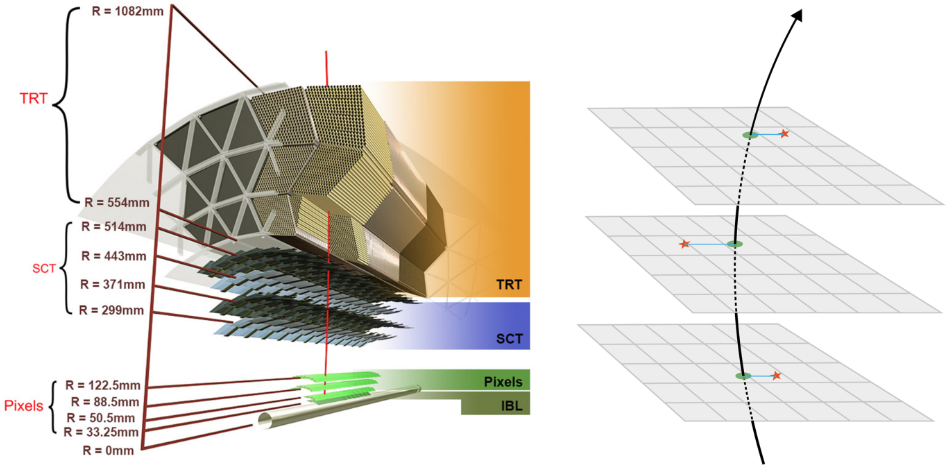

Figure 3.7: Cut-away view of one-quarter of the ATLAS ID [35].

3.2.2 Calorimeters

Surrounding the ID, the calorimeters are designed to absorb and measure the energy of incoming particles, enabling precise energy reconstruction and spatial localization of energy deposits. The ATLAS detector features two types of calorimeters. The Electromagnetic Calorimeter (ECal), positioned immediately outside the ID, is responsible for measuring electromagnetic showers within the pseudorapidity range $|\eta| < 3.2$. Additional coverage for electromagnetic interactions in the forward region ($3.1 < |\eta| < 4.9$) is provided by the Forward Calorimeter (FCal). Beyond the ECal, the Hadronic Calorimeter (HCal) measures the energy of hadronic showers. A schematic representation of the calorimeter system is shown in fig. 3.8.

Both the electromagnetic and hadronic calorimeters employ a sampling design, where alternating layers of active and passive materials allow energy measurements while requiring correction factors to determine the total deposited energy. In the barrel region, the ECal is housed within a cryostat, whereas in the endcaps, the ECal, HCal, and FCal are all enclosed in cryostats due to their proximity to the beamline.

Electromagnetic Calorimeter

The ECal utilizes a liquid argon (LAr) configuration, with lead acting as the passive absorber and LAr serving as the active detecting medium. Liquid argon is chosen for its linear response, long-term stability, and radiation tolerance, while the thickness of the lead layers

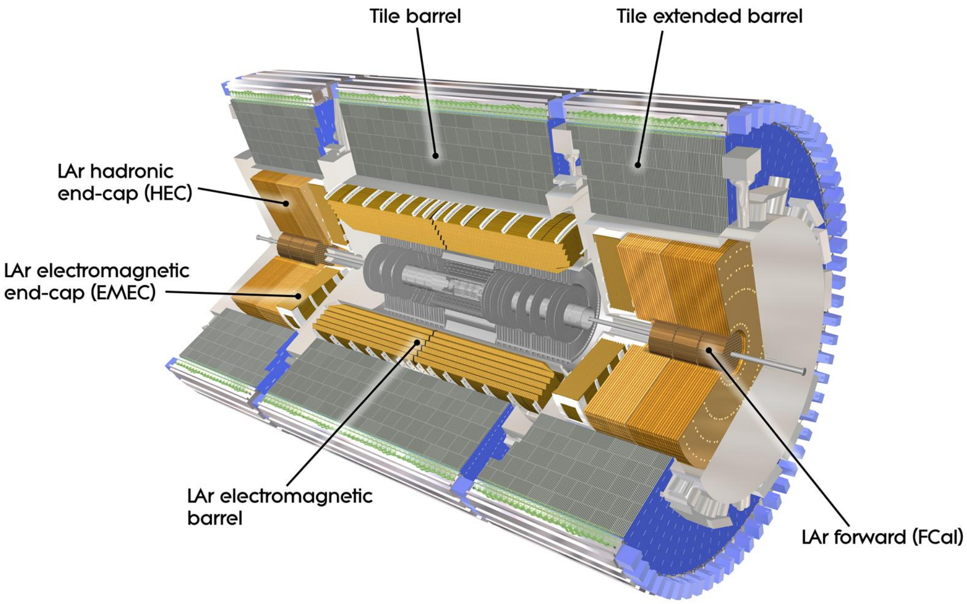

Figure 3.8: Calorimeters in the ATLAS detector [36].

is optimized for energy resolution. The ECal follows an accordion-shaped geometry, ensuring continuous ϕ coverage without azimuthal gaps. It is segmented into three layers for $|\eta| < 2.5$ and two layers for $2.5 < |\eta| < 3.2$. The barrel section consists of cylindrical modules, whereas the endcap section is structured into coaxial wheels.

A presampler layer, made of LAr, is positioned in front of the ECal to account for energy losses from electrons and photons before they reach the calorimeter. The presampler consists of 64 azimuthal sectors in the barrel and 32 in each endcap. The overall detector thickness varies between 22 and 33 radiation lengths (X_0) in the barrel and between 24 and 38 radiation lengths in the endcaps.

Hadronic Calorimeter

The HCal is more structurally complex than the ECal and is composed of three distinct regions: the Tile Calorimeter, the Hadronic Endcap Calorimeter (HEC), and the FCal.

The Tile Calorimeter, located in the barrel, surrounds the barrel ECal and extends over $|\eta| < 1.0$. Its extended barrel components cover $0.8 < |\eta| < 1.7$ on either side. This calorimeter utilizes steel as the absorbing material and scintillating tiles as the active detecting medium. It consists of three layers, ranging from 2.28 m to 2.45 m in radial distance, and is segmented azimuthally into 64 modules.

The HEC consists of two wheels, each containing two layers, positioned beyond the endcap ECal. It covers the pseudorapidity range $1.5 < |\eta| < 3.2$. Unlike the ECal, the HEC employs copper as its absorber material while still utilizing LAr as the active medium. The copper plate thickness varies: the innermost wheels use 25 mm plates, while the outermost wheels utilize 50 mm plates. The plates extend radially from 0.475 m to 2.03 m.

The FCal provides coverage in the very forward region, $3.1 < |\eta| < 4.9$, and consists of three modules. All three modules employ LAr as the active medium; however, the first module utilizes copper as the absorber to optimize electromagnetic measurements, while the second and third modules use tungsten to enhance hadronic energy measurement.

3.2.3 Muon Spectrometer

The Muon Spectrometer (MS) is the outermost and largest subdetector of the ATLAS experiment. It is designed to detect final-state muons and measure their momenta with high precision. The MS consists of four types of tracking chambers: Resistive-Plate Chambers (RPC), Thin-Gap Chambers (TGC), Monitored Drift Tubes (MDT), and Cathode Strip Chambers (CSC). A system of superconducting toroidal magnets bends the trajectories of muons, enabling momentum reconstruction. The layout of the MS, depicted in fig. 3.9, follows the standard ATLAS segmentation into a barrel region ($|\eta| < 1.0$) and an endcap region ($1.0 < |\eta| < 2.7$). The barrel chambers are arranged in three concentric stations around the beamline at radii of approximately 5 m, 7.5 m, and 10 m. The endcap chambers are positioned in four circular disks located at $z = \pm 7$, ± 10, ± 14, and ± 21-23 m, centered around the beamline.

Tracking in the MS is primarily provided by MDT chambers, which are present in both the barrel and endcap regions. In the forward region ($2.0 < |\eta| < 2.7$), CSCs are additionally used due to their superior capability to handle high particle flux and background levels. RPCs and TGCs are responsible for fast muon triggering, with RPCs installed in the barrel and TGCs in the endcaps.

Ideally, only muons and neutrinos can traverse the entire calorimeter system to reach the MS. However, due to the stochastic nature of hadronization, some hadronic particles may penetrate the calorimeters without being fully absorbed. These events are known as *punch-through jets* and contribute to the background in muon identification.

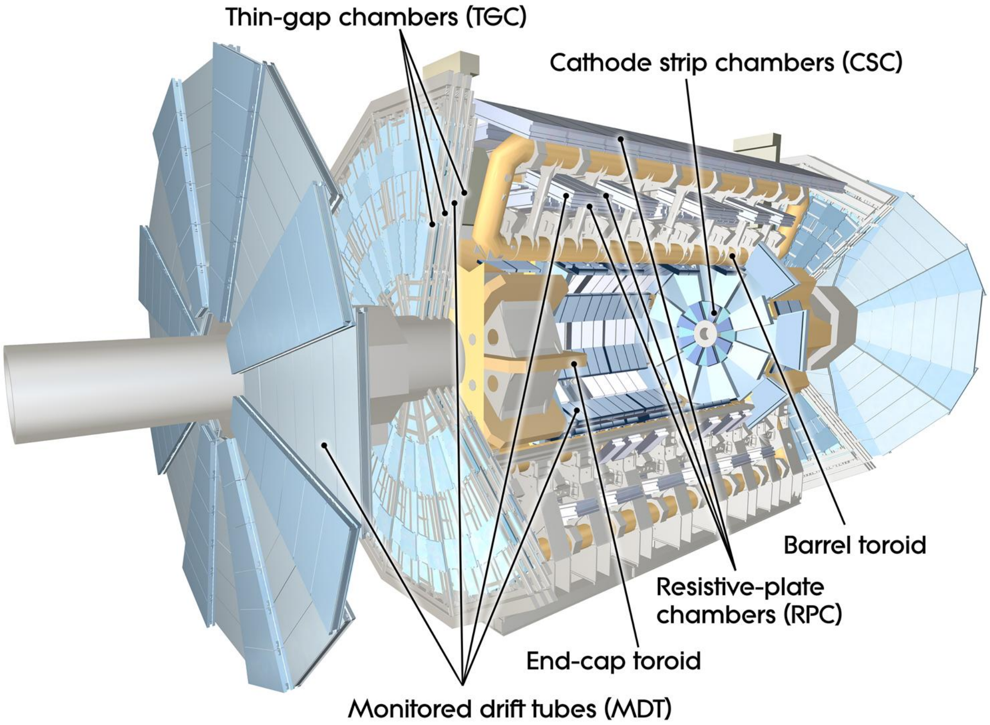

Figure 3.9: Schematic of the ATLAS Muon Spectrometer [37].

Monitored Drift Tubes

MDT chambers consist of two multilayers, each containing either four layers of drift tubes (for inner stations) or three layers (for middle and outer stations). The drift tubes are aluminum cylinders, 30 mm in diameter, with a central tungsten-rhenium wire of 50 μm diameter. The tubes are filled with a gas mixture of Ar-CH_4-N_2 at a pressure of 3 bar, providing a gas gain of 2×10^4. The length of MDT tubes varies between 70 cm and 630 cm depending on their location within the detector. The total number of MDT tubes across ATLAS is approximately 372,000, with an average position resolution of 80 μm per tube.

Cathode Strip Chambers

CSCs are multiwire proportional chambers designed for high-occupancy environments. They utilize tungsten-rhenium wires of 30 μm diameter and a gas mixture of Ar-CO_2-CF_4, achieving a gain of 10^4. CSCs simultaneously measure positions in both the z/R and ϕ directions, allowing them to handle significantly higher particle rates than MDTs. Due to this capability, CSCs replace MDTs in the innermost station of the forward region ($2.0 < |\eta| < 2.7$), where particle fluxes are highest.

Resistive-Plate Chambers

RPCs are used for muon triggering in the barrel region of the MS. Each chamber consists of two parallel resistive bakelite plates with a 2 mm gas gap, filled with 97% tetrafluoroethane ($C_2H_2F_4$) and 3% isobutane (C_4H_{10}). A uniform electric field of 4.5 kV/mm induces electron avalanches, and signals are capacitively read out on both sides of the chamber. The timing difference between these signals enhances the time resolution. Each chamber comprises two orthogonally oriented layers, providing independent measurements in the η and ϕ directions. The spatial resolution of RPCs is approximately 1 cm, with a time resolution of 1.5 ns.

Thin-Gap Chambers

TGCs serve as trigger detectors in the endcap region of the MS and operate similarly to CSCs. Each chamber contains anode wires held at 3100 V, spaced 1.8 mm apart, within a 2.8 mm gas gap. The small anode-cathode distance of 1.4 mm, which is smaller than the wire spacing, ensures fast signal response. The gas mixture consists of 55% CO_2 and 45% n-pentane (n-C_5H_{12}), providing a gain of 10^6. TGCs are crucial for rapid muon identification in the high-background forward region.

3.2.4 Trigger System

During Run 2 of the LHC, the nominal bunch spacing was 25 ns, resulting in an interaction rate of approximately 40 million proton-proton collisions per second. Given that each collision generates around 1 MB of data [38], it is not feasible to store all recorded events. Instead, a multi-level trigger system is employed to rapidly filter and retain only the most relevant events for analysis.

The ATLAS trigger system consists of two primary levels. The first level, known as Level 1 (L1), is hardware-based and makes rapid decisions using coarse detector information. It reduces the event rate from 40 MHz to approximately 100 kHz within 2.5μs. The second level, the HLT, employs more refined and high-granularity detector data to further process and filter events, ultimately reducing the data storage rate to around 1 kHz. A schematic representation of the trigger and data acquisition system used in Run 2 is shown in fig. 3.10.

The L1 trigger operates using a set of predefined trigger items, each designed to identify specific physics signatures. These include signatures from individual particles such as muons, electrons, photons, jets, and hadronically decaying τ-leptons, as well as global quantities like missing transverse energy (E_T^{miss}) and total transverse energy. When an event satisfies an L1 trigger condition, one or more Regions-of-Interest (RoIs) are defined, marking spatial regions in the detector where interesting activity has been identified. These RoIs serve as input seeds for the HLT, which then applies more refined selection criteria using full detector information to determine whether the event is retained.

Certain frequently occurring triggers, such as those corresponding to common Standard Model processes, may produce event rates exceeding the capacity of the data acquisition system. In such cases, a prescale factor is applied, meaning that only a fraction of the selected events are retained. For instance, a prescale of 4 implies that only one in every four events passing the trigger conditions is stored for further analysis.

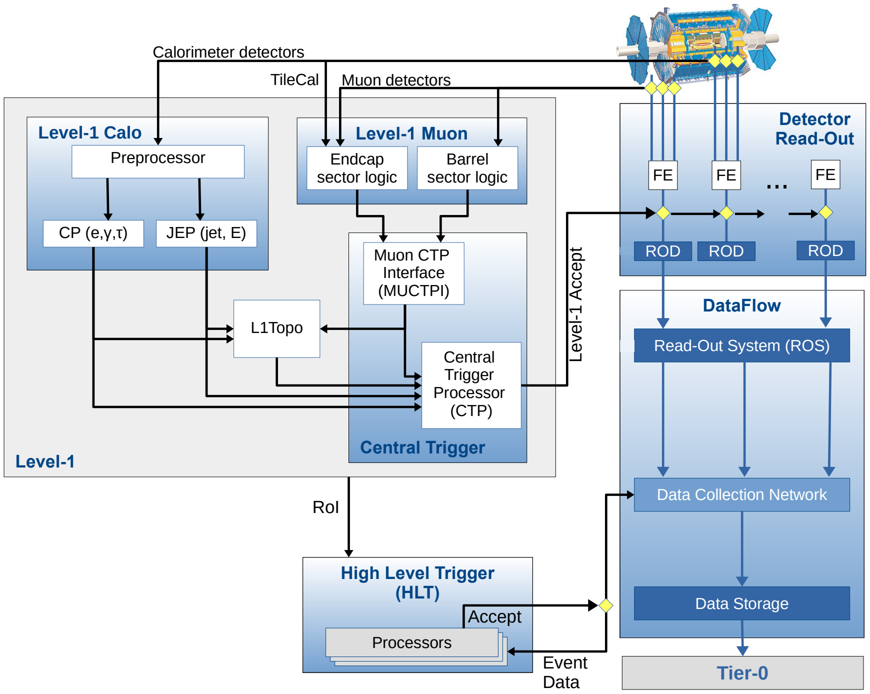

Figure 3.10: Schematic representation of the ATLAS trigger and data acquisition system during Run 2 [39].

3.3 High-Luminosity LHC and ATLAS upgrades

The High-Luminosity LHC (HL-LHC) is an upgrade of the LHC, aimed at significantly enhancing its performance. The timeline for the HL-LHC project is shown in Figure 3.11. The primary goal is to increase the delivered integrated luminosity by a factor of 5 to 7.5 compared to the LHC's achievements, with the potential to reach the originally designed center-of-mass energy of $\sqrt{s} = 14$ TeV. By the end of its operational lifetime, the HL-LHC is expected to achieve a total integrated luminosity of 3000 to 4000 fb^{-1}.

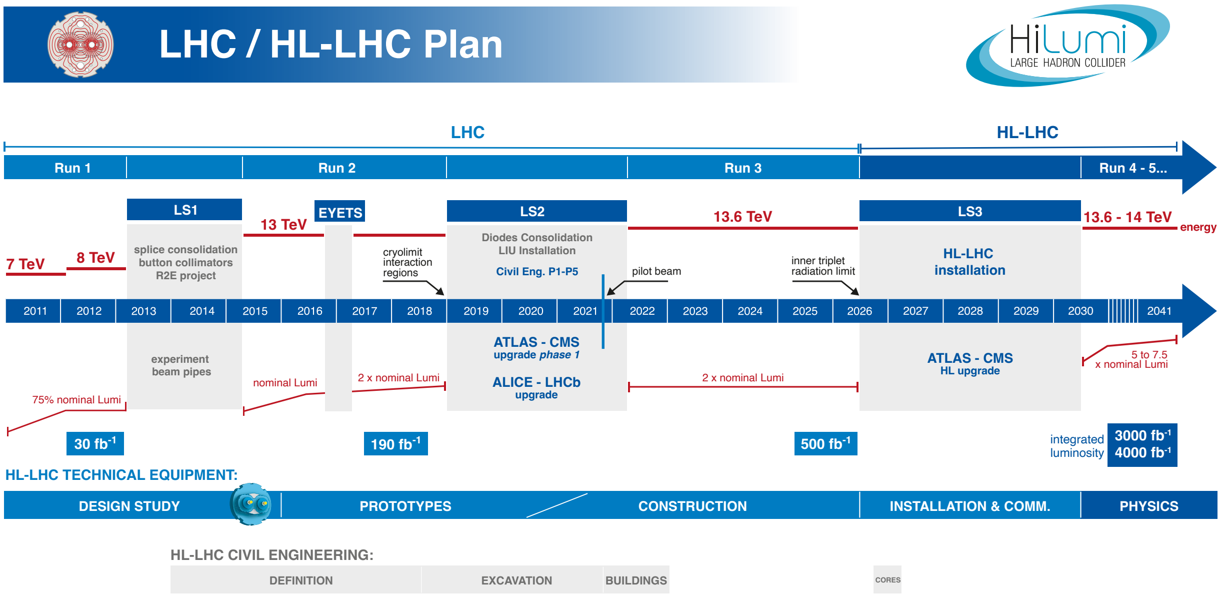

Figure 3.11: LHC/HL-LHC Plan updated in October 2024. [40]

Significant upgrades to the accelerator are in progress, including the implementation of advanced superconducting magnets and compact superconducting crab cavities designed for beam rotation [41]. The HL-LHC is expected to start operation in 2030. With this upgrade, the HL-LHC will be capable of producing over 15 million Higgs bosons per year, substantially enhancing the dataset available for investigating rare processes and potential exotic Higgs decays beyond the predictions of the SM.

However, the increase in instantaneous luminosity will result in a significantly higher number of interactions per bunch crossing, presenting substantial challenges for the current ATLAS detector and data acquisition systems. In the ultimate HL-LHC configuration, the instantaneous luminosity is expected to reach $L = 7.5 \times 10^{34}$ cm^{-2}s^{-1}, leading to up to 200 inelastic collisions per bunch crossing (commonly referred to as "pile-up"). To address these challenges, several upgrades to the ATLAS detector are planned during LS3 to ensure it can effectively operate under the demanding conditions of the HL-LHC. This discussion focuses on the upgrades to the Inner Tracker (ITk) and the Trigger and Data Acquisition systems.

Inner Tracker Detector: The ATLAS ITk is a new all-silicon-based inner detector designed to replace the current inner detector [42]. The ITk will provide improved impact parameter resolution, enabling more precise identification of hadrons containing b- and c-quarks. Additionally, the ITk will extend the pseudorapidity coverage in the forward region from $|\eta| < 2.5$ to $|\eta| < 4$, thereby increasing the detector's acceptance and coverage for forward events.

Trigger and Data Acquisition System: Several major upgrades to the trigger and data acquisition systems are being implemented to ensure efficient event selection under the high-luminosity conditions of the HL-LHC. A new Level-0 hardware trigger system will replace the existing Level-1 trigger, enabling a readout rate of 1 MHz with a maximum latency of 10 ms. Furthermore, an Event Filter system, utilizing a large processor farm, will take over the current High Level Trigger. This system will further reduce the event rate using advanced online algorithms and is designed to handle an output rate of 10 kHz for permanent storage, ensuring efficient data retention for subsequent analysis.

This advanced Event Filter system will leverage heterogeneous computing devices, such as GPUs and FPGAs, in combination with traditional CPUs to achieve both power savings and increased throughput. The scalability and throughput of the system are critical to accommodate the increased data rates. With the ITk detector expected to provide approximately 300k spacepoints, the system must support region-of-interest tracking at 1 MHz and full-scan tracking at 150 kHz.

To address these computational challenges, the concept of "Tracking as a Service" is being explored as one of my contributions. This approach introduces a flexible, service-oriented computing model designed to efficiently manage the high computational demands of tracking tasks, particularly for deep-learning-based tracking models such as Graph Neural Networks. By leveraging industry-standard libraries, such as NVIDIA Triton Inference Server [44], this model enables scalable and efficient deployment of advanced tracking algorithms.

I led the main developments of this concept through the ExaTrkX-as-a-Service framework,

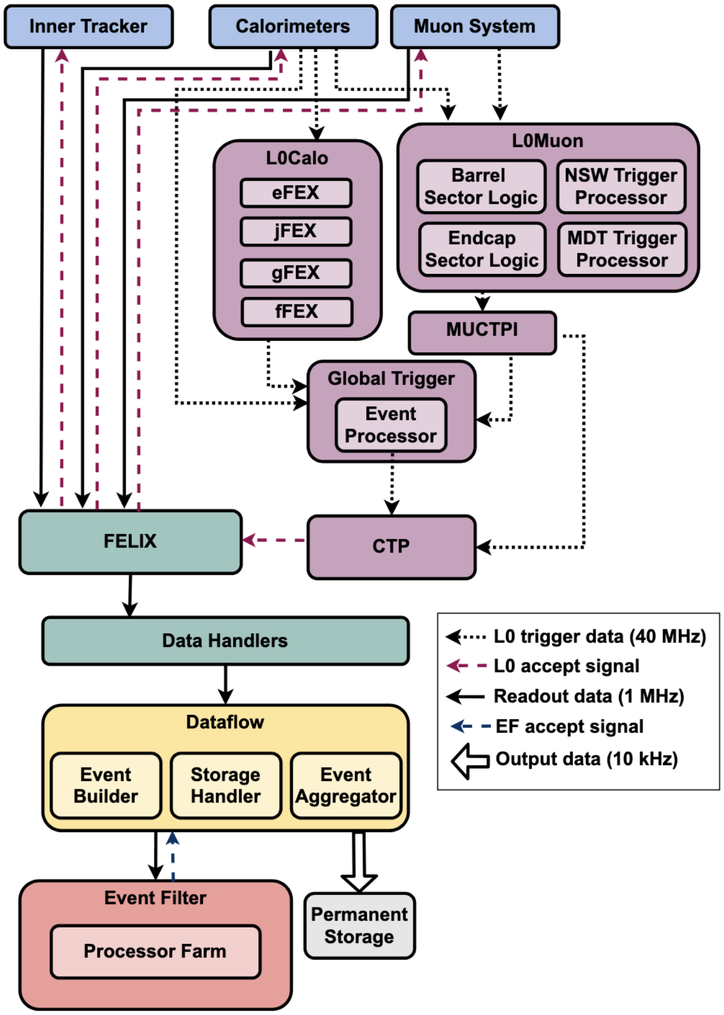

Figure 3.12: Trigger and Data Acquisition System in HL-LHC[43].

establishing its foundations and guiding further advancements. Detailed information about this work is provided in Appendix B.

Chapter 4

Object Definition

This chapter elucidates the methodologies implemented for object reconstruction within the ATLAS experiment, a critical component of physics analyses in high-energy particle collider experiments. At the detector interface, interactions between incident particles—including electrons, photons, and hadrons—and the detector material give rise to electrical signals. These signals are vital as they provide the raw data input for a sophisticated suite of software tools engineered for the reconstruction of various physics objects. The effective interpretation of these signals is pivotal for identifying the fundamental particles and their interaction processes, which are essential for advancing our understanding of particle physics.

4.1 Track and Vertex Reconstruction

Track and vertex reconstruction are foundational tasks in understanding the trajectories and origins of charged particles within particle physics experiments. These processes are achieved through a multi-stage approach that integrates advanced algorithms and precise detector measurements.

4.1.1 Track Reconstruction

Track reconstruction involves identifying and fitting the paths of charged particles as they traverse the inner detector. This process can be divided into five main stages:

1. **Clustering:** Adjacent hits in the detector are grouped together to form clusters, which are essential for resolving the trajectory of the particle.

2. **Spacepoint Formation:** Clusters in the Pixel and SCT subsystems are combined to create spacepoints, providing a three-dimensional reference for track reconstruction.

3. **Seeding:** Spacepoints are used to identify potential seeds for tracks, initiating the trajectory-building process.

4. **Track Finding:** Using seeded spacepoints, potential tracks are identified by extrapolating trajectories that are consistent with the detector geometry and magnetic field.

5. **Track Fitting:** The final step refines the trajectory by fitting it to the observed hits using algorithms such as the Kalman Filter, ensuring the best possible estimate of the particle's path.

The reconstructed tracks provide critical information about the particle's transverse momentum (p_T), pseudorapidity (η), and azimuthal angle (ϕ). Figure 4.1 illustrates the full chain of track reconstruction, from initial clustering to fully fitted tracks.

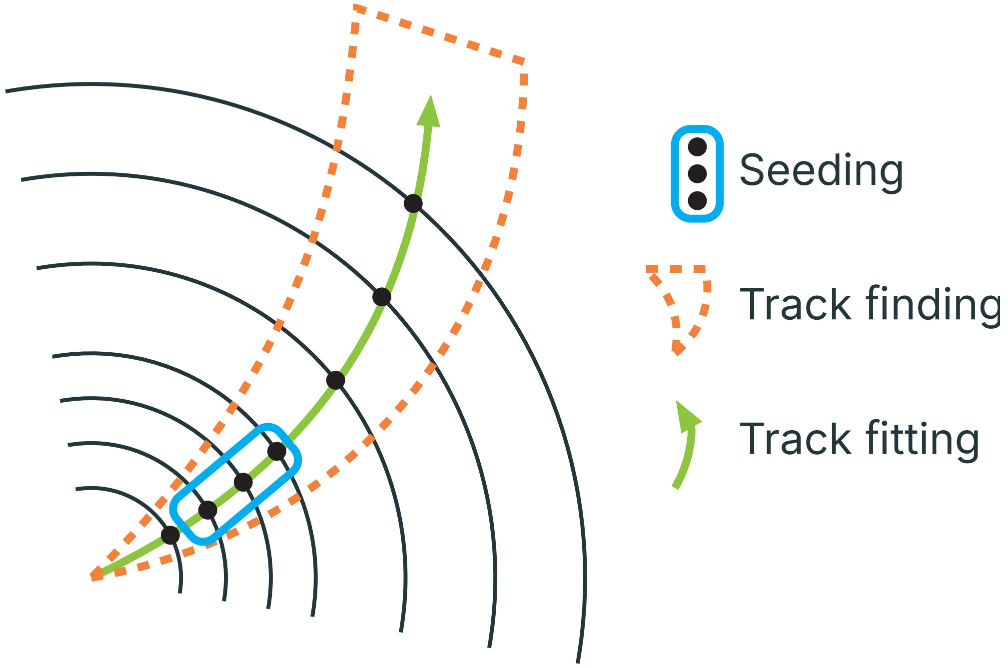

Figure 4.1: Illustration of a track reconstruction chain starting from clustering to fully formed tracks [45].

4.1.2 Vertex Reconstruction

Vertex reconstruction builds upon the reconstructed tracks to locate interaction points within the detector. These vertices are categorized into:

1. **Primary Vertices:** The collision point of two beam particles, including both hard-scatter and pile-up interactions. In collider experiments, the primary vertex is typically the one with the highest p_T, or “hard-scatter”, which is of primary interest, while others are classified as pile-up vertices. Accurate primary vertex reconstruction clusters charged-particle trajectories to these vertices, essential for determining the full kinematics of an event.

2. **Secondary Vertices:** Additional vertices that arise from the decay of long-lived particles or other secondary interactions within the detector.

The process involves clustering tracks that converge at a common point, indicative of a vertex. Algorithms such as iterative vertex fitting are used to optimize the precision and reliability of vertex identification. Figure 4.2 demonstrates the distinction between primary and pile-up vertices in a proton-proton collision.

Primary Vertex at HL-LHC

With the HL-LHC, primary vertex reconstruction faces new challenges. At peak luminosities of $7.5 \times 10^{34}\,\mathrm{cm}^{-2}\mathrm{s}^{-1}$ and $\sqrt{s} = 14$ TeV, up to 200 interactions per bunch crossing are expected, creating a dense environment. To address this, the ATLAS Phase-II Upgrade Program will replace the Inner Detector with an all-silicon ITk, composed of a Pixel Detector and a Strip Detector, which together extend tracking coverage up to $|\eta| = 4.0$ [46].

Vertex reconstruction in this context relies on the Adaptive Multi Vertex Finder (AMVF), a multi-vertex adaptive fitting algorithm optimized for dense event conditions. Originally developed for Run 3, AMVF demonstrates improved performance over the previous iterative method, and further optimizations are ongoing to prepare for the HL-LHC requirements [47].

My contributions to ATLAS, which involve studying and optimizing the AMVF for the ITk under simulated HL-LHC conditions, are detailed in A.

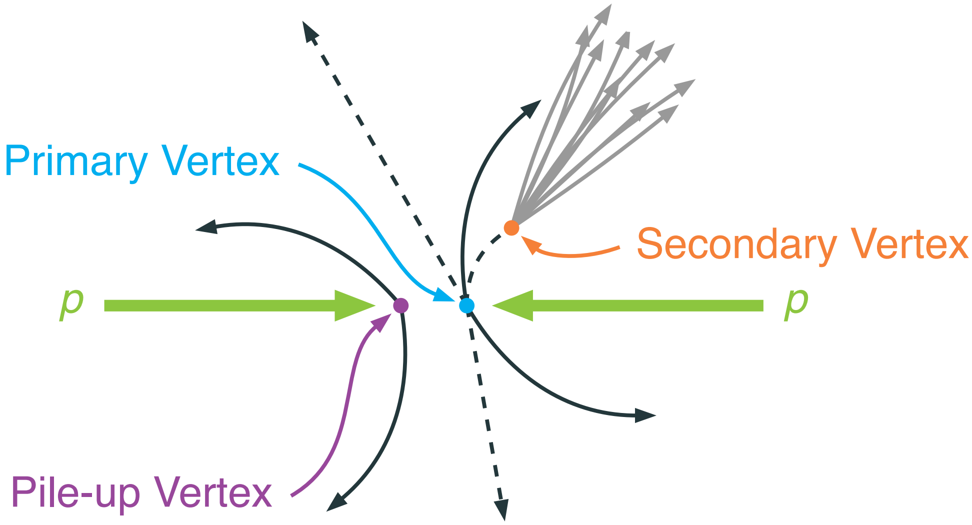

Figure 4.2: Illustration of a set of three vertices in a proton-proton collision. We distinguish between primary hard-scatter, primary pile-up, and secondary vertices [45].

4.2 Leptons

The accurate reconstruction and identification of leptons, specifically electrons and muons, are crucial for collider physics analyses. Leptons are identified through a multi-stage process involving **reconstruction**, **identification** and **isolation** Both electron and muon candidates must be associated with the primary vertex to reduce background contamination from secondary sources.

4.2.1 Electrons

Electrons are reconstructed by matching clusters of energy deposited in the electromagnetic calorimeter with tracks reconstructed in the inner detector. The identification of electrons relies on a likelihood-based (LH) discriminant, which evaluates multiple properties, including the shower shape, track quality, and the consistency between the track and cluster positions [48]. The LH discriminant defines three sets of identification working points: `LooseLH`, `MediumLH`, and `TightLH`, each with varying levels of signal efficiency and background suppression. The `LooseLH` working point achieves the highest signal efficiency with less stringent background rejection, while the `TightLH` working point prioritizes background suppression at the cost of reduced signal efficiency. These working points are valid within the pseudorapidity range $|\eta| < 2.47$. For typical electroweak processes, the signal efficiency is approximately 93%, 88%, and 80% for the `LooseLH`, `MediumLH`, and `TightLH` operating points, respectively, with efficiency increasing as a function of the transverse energy (E_T).

Isolation criteria further ensure that selected electrons are not accompanied by nearby hadronic activity, reducing the likelihood of misidentification. Different isolation working points, such as `FCTight` and `Gradient`, are applied based on the analysis requirements. The `Gradient` isolation working point shows a strong pile-up dependence, with isolation efficiency decreasing from approximately 95% at low pile-up to around 85% at high pile-up conditions.

4.2.2 Muons

Muons are reconstructed by correlating tracks in the muon spectrometer with those in the inner detector, complemented by calorimeter-based identification methods [49, 50]. The identification of muons follows a set of stringent criteria that prioritize track integrity, compatibility with muon spectrometer information, and isolation from other event components.

Similar to electrons, muon identification uses multiple working points, including `Loose`, `Medium`, and `Tight`, which are defined to balance between signal efficiency and background rejection. The `Loose` working point is used to select baseline muons, while `Medium` and `Tight` are applied to signal muons depending on the analysis requirements. In the WZ analysis, the muon associated with the W boson is identified using the `Tight` Working Point (WP) due to stricter background rejection needs, while the `Medium` WP suffices for muons from the Z boson. For the same-sign WW analysis, the `Medium` WP is used for signal muons, paired with the `FixedCutPflowTight` isolation criterion to handle pile-up effects.

A summary of the lepton selection criteria and WPs adopted in the analyses that contribute to the combination is provided in this section in Table 4.1.

Table 4.1: Lepton identification and isolation WPs used in the signal regions for the two channels entering the combination.

Analysis / Working Points	$H_5^{\pm} \to W^{\pm}Z$	$H_5^{\pm\pm} \to W^{\pm}W^{\pm}$
Electron identification	`TightLH` (W) / `MediumLH` (Z)	`TightLH`
Electron isolation	`FCTight`	`Gradient`
Muon identification	`Tight` (W) / `Medium` (Z)	`Medium`
Muon isolation	`FCTight`	`FixedCutPflowTight`

4.2.3 Tau Leptons

The ATLAS detector is capable of identifying tau leptons, primarily through their hadronic decays, which produce a neutrino and a set of visible decay products. These visible decay products typically include one or three charged pions, accompanied by up to two neutral pions. Tau candidates are reconstructed as narrow, collimated jets (see section 4.3) and are classified based on the number of associated tracks.

Although tau leptons can appear in multilepton final states through decays of W/Z bosons or diboson processes, they are not included in this analysis. The reconstruction and identification of hadronically decaying taus introduce additional complexities and uncertainties, and their omission simplifies the object selection while maintaining sensitivity to the targeted signal processes.

4.3 Jets

Jets are complex physical phenomena in particle physics, represented by a collection of particles produced by the hadronization of quarks and gluons. These particles are emitted in tight bunches or streams following high-energy collisions, primarily studied in experiments like ATLAS to understand the fundamental aspects of QCD. The jet formation process is illustrated in Figure 4.3, which highlights the key stages of jet production: collision, fragmentation, and hadronization.

The reconstruction of jets is standardized across the analyses presented, utilizing the anti-k_t algorithm with a radius parameter $R = 0.4$, and leveraging particle-flow objects as input constituents [52, 53]. The anti-k_t algorithm clusters particles based on their p_T and angular separation, favoring the merging of particles with high p_T while preserving the conical jet shape. This is achieved by iteratively combining the closest pair of particles or merging a particle with an existing jet according to distance metrics defined by

$$d_{ij} = \min(p_{T,i}^{-2}, p_{T,j}^{-2}) \frac{\Delta R_{ij}^2}{R^2}, \quad d_{iB} = p_{T,i}^{-2}, \tag{4.1}$$

where ΔR_{ij} is the distance between two particles i and j in the $\eta - \phi$ plane. This algorithmic choice ensures robust jet performance while minimizing susceptibility to pile-up effects, as it tends to cluster soft particles at the boundaries of the jet, reducing contamination from

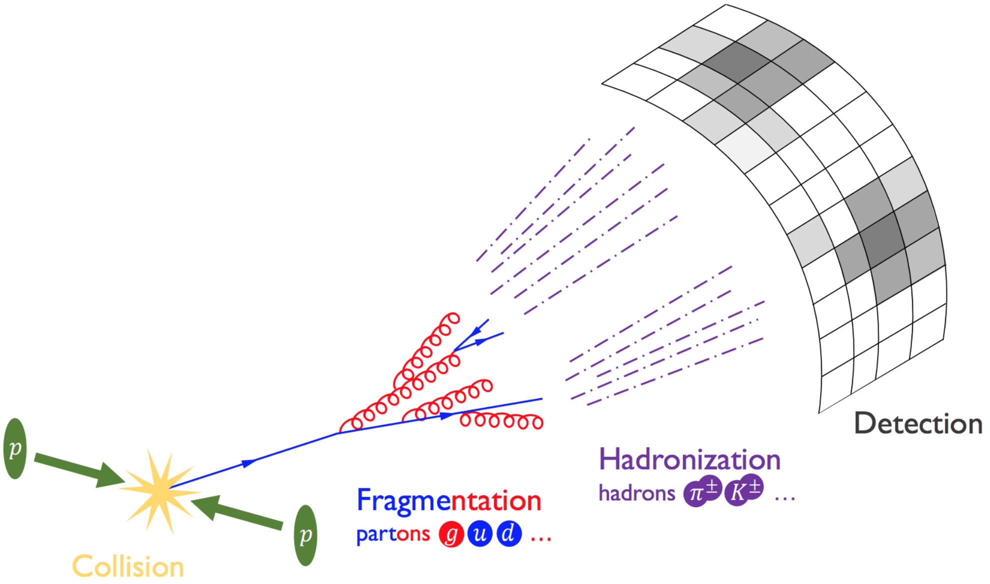

Figure 4.3: Jet formation process. Protons collide, leading to energetic partons. The partons fragment into a fractal-like structure of quarks and gluons, which subsequently hadronize into observable particles[51].

low-p_T pile-up contributions.

Jet candidates are required to satisfy stringent kinematic criteria: the absolute pseudorapidity ($|\eta|$) must not exceed 4.5, and p_T thresholds vary by analysis—30 GeV for the WZ channel and 25 GeV for the same-sign WW analysis. These criteria ensure that jets are within the detector's optimal sensitivity range and contribute meaningfully to the physical analysis.

Further advancements in jet reconstruction include techniques like pile-up mitigation algorithms, grooming methods such as Soft Drop, and tagging approaches like b-tagging or quark/gluon discrimination, which enhance the resolution and reduce biases in experimental analyses. These techniques are essential for distinguishing jets originating from different physics processes and improving the accuracy of signal and background separation.

The flavor of each jet is ascertained through a sophisticated deep-learning neural network, `DL1r`, which exploits the unique decay signatures of b-hadrons—particularly the impact parameters of associated tracks and the positions of displaced vertices within the inner detector. An operational efficiency of 85% is targeted for b-tagging, applying scale factors to adjust for any deviations observed in simulation relative to real data conditions [54, 55].

To further enhance the fidelity of jet reconstruction amid the challenging environment posed by pile-up, a Jet Vertex Tagger (JVT) is employed. This algorithm is crucial for jets with $p_T < 60$ GeV and $|\eta| < 2.4$, ensuring that these jets are indeed originating from the primary vertex [56, 57]. Additionally, in the WZ analysis, jets that fall within the forward region ($2.5 < |\eta| < 4.5$ and $p_T > 120$ GeV) must pass the forward JVT criterion, reflecting a tailored approach to mitigating pile-up in regions where it is most pronounced [58].

The precision of jet energy measurement is governed by the Jet Energy Scale (JES) and Jet Energy Resolution (JER) models, which are meticulously calibrated against a suite of in-situ measurements and simulation studies [59]. These models are vital for ensuring that the energy and momentum of reconstructed jets are accurately represented. Detailed specifications of the jet selection criteria are encapsulated in Table 4.2.

Table 4.2: Jet definition and configurations used for the two channels entering the combination.

Configuration \ Analysis	$H_5^{\pm} \to W^{\pm}Z$	$H_5^{\pm\pm} \to W^{\pm}W^{\pm}$
Jet Collections	`AntiKt4EMPFlow`	`AntiKt4EMPFlow`
Jet $\|\eta\|$ cut	< 4.5	< 4.5
Jet p_T cut	> 30 GeV	> 25 GeV
Pile-up tagging (central jets)	JVT `medium` WP	JVT `tight` WP
Pile-up tagging (forward jets)	fJVT `loose` WP	
b-tagging veto	`DL1r` @ 85%	`DL1r` @ 85%
JES model	`GlobalReduction`	`CategoryReduction`
JER model	`SimpleJER`	`FullJER`

4.4 Missing Transverse Momentum

Missing transverse momentum, denoted as $E_{\mathrm{T}}^{\mathrm{miss}}$, quantifies the imbalance in transverse momentum in an event, attributed to particles that escape detection. These particles include neutrinos and potentially new particles that interact weakly with the detector material. The $E_{\mathrm{T}}^{\mathrm{miss}}$ is critical in experiments like those conducted at the LHC, especially within the ATLAS detector, for probing physics beyond the SM.

The $E_{\mathrm{T}}^{\mathrm{miss}}$ vector, $\vec{E}_T^{\mathrm{miss}}$, is calculated as the negative vector sum of the transverse momenta ($\vec{p}_T$) of all observed physics objects:

$$E_T^{\mathrm{miss}} = \sqrt{(E_{\mathrm{miss},x}^2 + E_{\mathrm{miss},y}^2)}$$

where

$$E_{\text{miss},x(y)} = -\left(\sum_{\text{electrons}} p_T^e + \sum_{\text{photons}} p_T^\gamma + \sum_{\text{hadronic }\tau} p_T^{\tau_{\text{had}}} + \sum_{\text{muons}} p_T^\mu + \sum_{\text{jets}} p_T^{\text{jet}} + \sum_{\text{unused tracks}} p_T^{\text{track}}\right)$$

This calculation comprises contributions from “hard objects”—electrons, photons, tau leptons, muons, and jets—as well as “soft signals” from residual tracks not associated with any identified object but originating from the primary vertex.

A minimum threshold of $E_{\mathrm{T}}^{\text{miss}} > 25\,\text{GeV}$ for the WZ analysis and $E_{\mathrm{T}}^{\text{miss}} > 30\,\text{GeV}$ for the same-sign WW analysis is applied to each candidate event, ensuring relevance to the study objectives.

4.5 Treatment of Overlapping Objects

Effective identification of final-state objects requires that the detector response to a single physical object is not mistakenly reconstructed as multiple objects. To address this, an overlap removal procedure is employed using the “OverlapRemovalTool” [60, 61], which is designed to ensure accurate object reconstruction by resolving ambiguities in detector signals.

WZ Channel Criteria

For the WZ analysis, the “Standard” working point of the “OverlapRemovalTool” is applied. Specific rules include:

- If two electrons share the same track, the electron with lower p_{T} is discarded.
- Electrons that overlap with a muon track (from the muon spectrometer) are discarded. Conversely, if the muon is only calorimeter-tagged, it is the muon that is rejected.
- A jet closer than $\Delta R < 0.2$ to an electron is removed; if a jet is located within $0.2 < \Delta R < 0.4$ of an electron, then the electron is removed instead.
- Jets overlapping with muons by $\Delta R < 0.2$ are removed if they contain fewer than three tracks or if the discrepancies between the muon's energy and the jet's momentum are minimal. A muon is removed if it is within $\Delta R < 0.4$ of a jet and other conditions do not apply.

Same-sign WW Channel Criteria

In the same-sign WW analysis, the criteria adjust for increased stringency:

- Non-b-jets overlapping with an electron or muon within $\Delta R < 0.2$ and possessing fewer than three associated tracks (each with $p_{\mathrm{T}} > 500$ MeV) are removed.
- Electrons or muons overlapping with any jets (including b-jets) within $\Delta R < 0.4$ are removed.
- Electrons sharing an identification ID track with muons are removed to prevent misidentification.

Chapter 5

Data and Monte Carlo Samples

This chapter provides a brief description of the data and MC samples used in the q/g tagging calibration and the Charged Higgs combination analysis. Collision data from proton-proton (pp) collisions recorded by the ATLAS detector during the LHC Run 2 period (2015-2018) and various simulated event samples are detailed below.

5.1 Collision Data

The analysis utilizes pp collision data recorded by the ATLAS detector at a center-of-mass energy of $\sqrt{s} = 13$ TeV between 2015 and 2018. The dataset corresponds to an integrated luminosity of 140 fb^{-1} with an uncertainty of 0.83% [19, 62]. Events included in the analysis were collected during periods of stable beams and satisfy stringent data quality criteria as specified in the Good Run List (GRL) [63]. The relevant GRL files for each year are as follows:

```
data15_13TeV.periodAllYear_DetStatus-v89-pro21-02_Unknown_PHYS_StandardGRL_All_Good_25ns.xml
data16_13TeV.periodAllYear_DetStatus-v89-pro21-01_DQDefects-00-02-04_PHYS_StandardGRL_All_Good_25ns.xml
data17_13TeV.periodAllYear_DetStatus-v99-pro22-01
 _Unknown_PHYS_StandardGRL_All_Good_25ns_Triggerno17e33prim.xml
data18_13TeV.periodAllYear_DetStatus-v102-pro22-04
 _Unknown_PHYS_StandardGRL_All_Good_25ns_Triggerno17e33prim.xml
```

Quark/Gluon Tagging Calibration

For the q/g tagging analysis, the single jet Level-1 trigger `L1_J100` was used, followed by the lowest unprescaled small-R single-jet High-Level Trigger `HLT_j420`, which has a jet p_{T} threshold of 420 GeV. This trigger was chosen to ensure consistent selection across all years, despite the lower threshold of 360 GeV used in 2015. Multi-jet events were processed using the un-skimmed DAOD_JETM1 derivation scheme.

Charged Higgs combination analysis

Individual analyses utilizes different triggers and derivation due to the final state signatures. For the WZ analysis, events were selected using the DAOD_STDM5 derivation scheme, which retains events with at least three identified leptons with $p_{\mathrm{T}} > 6$ GeV. Meanwhile, the same-sign WW analysis utilized the DAOD_STDM3 derivation scheme for events with at least two identified leptons. The WZ analysis also made use of a strong skimming applied during derivation, while the tags p4095, p4096, and p4097 were employed. Similarly, for the same-sign WW analysis, samples were tagged with p3975, p4097, and p4252 depending on the sample.

Table 5.1: Summary of the single-lepton High-Level Trigger (HLT) used in this analysis.

	2015	2016 − 2018
Single muon	HLT_mu20_iloose_L1MU15 HLT_mu50	HLT_mu26_ivarmedium HLT_mu50
Single electron	HLT_e24_lhmedium_L1EM20VH HLT_e60_lhmedium HLT_e120_lhloose	HLT_e26_lhtight_nod0_ivarloose HLT_e60_lhmedium_nod0 HLT_e140_lhloose_nod0

5.2 MC Samples for Quark/Gluon Tagging

Multi-jet events are generated using various MC simulations and processed with the same `DAOD_JETM1` derivation framework as applied to the data. The nominal results are obtained using the Pythia 8.230 MC generator, which incorporates leading-order (LO) Matrix Element (ME) calculations for dijet production. To evaluate systematic uncertainties, the NNPDF2.3 LO parton distribution function (PDF) set is used in conjunction with Pythia.

Alternative samples are used to estimate systematic uncertainties, incorporating variations in parton shower modeling, ME generation, and multi-parton interaction (MPI) simulations. These follow the recommendations of the Physics Modeling Group (PMG) for jet processes [64]. However, some estimations are not ideal. For example, while the baseline generator is PYTHIA, the hadronization uncertainty is evaluated using SHERPA with a different PDF set. Strictly speaking, this approach is not optimal, as only one variable should be varied at a time. Unfortunately, fully consistent samples following the ideal scheme are either unavailable or challenging to implement.

Two sets of MC samples generated using SHERPA2.2.5 are employed to evaluate uncertainties related to hadronization modeling. Both samples utilize the CT10 PDF set and LO ME calculations for the $2 \rightarrow 2$ process. One set uses cluster hadronization, while the other employs the SHERPA interface to the Lund string fragmentation model as implemented in PYTHIA8.230.

For parton shower uncertainties, two sets of MC samples generated using HERWIG7.1.3 are utilized. One set employs angular-ordered showers, while the other uses dipole showers. These samples are produced at NLO accuracy with the MMHT PDF set.

To evaluate uncertainties from the ME , an additional set of multi-jet samples is produced using POWHEG-BOX interfaced with PYTHIA8 at NLO accuracy. These samples use the NNPDF2.3 LO PDF set and include variations in the perturbative scales within the ME and PDFs.

The renormalization and factorization scales are set to the transverse momentum (p_{T}) of the underlying Born configuration in all cases. A list of the MC samples used in this calibration is presented in Table 5.2.

Table 5.2: Monte Carlo simulations used for the multi-jet processes in this calibration. The table summarizes the PDF sets, event generators, parton shower models, and the order in α_s used for cross-section calculations and yield normalization [65].

PDF Set	Generator	Cross-Section	Parton Shower	Hadronization
NNPDF2.3	PYTHIA8 (v.235)	LO	p_{T}-ordered	String
CT10	SHERPA2.2.5	LO	p_{T}-ordered	Cluster
CT10	SHERPA2.2.5	LO	p_{T}-ordered	String
MMHT	HERWIG7.1.3	NLO	Dipole	Cluster
MMHT	HERWIG7.1.3	NLO	Angular-ordered	Cluster
NNPDF2.3	POWHEG-BOX+PYTHIA8	NLO	p_{T}-ordered	String

5.3 MC Samples for Charged Higgs Combination

Signal kinematic distributions, including those predicted by the GM model, are simulated using MC techniques. Background processes are modelled using a combination of MC simulation and data-driven methods. All samples are generated within the ATLAS simulation framework [66] and processed with GEANT4 [67]. The impact of multiple proton–proton interactions per bunch crossing (pile-up) is incorporated by overlaying the hard-scatter event with minimum-bias interactions simulated using PYTHIA 8.186 [68], employing the NNPDF2.3LO parton distribution functions [69] and the A3 set of tuned parameters [70].

5.3.1 Signal Samples

For the singly charged Higgs $H_5^{\pm}$ in the GM model, signal samples were generated with NLO precision in QCD, These span a mass range from 200 to 1000 GeV. The generation[1] utilized the athena version MCProd,20.7.9.9.27 and MADGRAPH5_aMC@NLO 2.7.2 with PYTHIA8 (v8.240).

For the doubly charged Higgs $H_5^{\pm\pm}$, MADGRAPH5_aMC@NLO 2.9.5 was used to generate the sample[2] at LO using interfaced with PYTHIA8 (v8.245). The targeted mass range for these simulated samples extended from 200 up to 3000 GeV.

For both signal samples, the signal simulation is produced using the `H5plane` bench-

---

[1] JIRA tickets documenting the generation procedure [71, 72]

[2] JIRA ticket documenting the generation procedure [73]

mark [31]. In addition, the $\sin\theta_{\mathrm{H}}$ values are set to 0.5 for mass points up to 800 GeV and 0.25 for higher mass samples, consistent with the existing constraints. An overview of the charged Higgs mass points that enter each individual fit, as well as the combination, is provided in Table 5.3. To ensure uniformity in the QCD accuracy of the two distinct signal sample sets for subsequent analysis, a normalization step is implemented. This step adjusts the samples to a uniform NNLO accuracy based on the cross-section values documented in the Higgs Cross-Section Working Group's recommendations [74] (see Tables 140, 141, 142, and 143[3]). To compute the NNLO K-factors, the signal samples used in this analysis have to be scaled[4] to $\sin\theta_{\mathrm{H}} = 1$, since this is the prescription used in Ref. [74]. In addition, the MadGraph MC samples simulate fully leptonic decays of VBF VV final states, and therefore, the cross-section has to be corrected by $1/\mathcal{B}(VV \to \text{fully leptonic})$, where $VV = W^{\pm}Z, W^{\pm}W^{\pm}$. The NNLO K-factors obtained are reported in Table 5.4.

5.3.2 Background Samples

The channel $H_5^{\pm} \to W^{\pm}Z$ is predominantly backgrounded by the SM $W^{\pm}Z$ processes, notably the QCD-mediated ($W^{\pm}Zjj-$QCD) and electroweak ($W^{\pm}Zjj-$EW) contributions. In the $W^{\pm}Zjj-$EW sample, a minor but non-negligible interference between the EW and QCD $W^{\pm}Z$ production is accounted for. The $W^{\pm}Zjj-$QCD background is simulated with Sherpa 2.2.2 [75], whereas the $W^{\pm}Zjj-$EW background is crafted using MadGraph 2.7.3 in conjunction with Pythia 8.244, employing the A14 tune [76]. Furthermore, diboson ($q\bar{q} \to ZZ \to 4\ell$ and $q\bar{q} \to ZZ \to \ell\ell\nu\nu$) and triboson event samples are generated with Sherpa 2.2.2 [77]. The $t\bar{t}V$ processes are modeled at NLO in QCD using the MadGraph 2.3.3 generator [78]. To address backgrounds with at least one misidentified or non-prompt lepton —encompassing $Z\gamma$, $W\gamma$, the Drell-Yan $Z \to \ell\ell$, $W \to \ell\nu$, top-quark pairs, and single top-quark processes— various generators have been employed. These samples are integral to the estimation of the fake/non-prompt lepton background. Elaborate details of these simulations are delineated in Table 5.5.

As for the backgrounds in the $H_5^{\pm\pm} \to W^{\pm}W^{\pm}$ channel, the SM $W^{\pm}W^{\pm}jj$ backgrounds

---

[3] Some of the mass points used in this analysis are not displayed in the Tables (multiples of 25, such as 225, 275, 325, 375, etc.). However, the granularity of the mass points provided is dense enough to do an interpolation by averaging the cross-sections of the adjacent mass points in each case.

[4] Note that the opposite approach can be followed, scaling the cross-section values published in Ref. [74] instead.

Table 5.3: Summary of the charged Higgs mass points in the combination analysis.

H_5 mass point [GeV]	$H_5^{\pm}$	$H_5^{\pm\pm}$	Combined
200	*	*	*
225	*	*	*
250	*	*	*
275	*	*	*
300	*	*	*
325	*	*	*
350	*	*	*
375	*	*	*
400	*	*	*
425	*	*	*
450	*	*	*
475	*	*	*
500	*	*	*
525	*	*	*
550	*	*	*
600	*	*	*
700	*	*	*
800	*	*	*
900	*	*	*
1000	*	*	*
1500		*	
2000		*	
3000		*	

Table 5.4: Summary of the NNLO K-factors applied to the NLO (LO) $H_5^{\pm}$ ($H_5^{\pm\pm}$) mass points in the combination analysis.

H_5 mass point [GeV]	$H_5^{\pm}$ NLO sample	$H_5^{\pm\pm}$ LO sample
200	1.01	1.16
225	1.01	1.08
250	1.00	1.21
275	1.01	1.14
300	0.96	1.24
325	1.03	1.18
350	0.97	1.25
375	0.99	1.20
400	0.98	1.27
425	1.01	1.22
450	1.02	1.27
475	1.09	1.23
500	1.05	1.28
525	1.21	1.28
550	1.24	1.29
600	1.26	1.29
700	1.23	1.30
800	1.33	1.32
900	1.29	1.32
1000	1.30	1.33
1500		1.38
2000		1.46
3000		0.44

Table 5.5: Summary of background MC simulation in the WZ channel [79].

DSID	Process	Generators	PDF	Filter eff.	Cross-section [pb]	k-factor	status
364253	WZ $\to \ell\nu\ell\ell$	Sherpa 2.2.2	NNPDF30NNLO	1.00	4.583	1.00	nominal
361292	WZ $\to \ell\nu\ell\ell$	Madgraph+Pythia8	A14NNPDF23LO	0.326	1.720	1.00	alternative
361293	WZ $\to \ell\nu\ell\ell$	Madgraph+Pythia8	A14NNPDF23LO	0.326	1.720	1.00	alternative
361601	WZ $\to \ell\nu\ell\ell$	Powheg+Pythia8	NLO CT10	1.00	4.5023	1.00	alternative
364739	WZjj + tZ: WZ $\to e^-\nu\mu\mu$, WZ $\to \mu^-\nu ee$	MadGraph+Pythia8	NNPDF30NLO	1.00	0.01543	1.00	nominal
364740	WZjj + tZ: WZ $\to e^+\nu\mu\mu$, WZ $\to \mu^+\nu ee$	MadGraph+Pythia8	NNPDF30NLO	1.00	0.02567	1.00	nominal
364741	WZjj + tZ: WZ $\to \mu^-\nu\mu\mu$, WZ $\to e^-\nu ee$	MadGraph+Pythia8	NNPDF30NLO	1.00	0.00770	1.00	nominal
364742	WZ EW: WZ $\to \mu^+\nu\mu\mu$, WZ $\to e^+\nu ee$	MadGraph+Pythia8	NNPDF30NLO	1.00	0.01281	1.00	nominal
830000	WZjj + tZ: WZ $\to e^-\nu\mu\mu$, WZ $\to \mu^-\nu ee$	MadGraph+Herwig	CT10 (ME), MMHT2014lo68cl (shower/MPI)	1.00	0.0154	1.00	alternative
830001	WZjj + tZ: WZ $\to e^+\nu\mu\mu$, WZ $\to \mu^+\nu ee$	MadGraph+Herwig	CT10 (ME), MMHT2014lo68cl (shower/MPI)	1.00	0.0257	1.00	alternative
830002	WZjj + tZ: WZ $\to \mu^-\nu\mu\mu$, WZ $\to e^-\nu ee$	MadGraph+Herwig	CT10 (ME), MMHT2014lo68cl (shower/MPI)	1.00	0.00770	1.00	alternative
830003	WZ EW: WZ $\to \mu^+\nu\mu\mu$, WZ $\to e^+\nu ee$	MadGraph+Herwig	CT10 (ME), MMHT2014lo68cl (shower/MPI)	1.00	0.0128	1.00	alternative
364250	ZZ QCD: $\ell\ell\ell\ell$	Sherpa 2.2.2	NNPDF30NNLO	1.00	1.2523	1.00	nominal
364254	ZZ QCD: $\ell\ell\nu\nu$	Sherpa 2.2.2	NNPDF30NNLO	1.00	1.2501	1.00	nominal
364283	ZZ EWK: $\ell\ell\ell\ell$	Sherpa 2.2.2	NNPDF30NNLO	1.00	0.01057	1.00	nominal
345705	$gg \to \ell\ell\ell\ell(m_{4\ell} < 130)$	Sherpa 2.2.2	NNPDF30NNLO	1.00	0.0099577	1.00	nominal
345706	$gg \to \ell\ell\ell\ell(m_{4\ell} > 130)$	Sherpa 2.2.2	NNPDF30NNLO	1.00	0.010163	1.00	nominal
361603	$q\bar{q} \to ZZ \to \ell\ell\ell\ell$	Powheg+Pythia8	NLO CT10	1.00	1.269	1.08	alternative
361604	$q\bar{q} \to ZZ \to \ell\ell\nu\nu$	Powheg+Pythia8	NLO CT10	1.00	0.92208	1.08	alternative
361040-361141	Z+jets	Sherpa 2.2.1	NNPDF30NNLO	-	-	-	nominal
361106	Z $\to ee$	Powheg+Pythia8	CTEQ6L1	1.00	1901.2	1.026	alternative
361107	Z $\to \mu\mu$	Powheg+Pythia8	CTEQ6L1	1.00	1901.2	1.026	alternative
361108	Z $\to \tau\tau$	Powheg+Pythia8	CTEQ6L1	1.00	1901.2	1.026	alternative
364500-364509	NLO Zγ	Sherpa 2.2.2	NNPDF30NNLO	-	-	-	alternative
361140-361149	LO Zγ	Sherpa 2.2.4	NNPDF30NLO	1.00	-	1.00	nominal
361600	W^+W^-	Powheg+Pythia8	NLO CT10	1.00	10.636	1.00	
361100	$W^+ \to e\nu$	Powheg+Pythia8	CTEQ6L1	1.00	11306.0	1.0172	nominal
361101	$W^+ \to \mu\nu$	Powheg+Pythia8	CTEQ6L1	1.00	11306.0	1.0172	nominal
361102	$W^+ \to \tau\nu$	Powheg+Pythia8	CTEQ6L1	1.00	11306.0	1.0172	nominal
361103	$W^- \to e\nu$	Powheg+Pythia8	CTEQ6L1	1.00	8283.1	1.0357	nominal
361104	$W^- \to \mu\nu$	Powheg+Pythia8	CTEQ6L1	1.00	8283.1	1.0357	nominal
361105	$W^- \to \tau\nu$	Powheg+Pythia8	CTEQ6L1	1.00	8282.9	1.0357	nominal
410470	$t\bar{t}$ $(\geq 1\ell)$	Powheg+Pythia6	A14NNPDF23LO	0.54382	729.77	1.1398	
410155	$t\bar{t}W$	Madgraph+Pythia8	NNPDF23LO	1.00	0.54822	1.096	nominal
410218	$t\bar{t}Z(ee)$	Madgraph+Pythia8	NNPDF23LO	1.00	0.036865	1.12	nominal
410219	$t\bar{t}Z(\mu\mu)$	Madgraph+Pythia8	NNPDF23LO	1.00	0.036868	1.12	nominal
364242	WWW $\to 3\ell 3\nu$	Sherpa 2.2.2	NNPDF30NNLO	1.00	0.0071979	1.00	nominal
364243	WWZ $\to 4\ell 2\nu$	Sherpa 2.2.2	NNPDF30NNLO	1.00	0.0017966	1.00	nominal
364244	WWZ $\to 2\ell 4\nu$	Sherpa 2.2.2	NNPDF30NNLO	1.00	0.0035467	1.00	nominal
364245	WZZ $\to 5\ell 1\nu$	Sherpa 2.2.2	NNPDF30NNLO	1.00	0.0018807	1.00	nominal
364246	WZZ $\to 3\ell 3\nu$	Sherpa 2.2.2	NNPDF30NNLO	0.4463	0.00074436	1.00	nominal
364247	ZZZ $\to 6\ell 0\nu$	Sherpa 2.2.2	NNPDF30NNLO	1.00	0.0001451	1.00	nominal
364248	ZZZ $\to 4\ell 2\nu$	Sherpa 2.2.2	NNPDF30NNLO	0.2245	0.00008652	1.00	nominal
364249	ZZZ $\to 2\ell 4\nu$	Sherpa 2.2.2	NNPDF30NNLO	0.4447	0.00017140	1.00	nominal

are simulated at LO in perturbative QCD (pQCD) for QCD-mediated, interference, and EW processes using MadGraph5_aMC@NLO2.6.7. The parton shower and hadronization processes are modelled using Herwig7.2.1. Diboson QCD $VVjj$ processes are simulated with Sherpa2.2.2, incorporating full electroweak vertex dynamics for up to one additional parton at NLO and up to three at LO, while the electroweak $W^{\pm}Z/\gamma^{*}jj$ and $Z/\gamma^{*}Z/\gamma^{*}jj$ productions are modelled using MadGraph5_aMC@NLO2.6.2 and Sherpa2.2.2, respectively. For the $V\gamma$ processes, Sherpa2.2.11 accounts for off-shell effects. The EW $V\gamma$ production is simulated using MadGraph5_aMC@NLO2.6.5+Pythia8.240. Triboson events leading to jets plus leptons are generated at LO with Sherpa2.2.2. The $t\bar{t}V$ samples are simulated at NLO in pQCD with MadGraph5_aMC@NLO2.3.3.p0, interfaced with Pythia8.210, and normalised to higher-order theoretical predictions. Contributions from tZq are generated at LO using MadGraph5_aMC@NLO2.3.3.p1 with parton showering by Pythia8.212. The W/Z bosons with jets are generated with MadGraph5_aMC@NLO2.3.2.p1 at LO, interfaced with Pythia8.210, and normalised to NNLO cross-sections. For $t\bar{t}$ and single top-quark events, the generator Powheg Boxv2 is employed with Pythia8.230 for subsequent processes and the A14 tune. Top-quark spin correlations are retained, with MadSpin [80]) used for t-channel top quarks. Lastly, prompt photon plus jet production is simulated with Sherpa2.2.2, including up to two jets at NLO and four at LO, capturing the contributions from misidentified converted photons. Elaborate details of these simulations are summarised in Table 5.6.

Table 5.6: Summary of background MC simulation in the same-sign WW channel. The notation V is used to represent either W or Z/γ^* [81].

Process, short description	ME Generator + parton shower	Order	Tune	PDF set in ME
EW, Int, QCD $W^\pm W^\pm jj$, nominal signal	MadGraph5_aMC@NLO2.6.7 + Herwig7.2	LO	Herwig	NNPDF3.0nlo
EW, Int, QCD $W^\pm W^\pm jj$, alternative shower	MadGraph5_aMC@NLO2.6.7 + Pythia8.244	LO	A14	NNPDF3.0nlo
EW $W^\pm W^\pm jj$, NLO pQCD approx.	Sherpa2.2.11 & Sherpa2.2.2(WWW) & Powheg Box2+Pythia8.235 (WH)	+0,1j@LO NLO	Sherpa A14	NNPDF3.0nnlo
EW $W^\pm W^\pm jj$, NLO pQCD approx.	Powheg Boxv2 + Pythia8.230	NLO (VBS approx.)	AZNLO	NNPDF3.0nlo
QCD $W^\pm W^\pm jj$, NLO pQCD approx.	Sherpa2.2.2	+0,1j@LO	Sherpa	NNPDF3.0nnlo
QCD $VVjj$	Sherpa2.2.2	+0,1j@NLO; +2,3j@LO	Sherpa	NNPDF3.0nnlo
EW $W^\pm Z/\gamma^* jj$	MadGraph5_aMC@NLO2.6.2+Pythia8.235	LO	A14	NNPDF3.0nlo
EW $Z/\gamma^* Z/\gamma^* jj$	Sherpa2.2.2	LO	Sherpa	NNPDF3.0nnlo
QCD $V\gamma jj$	Sherpa2.2.11	+0,1j@NLO; +2,3j@LO	A14	NNPDF3.0nnlo
EW $V\gamma jj$	MadGraph5_aMC@NLO2.6.5+Pythia8.240	LO	A14	NNPDF3.0nlo
VVV	Sherpa2.2.1 (leptonic) & Sherpa2.2.2 (one $V \to jj$)	+0,1j@LO	Sherpa	NNPDF3.0nnlo
$t\bar{t}V$	MadGraph5_aMC@NLO2.3.3.p0 + Pythia8.210	NLO	A14	NNPDF3.0nlo
tZq	MadGraph5_aMC@NLO2.3.3.p1 + Pythia8.212	LO	A14	NNPDF2.3lo

Chapter 6

Quark/Gluon Tagging and Calibration

This chapter describes the development of a jet tagging algorithm for jets initiated by light quarks with high transverse momentum ($p_{\mathrm{T}} > 500$ GeV). It represents the first quark/gluon jet tagger utilizing the Multi-Variable Analysis (MVA) method in ATLAS. The performance of this tagger is evaluated and calibrated using real experimental data, in comparison with conventional taggers. This study is specifically designed to enhance the dijet resonance search [82] by incorporating quark/gluon tagging to improve sensitivity.

The chapter is organized as follows: the motivation for quark/gluon discrimination and calibration is discussed in Section 6.1. Section 6.2 outlines the specialized event selection used in this study. The definitions of quark- and gluon-enriched samples are provided in Section 6.3. The development of the taggers is detailed in Section 6.4. The method for separating quark/gluon samples and determining scale factors is described in Section 6.5 and Section 6.6, respectively. Systematic uncertainties are discussed in Section 6.7, and the results are presented in Section 6.8. Finally, Section 6.9 summarizes the main contributions and provides an outlook.

6.1 Motivation

The identification of jets initiated by quarks or gluons is crucial for many analyses conducted at the ATLAS experiment at the LHC, particularly those involving SM measurements or searches for new physics. Improving the ability to distinguish between quark- and gluon-initiated jets can enhance the sensitivity and precision of these studies.

This distinction has a wide range of applications. For example, electroweak processes often produce two quark-initiated jets associated with vector boson or Higgs production [83, 84]. Moreover, various new physics scenarios predict heavy particles decaying into quark-initiated jets [85, 86]. In supersymmetric (SUSY) models, gluinos can decay into quark-initiated jets and neutralinos [87], while in R-parity violating SUSY models, neutralinos may further decay into additional quark-initiated jets [88]. Tagging gluon-initiated jets is also valuable in specific contexts, such as searches for resonances decaying into a b-quark and a gluon [82] or studies of stealth SUSY models [89]. Furthermore, differences in jet calibration for quark- and gluon-initiated jets can be addressed using a quark/gluon (q/g) tagging tagger, improving calibration accuracy [90].

From a theoretical perspective, as discussed in Section 2.1.2, the distinct properties of quark and gluon jets arise from their differing color charges. According to QCD, gluons have a larger color charge compared to quarks by a factor of 9/4, known as the "Casimir ratio". This results in gluons emitting more particles during hadronization, leading to higher track multiplicity and broader jet widths compared to quarks. These characteristics are utilized to differentiate quark- and gluon-initiated jets by examining features such as charged track multiplicity and jet width.

Calibration is an essential step to ensure the accuracy of tagging efficiencies. Ideally, the efficiencies obtained from MC simulations would perfectly match those in real experimental data. However, in practice, discrepancies inevitably arise due to limitations in simulation accuracy and detector modeling. These differences must be quantified and corrected to maintain the reliability of the analysis. To address this, the tagging efficiencies (ϵ) are evaluated both in MC simulations and real data. The calibration process adjusts the MC-based efficiencies to better reflect the experimental reality, thereby improving the robustness of the results.

This study aims to assess the performance of two tagging methods for distinguishing quark- and gluon-initiated jets: the charged-particle constituent multiplicity (N_{trk}) tagger and a BDT tagger. The tagging efficiencies are evaluated using datasets with varying quark and gluon fractions, and the results are used to calibrate tagging efficiencies for MC simulated jets.

6.2 Event Selection

6.2.1 Event Cleaning

Event cleaning is performed to ensure data quality and remove corrupted events. In addition to requiring events to belong to the luminosity blocks specified in the GRL, the following criteria are applied:

- LAr noise bursts (`xAOD::EventInfo::LAr`),
- Tile calorimeter corruption, e.g. power supply trips (`xAOD::EventInfo::Tile`),
- Single SCT upsets (`xAOD::EventInfo::SCT`),
- Incomplete events due to TTC restarts, removed using `xAOD::EventInfo::Core`.

Additionally, events must contain a primary vertex with at least two associated tracks. The primary vertex is defined as the one with the largest $\sum p_{\mathrm{T}}^2$.

6.2.2 Kinematic selection

The p_{T} of the jet is required to exceed 500 GeV to enhance the fraction of quark jets and improve the resolution of jet constituents. Only the leading two jets, defined as the jets with the highest p_{T}, are considered. These jets are treated as dijet events and must satisfy the pseudorapidity requirement $|\eta| < 2.5$, ensuring that their charged constituents are contained within the coverage of the ID.

To maintain balance in p_{T} and reduce contamination from non-isolated jets, the p_{T} ratio of the leading jet to the sub-leading jet is constrained to be less than 1.5. These two leading-p_{T} jets form the basis for the construction of quark-enriched and gluon-enriched subsamples. All event selections used are summarized in Table. 6.1.

Figure 6.1 presents the transverse momentum (p_{T}) distributions of the leading and sub-leading jets in dijet events, shown for both Monte Carlo simulation and data. The distributions exhibit the expected logarithmic fall-off, reflecting the behavior of the parton distribution functions.

Table 6.1: The selections to retrieve quark/gluon-enriched samples. j_i represents the i-th jet in p_{T}-ordering.

Selection	Multi-jet sample
Trigger	HLT_j420
Number of jets	≥ 2
$p_{\mathrm{T}}(j_1)$	> 500
$p_{\mathrm{T}}(j_2)$	> 500
$p_{\mathrm{T}}(j_1)/p_{\mathrm{T}}(j_2)$	< 1.5
$\lvert\eta(j_1)\rvert$	< 2.1
$\lvert\eta(j_2)\rvert$	< 2.1
Target parton	Quark(Higher $\lvert\eta\rvert$) or Gluon (Lower $\lvert\eta\rvert$)

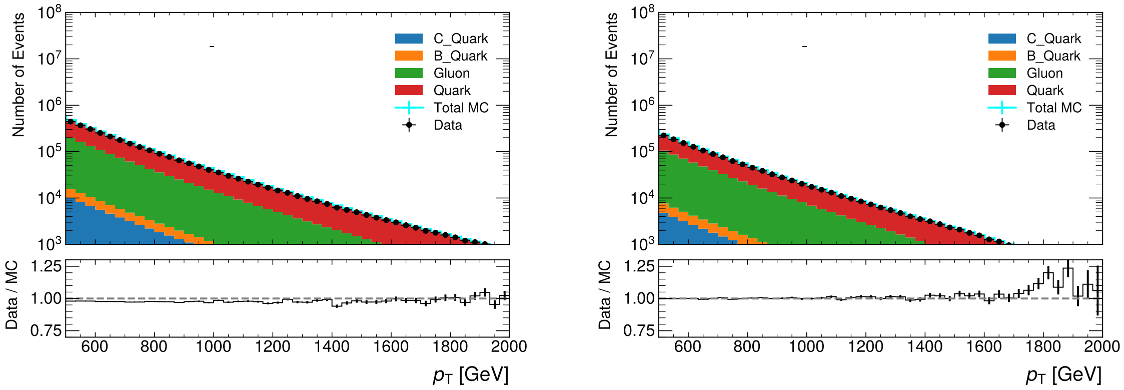

(a) Leading jet (Pythia)

(b) Subleading jet (Pythia)

Figure 6.1: Transverse momentum distributions of the leading and subleading jets in dijet events, as simulated with Pythia.

6.3 Definition of Quark- and Gluon-Enriched Jet Samples

To study quark and gluon jet properties, two distinct jet samples are defined based on the pseudorapidity ($|\eta|$) of the leading jets in dijet events. The quark-enriched sample is selected using the jet with the larger $|\eta|$ among the two leading jets, while the gluon-enriched sample is defined by the jet with the smaller $|\eta|$. This selection exploits the structure of the proton, where valence quark contributions dominate at higher momentum fractions, making forward jets (larger $|\eta|$) more likely to originate from quarks. In contrast, jets produced in the central region (smaller $|\eta|$) are more likely to be initiated by gluons due to the larger gluon density at lower momentum fractions.

6.4 Quark/Gluon Tagger Construction

6.4.1 Jet Tagging Variables

In this calibration, the number of tracks (N_{trk}), jet width (W_{trk}), and the two-point energy correlation function ($C_1^{\beta=0.2}$) computed from the associated tracks are used as q/g tagging variables.

N_{trk} The number of tracks associated with the jet.

W_{trk} The p_{T}-weighted width of the jet, divided by the scalar sum of the transverse momenta of the associated tracks. It is defined as

$$W_{\text{trk}} = \frac{\sum_{\text{trk}\in\text{jet}} p_{\text{T,trk}} \Delta R_{\text{trk,jet}}}{\sum_{\text{trk}\in\text{jet}} p_{\text{T,trk}}}, \tag{6.1}$$

where $p_{\text{T,trk}}$ is the transverse momentum of a charged track reconstructed by the inner detector (ID), and $\Delta R_{\text{trk,jet}}$ is the distance in the η-ϕ plane between the track and the jet axis.

$C_1^{\beta=0.2}$ The two-point energy correlation function is defined as

$$C_1^{\beta=0.2} = \frac{\sum_{i,j\in\text{jet}}^{i\neq j} p_{\text{T},i} p_{\text{T},j} \left(\Delta R_{i,j}\right)^{\beta=0.2}}{\left(\sum_{\text{trk}\in\text{jet}} p_{\text{T,trk}}\right)^2}, \tag{6.2}$$

where i and j denote tracks associated with the jet, and the sum runs over all pairs of tracks. The parameter β is fixed to 0.2, which is found to be suitable for quark/gluon tagging.

6.4.2 Boosted Decision Tree Tagger

MVA techniques are commonly used to separate signal from background in high-energy physics. One effective method under this category is the Boosted Decision Tree (BDT). A BDT uses a tree structure to classify events by applying a sequence of binary decisions based on input variables. At each node, a split is made depending on the value of a selected feature. This process continues until certain stopping conditions are met, such as a maximum tree depth or a minimum number of events per node. Once trained, the BDT assigns a score to each event, which reflects how likely it is to belong to a certain class. In this analysis, a BDT tagger is trained using `LightGBM`, with additional improvements from hyperparameter tuning and cross-validation. The tagger is used to classify jets as quark- or gluon-like. Details of the variable selection, training strategy, and optimization are described in the following sections.

Feature selections

The input variables to the BDT are selected based on their ability to separate quark and gluon jets. Figure 6.2 shows the distributions of key variables and the BDT score in forward and central detector regions, while Figure 6.3 compares quark and gluon jet features in different p_{T} ranges.

A correlation matrix is used to examine the relationships among the input features and identify redundant variables. As shown in Figure 6.4, N_{trk}, W_{trk}, and $C_1^{\beta=0.2}$ are moderately correlated, while p_{T} and η are less correlated with other variables.

Regarding p_{T}, although training separate models for each p_{T} range is possible, it adds complexity. Instead, a single BDT is trained using events from all p_{T} ranges, allowing it to generalize over the spectrum.

The inclusion of $|\eta|$ is also studied. Ideally, the tagger should perform consistently across detector regions. To test this, two training setups are compared—one including $|\eta|$ and one without. Figure 6.5 shows that excluding $|\eta|$ introduces a dependence on detector geometry. Including $|\eta|$ helps to reduce this dependence and improve tagger stability.

Training weights

Since high-p_{T} jets are less frequent in the simulation, a weight correction is applied to flatten the p_{T} distribution during training. These “flat-p_{T} ” weights are used only during training to ensure balanced learning across p_{T} ranges. The weights are derived by inverting the bin contents of the p_{T} histogram, as shown in Figure 6.6. For validation and calibration steps, the original physics-based weights are used.

Training Configurations

The BDT is implemented using the `LightGBM` framework [91], a fast and scalable gradient boosting library. The model is trained on multi-jet MC samples with truth-labeled quark

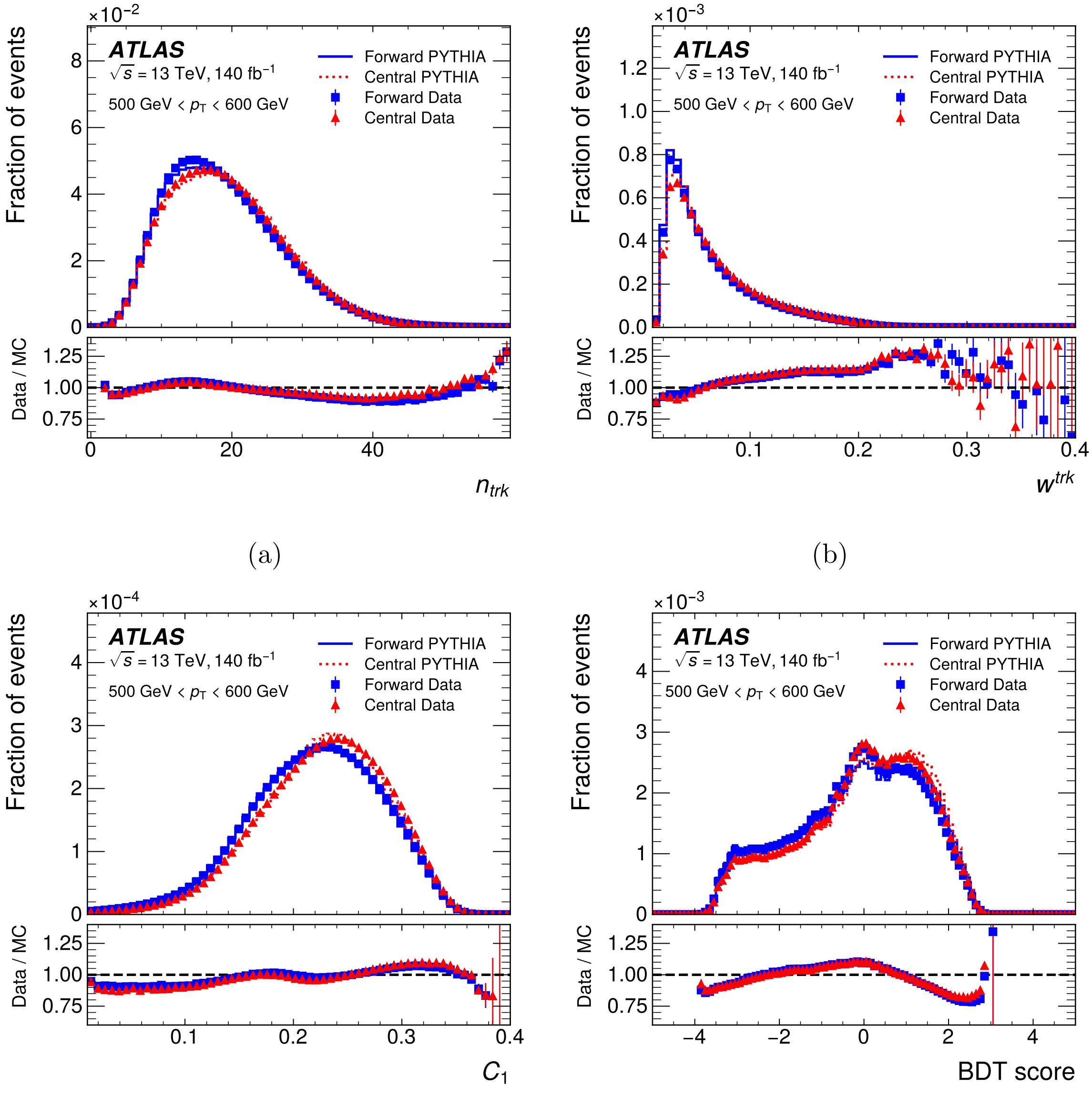

(a)

(b)

(c)

(d)

Figure 6.2: The distributions of N_{trk} a, W_{trk} b, C_1 c, and the BDT score d in the forward and central regions in data (closed symbols) and the Pythia MC (lines) are shown in the upper panels. The lower panels present the ratio of data to MC. The distributions correspond to jets with p_{T} in the range of 500–600 GeV. Vertical error bars indicate statistical uncertainties [65].

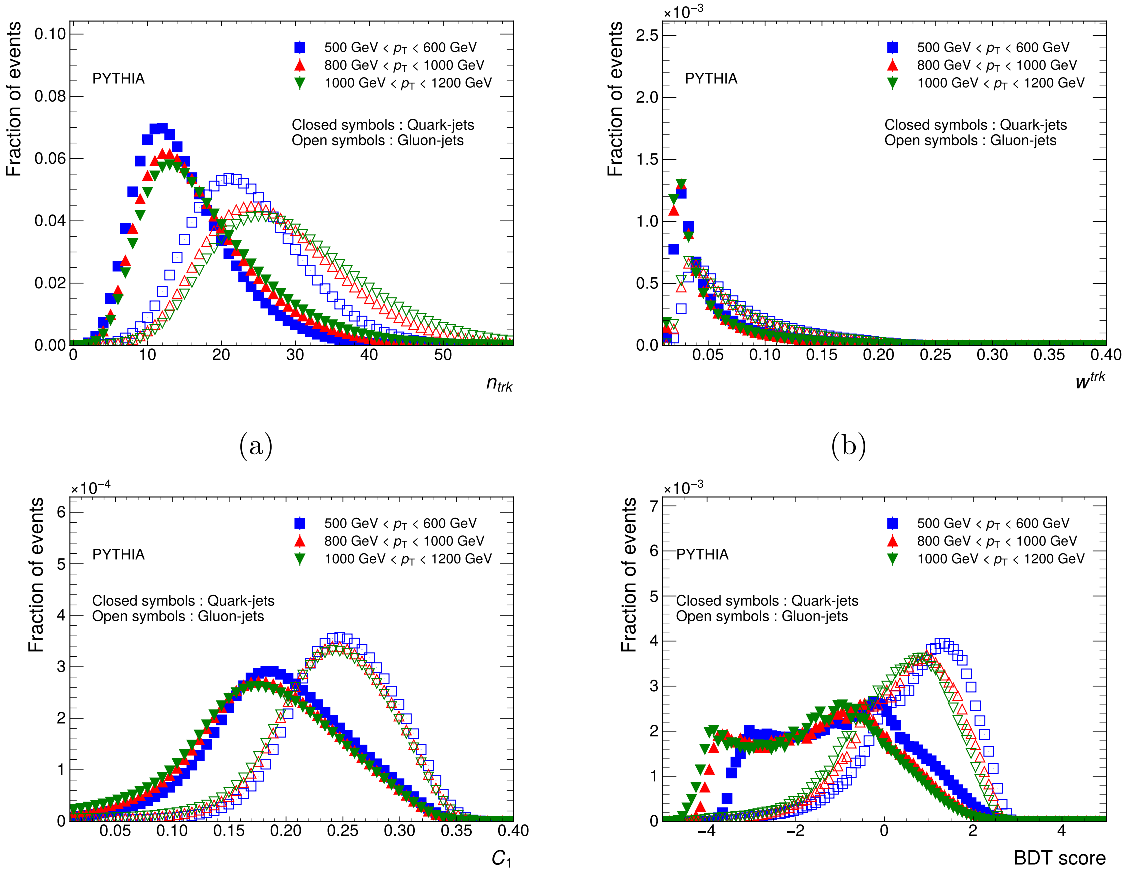

(a)

(b)

(c)

(d)

Figure 6.3: The distributions of N_{trk} a, W_{trk} b, C_1 c, and the BDT score d for quark-jets (closed symbols) and gluon-jets (open symbols) in specific p_{T} regions using the PYTHIA MC samples.

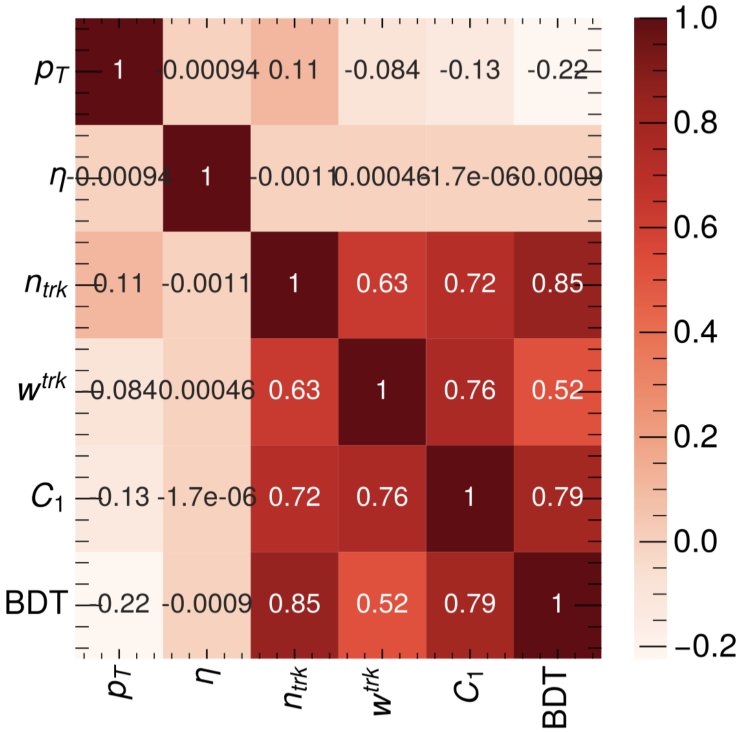

Figure 6.4: Correlation matrix of jet variables and the BDT scores.

and gluon jets.

To avoid overfitting, five-fold cross-validation is performed. The hyperparameters of the model are optimized using the `Optuna` package [92], which explores different combinations of parameters to improve performance.

Approximately 30% of the events from each data-taking period in the PYTHIA8 MC datasets A, D, and E are randomly selected for model development, yielding a total of about 60 million jets. The selected sample is subsequently divided into three subsets: 80% for training, 10% for validation, and 10% for testing.

The final hyperparameter values selected after 100 optimization iterations are:

- `bagging_fraction`: 0.9176
- `bagging_freq`: 2
- `feature_fraction`: 0.9085
- `lambda_l1`: 0.00164
- `lambda_l2`: 0.00633

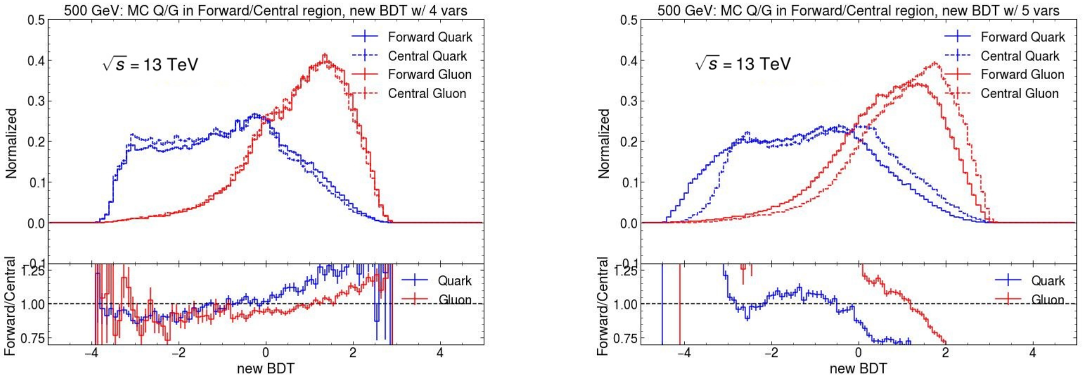

(a) Scenario 1: Training without $|\eta|$

(b) Scenario 2: Training with $|\eta|$

Figure 6.5: Comparison of BDT score distributions for different training scenarios in the jet p_T range of 500-600 GeV. (a) BDT trained without $|\eta|$; (b) BDT trained with $|\eta|$.

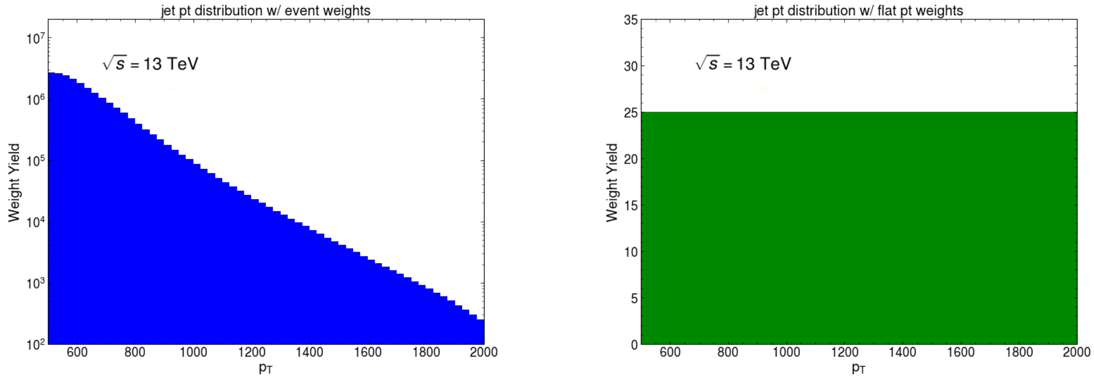

(a) Leading jet (Pythia)

(b) Subleading jet (Pythia)

Figure 6.6: The p_T distributions of jets using physical weights and "flat-p_T " weights. (a) Leading jet, (b) subleading jet, both obtained from Pythia simulations.

- `min_child_samples`: 13
- `num_leaves`: 224

These optimized settings help the BDT tagger achieve good classification performance and generalize well to different datasets.

Performance

The performance of the BDT tagger is evaluated using two primary metrics: the overtraining check and the Receiver Operating Characteristic (ROC) curve analysis.

The ROC curve offers a graphical summary of a classifier's performance across varying decision thresholds. It is constructed by plotting the True Positive Rate (TPR), also known as recall or sensitivity, against the False Positive Rate (FPR), sometimes referred to as the false alarm rate. This visualization provides insight into the model's ability to distinguish between quark and gluon jets.

In binary classification, each prediction falls into one of four categories:

- **True Positive (TP):** The model correctly predicts a positive class.
- **False Positive (FP):** The model incorrectly predicts a positive class.
- **True Negative (TN):** The model correctly predicts a negative class.
- **False Negative (FN):** The model incorrectly predicts a negative class.

The performance metrics are defined as:

$$\mathrm{TPR} = \frac{\mathrm{TP}}{\mathrm{TP} + \mathrm{FN}}, \quad \mathrm{FPR} = \frac{\mathrm{FP}}{\mathrm{FP} + \mathrm{TN}}.$$

By scanning over different thresholds, the ROC curve captures the trade-off between sensitivity and specificity. A high-performing model is characterized by a ROC curve that approaches the top-left corner of the plot, corresponding to high TPR and low FPR.

Figure 6.7 presents the ROC curves for several individual jet observables, along with the BDT tagger, evaluated in the jet p_{T} range between 500 and 600 GeV. Results are shown separately for the forward and central regions. In the training configuration, gluon jets are defined as the signal class, and quark jets as background. As a result, the ROC curves are plotted with quark-jet efficiency on the x-axis and gluon-jet rejection (1 - gluon efficiency) on the y-axis. Under this convention, optimal classifier performance is indicated by curves that extend toward the top-right corner of the plot.

Extending the evaluation across all p_{T} ranges, Figure 6.8 presents the Area Under the Curve (AUC) for the N_{trk}-only tagger and the BDT tagger as a function of jet transverse momentum.

Among the individual input variables, the N_{trk}-only tagger provides the strongest discrimination power for quark/gluon tagging. Variables such as W_{trk} and $C_1^{\beta=0.2}$, which are defined as ratios, are less sensitive to track reconstruction inefficiencies. The BDT tagger, which combines N_{trk}, W_{trk}, $C_1^{\beta=0.2}$, and additional input variables, consistently achieves

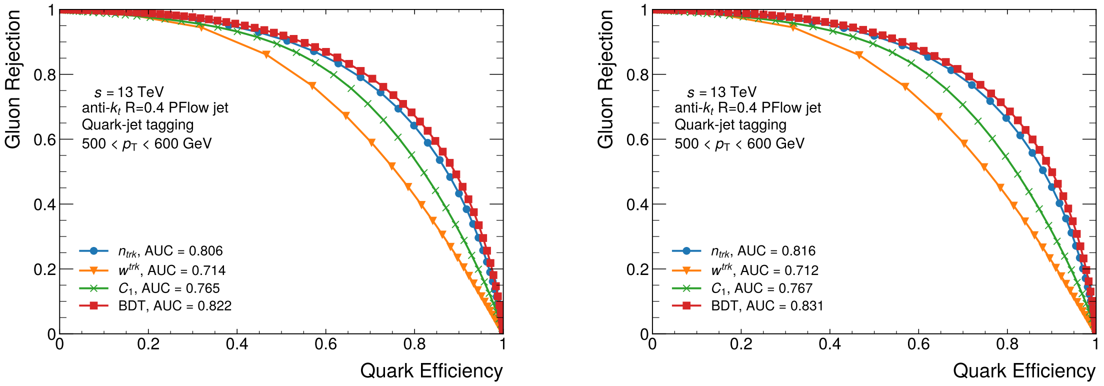

(a) Forward region (b) Central region

Figure 6.7: ROC curves for different taggers in the jet p_T range between 500 and 600 GeV in the (a) forward and (b) central regions.

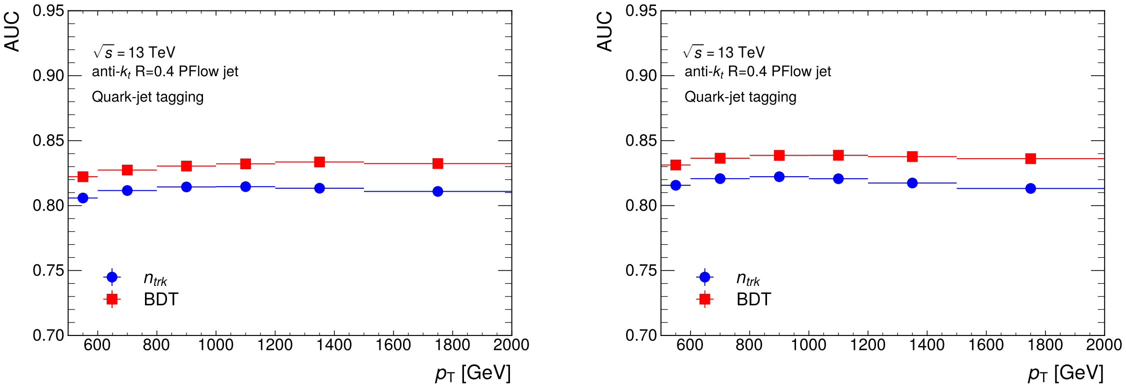

(a) Forward region (b) Central region

Figure 6.8: AUC values for different taggers as a function of jet p_T, shown separately for the (a) forward and (b) central regions.

higher AUC values than the N_{trk}-only tagger across all jet p_T intervals. This indicates that the multivariate approach improves gluon rejection while preserving quark identification efficiency.

Both the N_{trk}-only and BDT taggers are subject to calibration procedures, which are described in detail in the following section.

6.5 Matrix Method

The matrix method is used to extract pure quark or gluon jets from quark-enriched and gluon-enriched samples, assuming that the variable distributions are the same for quark and gluon jets in both samples.

The relationship between the higher and lower $|\eta|$ jet distributions is expressed as:

$$\begin{pmatrix} p_{\mathrm{H}}(x) \\ p_{\mathrm{L}}(x) \end{pmatrix} = \underbrace{\begin{pmatrix} f_{\mathrm{H,Q}} & f_{\mathrm{H,G}} \\ f_{\mathrm{L,Q}} & f_{\mathrm{L,G}} \end{pmatrix}}_{\equiv F} \begin{pmatrix} p_{\mathrm{Q}}(x) \\ p_{\mathrm{G}}(x) \end{pmatrix} \tag{6.3}$$

$$\Leftrightarrow \begin{pmatrix} p_{\mathrm{Q}}(x) \\ p_{\mathrm{G}}(x) \end{pmatrix} = F^{-1} \begin{pmatrix} p_{\mathrm{H}}(x) \\ p_{\mathrm{L}}(x) \end{pmatrix}, \tag{6.4}$$

where $p_{\mathrm{Q,G}}(x)$ represent the distributions of the q/g tagging variable x in pure quark- and gluon-jet samples, $p_{\mathrm{H}}(x)$ and $p_{\mathrm{L}}(x)$ are the distributions in the multi-jet, higher $|\eta|$ jet, and lower $|\eta|$ jet samples, respectively, and $f_{\mathrm{H/L,Q/G}}$ are the fractions of quarks or gluons in the higher $|\eta|$ or lower $|\eta|$ jet samples.

6.6 Scale Factors

The working points (WPs) of the quark/gluon taggers are defined by fixing the quark-jet tagging efficiency in the nominal Pythia MC sample. For each tagger, the quark- and gluon-jet efficiencies at a given threshold x^{WP} are defined as:

$$\epsilon_{\mathrm{Q/G}}(x^{\mathrm{WP}}) = \int_{x<x^{\mathrm{WP}}} p_{\mathrm{Q/G}}(x)\,\mathrm{d}x, \tag{6.5}$$

where $p_{\mathrm{Q/G}}(x)$ denotes the probability density function of the tagger score for quark or gluon jets.

The corresponding rejection factors are given by:

$$\xi_{\mathrm{Q/G}}(x^{\mathrm{WP}}) = \frac{1}{1-\epsilon_{\mathrm{Q/G}}(x^{\mathrm{WP}})}. \tag{6.6}$$

To account for potential differences between data and simulation, data-to-MC scale factors (Scale Factor (SF)s) are derived for each tagger at fixed WPs, in bins of jet p_{T}. These scale factors correct either the quark-jet efficiency or the gluon-jet rejection to match observations in data.

The scale factors are defined as follows:

$$\mathrm{SF}_{\mathrm{Q}}(x^{\mathrm{WP}}) = \frac{\epsilon_{\mathrm{Q}}^{\mathrm{Data}}(x^{\mathrm{WP}})}{\epsilon_{\mathrm{Q}}^{\mathrm{MC}}(x^{\mathrm{WP}})} \tag{6.7}$$

$$\mathrm{SF}_{\mathrm{G}}(x^{\mathrm{WP}}) = \frac{\xi_{\mathrm{G}}^{\mathrm{Data}}(x^{\mathrm{WP}})}{\xi_{\mathrm{G}}^{\mathrm{MC}}(x^{\mathrm{WP}})}, \tag{6.8}$$

where ϵ_{Q} and ξ_{G} are the quark efficiency and gluon rejection, respectively, measured in data and simulation.

Working points corresponding to 50%, 60%, 70%, and 80% fixed quark-jet efficiencies have been studied. The resulting scale factors for each WP show consistent trends and exhibit similar behaviors across different jet p_{T} ranges.

6.7 Systematic Uncertainties

6.7.1 Theoretical Uncertainties

- **Parton Shower Modeling:** Variations in parton shower algorithms can affect the extracted SFs. This uncertainty is assessed by comparing results from two MC samples that share the same matrix element and hadronization settings but use different parton shower models: HERWIG angular-ordered and dipole-based showers. The difference is found to be less than 10% for quark efficiency and up to 20% for gluon rejection, making it the dominant uncertainty for gluon SFss.

- **PDF Variations:** The uncertainty from parton distribution functions is evaluated using the LHAPDF package with the NNPDF2.3 set. By reweighting events with each variation in the set and comparing the resulting SFs, an uncertainty of 5% to 7% is obtained. This contribution is relatively small compared to other sources.

- **Scale Variations:** Renormalization (μ_R) and factorization (μ_F) scale uncertainties are used to estimate missing higher-order QCD effects. Using the nominal PYTHIA sample, seven scale variations are applied:

$$(\mu_R, \mu_F) = (2, 2), (2, 1), (1, 1), (1, 2), (1, 0.5), (0.5, 1), (0.5, 0.5).$$

The largest deviation from the nominal result across these variations is taken as the systematic uncertainty, ranging between 4% and 7%.

- **Splitting-Kernel Variations:** Different choices of non-singular terms in the splitting functions can influence the modeling of QCD radiation. This variation results in uncertainties below 1%.
- **Matrix Element Modeling:** Differences in the hard scattering process are probed by comparing SFs obtained from samples generated with different matrix element generators, specifically Powheg and Pythia. This reflects theoretical uncertainty in the modeling of parton-level dynamics.

6.7.2 Experimental Uncertainties

- **Tracking Efficiency:** Tracking-related uncertainties arise from imperfections in track reconstruction, including material interactions and fake rate mismodeling. Corrections applied to associated tracks result in a systematic uncertainty ranging from 1% to 8%.
- **JES and JER:** Uncertainties in jet energy calibration and resolution are evaluated by applying standard JES and JER systematic variations. The resulting impact on SFs is small, approximately 0.2%.
- **Track Multiplicity and BDT Reweighting:** To correct for residual η-dependent mismodeling in the quark- and gluon-enriched regions, reweighting based on $N_{\text{trk}}$and BDT scores is applied. The associated systematic uncertainty is minor, between 0.1% and 0.5%.
- **MC Non-closure:** Discrepancies between truth-labeled and reweighted distributions in simulation are used to estimate the non-closure uncertainty. This source contributes an uncertainty of approximately 1%.

- **Hadronization Modeling:** The uncertainty related to hadronization is evaluated using Sherpa samples with both string- and cluster-based models. The resulting uncertainty on SFs spans 1% to 8% for both jet types.

6.7.3 Statistical Uncertainties

Statistical uncertainties are evaluated by fluctuating the bin contents of the input data and MC distributions using Poisson or Gaussian variations, depending on the sample size. For each variation, the full scale factor extraction procedure is repeated. The standard deviation of the resulting scale factors over 5000 pseudo-experiments is taken as the statistical uncertainty. This contribution is found to be approximately 0.1%.

6.8 Results

Figure 6.9 presents the scale factors for both quark and gluon jets at the 50% quark-jet efficiency working point, as a function of jet transverse momentum. The scale factors range from 0.92 to 1.02, with a total systematic uncertainty of approximately 20%. The dominant source of uncertainty arises from theoretical modeling.

To test the robustness of the results, the measurements were repeated after reweighting the jet $|\eta|$ distribution in the quark- and gluon-enriched samples to be flat. The resulting scale factors are consistent with the nominal results within the quoted total uncertainties, indicating stability with respect to $|\eta|$ dependence.

6.9 Summary and Outlook

This work presented the development of a BDT tagger for quark/gluon jet identification and the calibration of the quark/gluon tagging algorithm. Multi-jet events and alternative MC samples were utilized to estimate systematic uncertainties and ensure the robustness of the approach.

The methodologies developed in this study have been served as benchmark for further advancements in the field of quark/gluon jet tagging. For example,“Constituent-Based Quark-Gluon Tagging using Transformers with the ATLAS detector” [93] builds on this foundation

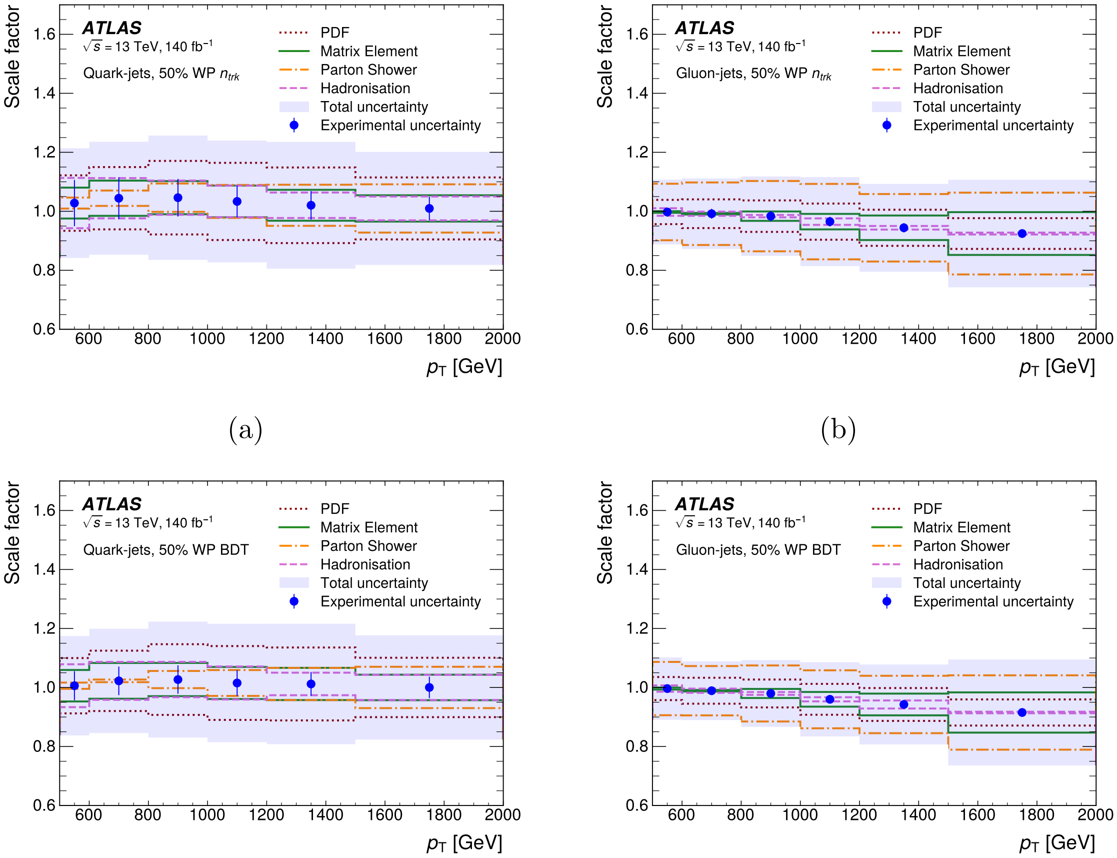

(a) (b)

(c) (d)

Figure 6.9: Scale factors (points) defined in Eq. (6.8) along with total uncertainties (shaded bands), leading theoretical uncertainties (solid lines), and experimental uncertainties (vertical error bars), for the N_{trk}-only tagger (a,b) and BDT tagger (c,d), shown as functions of jet p_{T}. Results are presented separately for quark jets (left) and gluon jets (right), using the Pythia MC sample [65].

by applying modern deep learning techniques directly to jet constituents. While our approach focuses on high-level jet variables, this work explores innovative architectures such as Particle Flow Networks, Energy Flow Networks, ParticleNet, and particle transformers. Additionally, Dynamically Enhanced Particle Transformers have been investigated to further improve tagging performance.

Looking ahead, a promising direction for quark/gluon tagging lies in its extension to the HL-LHC era. With the expanded pseudorapidity coverage of the ITk and the inclusion of the High Granularity Timing Detector, which provides additional timing information in the forward region ($2.4 < |\eta| < 4.0$), track reconstruction tasks are expected to improve significantly. I actively contributed to early discussions with the principal developers of this project, exploring the potential of these novel capabilities.

These advancements underscore the importance of combining high-level features with state-of-the-art machine learning techniques to address the challenges of jet tagging. This work lays the foundation for future improvements in tagging precision and efficiency, particularly as we prepare for the demanding conditions of the HL-LHC.

Chapter 7

Charged Higgs

In this chapter, a combination of two individual searches for singly- and doubly-charged Higgs bosons produced via VBF is presented. These searches, performed separately during Run 2, serve as inputs to the combined analysis. The combination is carried out by merging histograms from both analyses into a common workspace within a unified fitting framework, allowing constraints to be placed on the `H5plane` benchmark of the GM model.

The chapter is organized as follows: Section 7.1 describes the event selection criteria and the orthogonal analyses from both individual searches, which form the foundation of the combination. Section 7.2 addresses the treatment of systematic uncertainties. The statistical method, which connects observed event counts to physical cross sections, is explained in Section 7.3. Finally, Section 7.4 presents the results, discusses prospects for future searches, and includes a summary of my contributions.

7.1 Event Selection

This section outlines the event selection criteria for two analyses entering the combination and explores their orthogonality. Event selection is a balance between maximizing signal efficiency and minimizing background contamination. The optimization of selection criteria is an iterative process, requiring detailed understanding of both the signal and background processes. Effective event selection is crucial for the success of HEP experiments, enabling the discovery of new particles and the precise measurement of fundamental physics parameters.

Section 7.1.1 details the common selection criteria applied across both analyses, while

Section 7.1.2 and Section 7.1.3 focus on the specific criteria unique to the WZ and same-sign WW analyses, respectively. A thorough discussion on the orthogonality of the events is presented in Section 7.1.4.

7.1.1 Common Selections in Two Analyses

Both analyses first apply general procedures, then implement stringent selection cuts to delineate signal and control regions subsequent to the baseline selection. Besides the common event cleaning selection described in Section 6.2.1, some additional selections are below.

- **Primary Vertex.** Due to the presence of multiple pp collisions in a single bunch crossing, each event can have multiple vertices reconstructed. The primary vertex used in the analysis is selected to be the vertex with the largest p_{T}^2 sum in the event. Only events where the primary vertex has at least two (three) associated tracks are considered in WZ (same-sign WW) events.
- **Jet Cleaning.** Events containing jets originating from non-collision background processes are vetoed. For this, a loose working point (DFCommonJets_eventClean_LooseBad) of a dedicated event jet cleaning algorithm is used.

Given that both analyses target the VBF signature, characteristics of jets such as high invariant mass and extensive angular separation are employed to enhance the event purity. This is crucial for segregating signal events from QCD-induced processes which yield identical final states, in addition to leptonic information.

7.1.2 WZ Analysis

The WZ analysis selection involves multiple stages of event selection criteria to ensure the purity of the signal and to define the signal regions (SRs) and control regions (CRs). The analysis leverages an Artificial Neural Network (ANN) for event selection within the $H^{\pm}$ context. The ANN is trained to distinguish between signal and background events using several variables that are critical to the identification of VBF events. The selection procedure follows the methodology outlined in the Internal Note from the Run 2 WZ analysis [79].

Baseline Selection

The baseline selection is applied to all data and simulated samples before defining more specific analysis regions. The criteria include:

- **Exactly Three Leptons:** Events must contain exactly three leptons meeting the *Loose* selection criteria, ensuring a clear WZ signature.
- **ZZ Veto:** Events with four or more leptons meeting the *Baseline* criteria are vetoed to reduce the ZZ background.
- **Trigger-Matched Lepton:** At least one of the three leptons must be trigger-matched and have $p_{\mathrm{T}} > 27$ GeV to ensure good trigger efficiency.
- **Z Candidate:** The event must contain a pair of leptons of the same flavor and opposite charge with an invariant mass within 20 GeV of the Z boson mass.
- **W Candidate:** The third lepton, not used in the Z candidate, is considered the W candidate and must satisfy the *Tight* selection criteria.
- **Missing Transverse Energy:** The event must have $E_{\mathrm{T}}^{\mathrm{miss}} > 25$ GeV to account for the neutrino from the W decay.

Signal Region: Artificial Neural Network VBF Selection

The VBF production mode ($pp \to H_5^{\pm}jj \to WZjj$) is characterized by a distinctive detector signature, including the presence of two jets with a large rapidity gap, reduced hadronic activity in the central region, and specific kinematic properties of the jets. To improve the sensitivity of the analysis, machine learning algorithms, specifically an ANN, are employed to classify events as signal-like or background-like.

The ANN used in this analysis is a binary classifier designed to distinguish VBF signal events from background events. The training phase involves a subset of the inclusive phase space, requiring events to pass an inclusive selection with at least two VBF jets having an invariant mass $m_{jj} > 100$ GeV and a 1-jet veto.

The training is conducted using the Keras package [94], a high-level neural network interface running on top of the TensorFlow package [95]. The rectified linear unit (ReLU) is used as the activation function for its efficiency in gradient-based optimization methods. The output activation function is a sigmoid, producing values between 0 and 1.

To maximize the use of available statistics, an n-fold cross-validation technique is applied. Events are divided into n-folds, with $(n-1)$ folds used for training and the remaining fold for testing and evaluation. Regularization techniques, such as Dropout and early stopping, are employed to prevent overfitting. Dropout involves randomly dropping units from the neural network during training to create a bagging-like effect, while early stopping halts training when validation loss stops improving, as determined by a patience parameter.

The selection of the ANN score threshold is optimized to maximize the significance for the lowest mass point (200 GeV for the GM model). A single cut on the ANN output score defines the signal region, simplifying the training process and improving the robustness of the analysis.

ANN VBF Selection: Technical Aspects

The ANN architecture includes two hidden layers with 45 neurons each. The training uses the stochastic gradient descent optimizer with Nesterov's Accelerated Gradient for improved convergence. The learning rate and other hyperparameters are tuned to achieve optimal performance.

The variables used in the ANN training are listed in Table 7.1. These variables are chosen based on their ability to discriminate between signal and background, and their low correlation with each other to ensure diverse information is utilized in the training process.

Table 7.1: Variables used for ANN training in the WZ analysis [79].

Training variable	Definition
m_{jj}	Invariant mass of the two leading-p_{T} jets
$\Delta\phi_{jj}$	Difference in ϕ of the two leading-p_{T} jets
η_W, η_Z	Pseudorapidities of the reconstructed gauge bosons
η_{j_1}	Leading-p_{T} jet pseudorapidity
ζ_{Lep}	Event centrality
$E_{\mathrm{T}}^{\mathrm{miss}}$	Missing transverse momentum
H_{T}	Scalar p_{T} sum of the VBF jets[1] and the leptons from the WZ decay

---

[1] The definition for "VBF jets" is provided in Section 4.3.

ANN VBF Selection: Optimization

The ANN is trained using all $H_5^\pm$ GM simulated events as the signal and SM WZ-EW and WZ-QCD events as background. The individual signal samples are combined after applying cross-section weights for training. This approach is advantageous as it reduces the training effort and allows for a single signal region to be defined.

After training, the ANN signal region is defined by a cut on the ANN output score, chosen to maximize the significance at the lowest mass point. This method has been validated to perform effectively, as studies have shown that training separate mass regions does not significantly improve the analysis.

The efficiency and acceptance of the ANN-based VBF selection are shown in Figure 7.1. The acceptance times efficiency ($\mathcal{A} \times \epsilon$) is evaluated as a function of the mass of the VBF $H_5^\pm$, relative to the generated signal events. For $H_5^\pm$ bosons, the $\mathcal{A} \times \epsilon$ value ranges from 2-12% and 2-5%, respectively, for resonance masses between 200 and 1000 GeV. The differences are due to generator-level selection and different angular distributions of the final products.

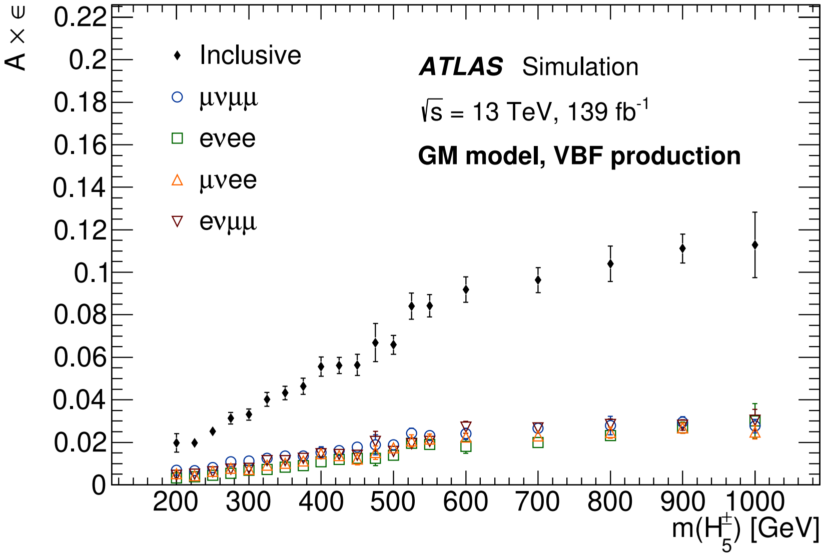

Figure 7.1: The acceptance (A) times efficiency (ϵ) of VBF $H_5^\pm$ selection after the ANN-based VBF selection at different mass points for the individual channels $\mu\nu\mu\mu$, $e\nu ee$, $\mu\nu ee$, $e\nu\mu\mu$, and the sum of all channels. The uncertainty includes both the statistical and experimental systematic components [79].

Control Regions

Two control regions are defined to constrain the dominant backgrounds:

- $W^{\pm}Z - \mathrm{QCD}$ **Control Region:** Populated with events having ANN scores less than 0.82. This region helps constrain the QCD-mediated production of WZ dibosons.
- ZZ **Control Region:** Defined to extract the ZZ background normalization. It is enriched with ZZ events, which represent a significant background.

The detailed selection criteria for the signal and control regions are summarized in Table 7.2.

Table 7.2: Summary of the event selection for the signal and control regions in the WZ analysis [79].

WZ analysis			
Regions Requirement	SR	$W^{\pm}Z - \mathrm{QCD}$ CR	ZZ CR
Leading trigger-matched lepton	> 27 GeV		
3 Loose leptons p_{T}	> 25 GeV		
Electron $\lvert\eta\rvert$	< 2.47, excluding $1.37 \leq \lvert\eta\rvert \leq 1.52$		
Muon $\lvert\eta\rvert$	< 2.7		
Jet p_{T}	> 30 GeV		
Jet $\lvert\eta\rvert$	< 4.5		
Number of VBF jets	≥ 2		
Z candidate	$\lvert m_{ee} - m_Z\rvert < 20$ GeV		
ZZ veto	veto events with ≥ 4 leptons		-
$E_{\mathrm{T}}^{\mathrm{miss}}$	> 25 GeV		-
b-jet veto	$N_{b-\mathrm{jet}} = 0$, $p_{\mathrm{T}}^{b-\mathrm{jet}} > 20$ GeV, $\lvert\eta^{b-\mathrm{jet}}\rvert < 2.5$		-
m_{jj}	> 100 GeV	> 500 GeV	-
ANN score	> 0.82	< 0.82	-

7.1.3 Same-sign WW Analysis

The same-sign WW analysis aims to investigate events characterized by the presence of two W bosons decaying leptonically into same-sign charged leptons and associated jets. The selection criteria for this analysis are designed to maximize the purity of the SRs and to define CRs that help constrain background contributions. The selection procedure follows the methodology outlined in the Internal Note from the Run 2 same-sign WW analysis [81].

Baseline Selection

Events are collected using trigger chains that select events based on the presence of high-p_{T} leptons. The detailed trigger information is described in Section 4.

- **Leptons:** Exactly two charged leptons with the same electric charge are required, with $p_{\mathrm{T}} > 27$ GeV. Muons must have $|\eta| < 2.5$, and electrons must have $|\eta| < 2.47$, excluding the transition region $1.37 \leq |\eta| \leq 1.52$. In the ee channel, $|\eta| < 1.37$.
- **$m_{\ell\ell'}$:** The invariant mass of the lepton pair must be greater than 20 GeV to reduce low-mass Drell-Yan background.
- **Z-veto:** In the ee channel, events with $|m_{ee} - m_Z| < 15$ GeV are vetoed to suppress $Z/\gamma^* \to ee$ background.
- **Missing Transverse Energy:** Events must have $E_{\mathrm{T}}^{\mathrm{miss}} > 30$ GeV to account for neutrinos from W decays.
- **Jets:** At least two jets with $p_{\mathrm{T}} > 65$ GeV for the leading jet and $p_{\mathrm{T}} > 35$ GeV for the subleading jet, within $|\eta| < 4.5$. Additional jets must have $p_{\mathrm{T}} > 25$ GeV.
- **b-jet Veto:** Events with any b-jets are vetoed using the DL1r tagger with an 85% efficiency working point.
- **VBF Criteria:** The invariant mass of the dijet system must be $m_{jj} \geq 500$ GeV, and the rapidity separation between the two jets must be $|\Delta y_{jj}| > 2$.

Signal Region

The SR is defined to maximize the sensitivity to the targeted signal processes while minimizing contamination from background events. The selection criteria for the SR are:

- **Signal Region:**
  - Exactly two same-sign leptons with $p_{\mathrm{T}} > 27$ GeV.
  - Leading and subleading jets with $p_{\mathrm{T}} > 65$ GeV and 35 GeV, respectively.
  - At least two jets with $p_{\mathrm{T}} > 25$ GeV.
  - Dijet invariant mass $m_{jj} \geq 500$ GeV and $|\Delta y_{jj}| > 2$.

  - b-jet veto using DL1r tagger with 85% efficiency.
  - Missing transverse energy $E_{\mathrm{T}}^{\mathrm{miss}} > 30$ GeV.
  - Z-veto in ee channel: $|m_{ee} - m_Z| > 15$ GeV.

Control Regions

To enhance the analysis, specific control regions are defined to improve the modeling of background contributions and control uncertainties in the signal extraction fit.

- $W^{\pm}Z$ – QCD **Control Region:**
  - Same selection as SR with exactly one additional signal lepton.
  - $m_{jj} > 200$ GeV.
  - Trilepton invariant mass $m_{\ell\ell\ell} > 106$ GeV to suppress radiative Z boson decays.
- **Low-m_{jj} Control Region:**
  - Same selection as SR but with $200 < m_{jj} < 500$ GeV.

The selection criteria for the signal and control regions are summarized in Table 7.3.

7.1.4 Analysis Orthogonality

While the individual analyses delineate two control regions to constrain the QCD-mediated production of WZ dibosons, the event selection criteria are not strictly mutually exclusive. This non-exclusivity results from independently optimized selection criteria in each analysis to maximize signal significance within their respective channels. To avoid data event double-counting, strict enforcement of orthogonality requirements is essential.

Given the potential overlap, a strategic decision was made to omit the dedicated $W^{\pm}Z$ – QCD CR from the same-sign WW analysis in the combined fit. Thus, the normalization of the $W^{\pm}Z$ – QCD background contribution is solely constrained by the $W^{\pm}Z$ – QCD CR from the WZ analysis. This approach simplifies the combined analysis and ensures more robust statistical inference by leveraging the more effective control region.

Table 7.3: Summary of the event selection for the signal and control regions in the same-sign WW analysis [81].

Same-sign WW analysis			
Requirement \ Regions	SR	Low-m_{jj} CR	$W^{\pm}Z - \text{QCD}$ CR
Leading and subleading lepton p_{T}	> 27 GeV		
Electron $\lvert\eta\rvert$	< 2.47 (1.37 in ee), excluding $1.37 \leq \lvert\eta\rvert \leq 1.52$		
Muon $\lvert\eta\rvert$	< 2.5		
Leading (subleading) jet p_{T}	$> 65\,(35)$ GeV		
Additional jet p_{T}	> 25 GeV		
Jet $\lvert\eta\rvert$	< 4.5		
$m_{\ell\ell}$	> 20 GeV		
$E_{\text{T}}^{\text{miss}}$	> 30 GeV		
Charge misid. $Z \to ee$ veto	$\lvert m_{ee} - m_Z\rvert > 15$ GeV		–
b-jet veto	$N_{b\text{-jet}} = 0$, $p_{\text{T}}^{b\text{-jet}} > 20$ GeV, $\lvert\eta^{b\text{-jet}}\rvert < 2.5$		
$N_{\text{veto leptons}}$	$= 0$	$= 0$	$= 1\,, p_{\text{T}} > 15$ GeV
$m_{\ell\ell\ell}$	–	–	> 106 GeV
m_{jj}	> 500 GeV	$200 < m_{jj} < 500$ GeV	> 200 GeV
$\lvert\Delta y_{jj}\rvert$	> 2		

Study on Removal of Overlapping Regions

The studies conducted on the removal of overlapping regions showed that both the WZ and same-sign WW analyses initially define a $W^{\pm}Z - \text{QCD}$ CR using distinct event selection criteria. To evaluate the impact on the combination result, the $W^{\pm}Z - \text{QCD}$ CR was excluded in each channel under the following scenarios:

- **Combined scenario 1**: $W^{\pm}Z - \text{QCD}$ region excluded in the same-sign WW channel.
- **Combined scenario 2**: $W^{\pm}Z - \text{QCD}$ region excluded in the WZ channel.

In both scenarios, the retained $W^{\pm}Z - \text{QCD}$ CR was used to constrain the background contribution. The results, summarized in Table 7.4, demonstrate the normalization factors from the individual channels before the combination and the effects of removing the $W^{\pm}Z - \text{QCD}$ CR one at a time, evaluated at a mass point of 375 GeV.

Overall, both combined scenarios yield similar results, with the nominal values largely overlapping within their uncertainties. Excluding the $W^{\pm}Z - \text{QCD}$ region in the WZ channel results in a smaller uncertainty in the corresponding normalization factor due to the larger impact of systematic uncertainties in the WZ channel's CR . However, considering the signal leakage included in the CR of the WZ channel and potential additional overlap between the SR of the WZ channel and the $W^{\pm}Z-$QCD CR of the same-sign WW analysis, *Combined scenario 1* is preferred. This decision, made during the first Editorial Board meeting[2], enhances the robustness of the analysis.

Table 7.4: Normalization factors for different configurations at the 375 GeV mass point and $\sin\theta_{\mathrm{H}} = 0.5$.

	same-sign WW	**WZ fit**	**Combined scenario 1**	**Combined scenario 2**
$\mu(W^{\pm}Z-\mathrm{QCD})$	0.69 ± 0.06	0.71 ± 0.07	0.73 ± 0.07	0.69 ± 0.06
$\mu(W^{\pm}W^{\pm}-\mathrm{EW})$	0.97 ± 0.15		0.91 ± 0.13	0.92 ± 0.13
$\mu(ZZ)$		1.05 ± 0.17	1.07 ± 0.17	1.05 ± 0.16

---

[2] Decision details available at Indico event 1422245.

7.2 Uncertainties

In high energy physics analyses, two primary types of uncertainties are typically considered: **statistical uncertainties** and **systematic uncertainties**. Statistical uncertainties arise from stochastic fluctuations in the physical processes being observed. The extent of statistical uncertainty is inversely proportional to the size of the dataset—the larger the dataset, the smaller the statistical uncertainty. This chapter provides an overview of the systematic uncertainties considered in the individual analyses as well as the strategy for combining them in the final result.

The sensitivity of this combined analysis is primarily limited by statistical uncertainties. Nevertheless, systematic uncertainties contribute to a reduction in the exclusion limits on the GM model by up to 5% when included in the combination, compared to a scenario where only statistical uncertainties are taken into account (see Figure C.1 in Appendix C.1). Thus, systematic uncertainties have a relatively minor impact on the final limits, and assumptions regarding their correlations across the two analyses do not significantly alter the overall results.

The combination strategy assumes that detector-related uncertainties are correlated between the analyses unless discrepancies in event reconstruction methods or correlation models indicate otherwise. Comparisons between treating experimental uncertainties as either fully correlated or fully uncorrelated show no significant differences in the final results. Theoretical uncertainties related to the modeling of background processes are considered uncorrelated between the analyses due to variations in phase spaces and background estimation techniques. Conversely, theoretical uncertainties related to signal process modeling are assumed to be correlated between the channels, as both analyses rely on similar techniques and use the same Monte Carlo simulation programs.

Systematic uncertainties emerge from less well-defined sources and significantly affect the precision and accuracy of experimental results. These can be broadly classified into two categories:

- *Experimental Uncertainties:* Associated with the measurement process itself, such as errors in instrument calibration, detector efficiency, or data acquisition systems.

- *Theoretical Uncertainties:* Originate from the assumptions and approximations made in theoretical models, including uncertainties in parton distribution functions.

The detailed procedures for handling each source of uncertainty are described in the following sections: experimental uncertainties in Section 7.2.1, and theoretical uncertainties in Section 7.2.2.

7.2.1 Experimental uncertainties

These sources of uncertainty include those in the calibration of the objects and algorithms used in the analyses entering the combination.

- **Lepton systematic uncertainties.** These uncertainties refer specifically to electrons and muons, and include energy and momentum scale and resolution calibration uncertainties, as well as reconstruction, identification, isolation [96, 97], and trigger efficiencies [98, 99]. All of these uncertainties apply to both the signal and simulated background distributions, and the common sources of uncertainty are treated as correlated in the combination of both channels when compatible uncertainty models are used, following the prescription from the relevant ATLAS CP groups. The systematic uncertainties and the treatment applied are listed in Table 7.5.

- **Jet systematic uncertainties.** Uncertainties in the calibration of the jet energy scale and resolution [53] are treated as uncorrelated, since different uncertainty models were used in the separate channels. The impact of these jet energy uncertainties on the combined exclusion expected limits is discussed in Appendix C.3, and it is found to be dominated by the WZ analysis[3] contribution. The impact on the combined GM exclusion expected limits from excluding all the jet energy uncertainties is always smaller than 1.5%, as displayed in Table C.7. The JVT [57] uncertainties are included and treated as correlated, while fJVT [58] uncertainties are only included in the WZ analysis. Uncertainties in the $E_{\mathrm{T}}^{\mathrm{miss}}$ calibration [100] are considered as well and the common sources of uncertainty are treated as correlated. The systematic uncertainties and the treatment applied are listed in Table 7.6.

- **Flavour tagging uncertainties.** A b-jet tagger [101] is used for the application of a b-jet veto to improve the purity in the signal region. The broad categories of

---

[3] This finding suggests that the effect of possible correlations not accounted for between the channels could be up to the order of the impact observed in the combined limits after excluding the jet energy uncertainties in the same-sign WW channel, which is smaller than 0.3%. Therefore, this is a small effect that does not change significantly the analysis results.

flavour uncertainties considered are b-tagging, c-tagging, light-jet tagging, and tagging extrapolation for high p_{T} regions. These uncertainties are treated as uncorrelated, since different uncertainty models were used, following the prescription from the ATLAS Flavour Tagging CP group. These uncertainties are listed in Table 7.7.

- **Non-prompt background uncertainty.** Systematic variations are obtained using a data-driven technique in the same-sign WW analysis, varying p_{T} (and η in the case of electrons) scale factors. In the WZ analysis, an uncertainty in the estimation of the non-prompt background is considered as well. Since both uncertainties are based on independent data-driven approaches, they are treated as uncorrelated. These uncertainties are only applied to the non-prompt contributions in the fit.
- **Data-driven charge misidentification uncertainty.** Uncertainties of the data-driven electron charge misidentification background in the same-sign WW analysis are coming from the calibration uncertainties of the charge selector tool [96]. These uncertainties are only present in the same-sign WW analysis, and are only applied to the charge misidentification background.
- **Pile-up uncertainty.** The Monte Carlo pile-up reweighting uncertainty is treated as correlated in the combination of both channels.
- **Luminosity uncertainty.** The uncertainty in the combined $2015-2018$ integrated luminosity is 0.83% [19], obtained using the LUCID-2 detector [20] for the primary luminosity measurements, complemented by measurements using the inner detector and calorimeters. This uncertainty is treated as correlated between both channels.

7.2.2 Theoretical uncertainties

These sources of uncertainty include the normalization uncertainties applied to minor backgrounds modelled using MC simulation, as well as the theoretical uncertainties on the dominant $W^{\pm}W^{\pm}$, $W^{\pm}Z$, and ZZ background contributions, accounting for the missing higher-

---

[4] Different models provided by the EGamma CP group were propagated in the two analyses. The `TOTAL_1NPCOR_PLUS_UNCOR` model was used for the WZ channel, while the `SIMPLIFIED` model was used in the same-sign WW channel. The recommendation from the group is to not correlate these models: https://twiki.cern.ch/twiki/bin/viewauth/AtlasProtected/ElectronEfficiencyCorrelationModel#Available_models

Table 7.5: Lepton systematic uncertainties. The abbreviations "S" and "B" stand for signal and background, respectively. The correlation treatment is indicated in the rightmost column.

	Channel		
Source of uncertainty	WZ	same-sign WW	Uncertainty treatment
Electron energy resolution	S + B	S + B	Correlated
Electron energy scale	S + B	S + B	Correlated
Electron reconstruction	S + B	S + B	Correlated
Electron identification	S + B	S + B	Uncorrelated[4]
Electron isolation	S + B	S + B	Correlated
Electron trigger		S + B	
Muon momentum resolution	S + B	S + B	Correlated
Muon momentum scale	S + B	S + B	Correlated
Muon reconstruction	S + B	S + B	Correlated
Muon identification	S + B	S + B	Correlated
Muon isolation	S + B	S + B	Correlated
Muon trigger		S + B	
Muon track-to-vertex association	S + B	S + B	Correlated
Muon Sagitta	S + B	S + B	Correlated

Table 7.6: Jet and $E_{\mathrm{T}}^{\mathrm{miss}}$ systematic uncertainties. The abbreviations "S" and "B" stand for signal and background, respectively. The correlation treatment is indicated in the rightmost column.

	Channel		
Source of uncertainty	WZ	same-sign WW	Uncertainty treatment
Jet energy resolution	S + B	S + B	Uncorrelated
Jet energy scale	S + B	S + B	Uncorrelated
Jet JVT	S + B	S + B	Correlated
Jet fJVT	S + B		
$E_{\mathrm{T}}^{\mathrm{miss}}$ soft term resolution	S + B	S + B	Correlated
$E_{\mathrm{T}}^{\mathrm{miss}}$ soft term scale	S + B	S + B	Correlated
$E_{\mathrm{T}}^{\mathrm{miss}}$ scale uncertainty due to tracks in jets		S + B	

Table 7.7: Flavour tagging systematic uncertainties. The abbreviations "S" and "B" stand for signal and background, respectively. The correlation treatment is indicated in the right-most column.

	Channel		
Source of uncertainty	WZ	same-sign WW	Uncertainty treatment
b-tagging	S + B	S + B	Uncorrelated
c-tagging	S + B	S + B	Uncorrelated
Light-q tagging	S + B	S + B	Uncorrelated
Tagging extrapolation	S + B	S + B	Uncorrelated

orders in pQCD, PDF, α_s, and parton shower effects. The theory uncertainties considered for the GM singly and doubly charged Higgs bosons signal processes are also discussed.

- **WZ background.** Uncertainties in the theoretical modelling by the MC generators used to evaluate the $W^{\pm}Z-$QCD and $W^{\pm}Z-$EW templates are considered. Both the WZ and same-sign WW fits constrain the $W^{\pm}Z-$QCD background normalization with a dedicated control region. Therefore, only the shape variations of the reconstructed distributions are considered for this background. Uncertainties due to higher-order QCD corrections are evaluated by varying the renormalization and factorisation scales independently by a factor two up and down, excluding variations in opposite directions. In addition, uncertainties due to the PDF and the α_s value used in the PDF determination are evaluated[5].
    - In the WZ fit, an additional modelling uncertainty in the $W^{\pm}Z-$ QCD background to account for parton shower model differences is estimated by comparing predictions of the m_{WZ} distribution from the Sherpa and MadGraph MC generators. The difference between the two predicted m_{WZ} distribution shapes is used as an uncertainty band centred around the nominal Sherpa prediction. In a similar way, a parton shower modelling uncertainty is estimated for the $W^{\pm}Z-$ EW background from the difference between Herwig and Pythia models.
    - In the same-sign WW fit, the QCD-induced $W^{\pm}Z$ background MC model suffers from m_{jj} mismodelling, which is corrected by reweighting the m_{jj} to data with

---

[5] In the same-sign WW analysis, the scales, PDF and α_s uncertainties for the $W^{\pm}Z-$ EW component are not included. The impact expected is small, since the fraction of EW events represents $\approx 20\%$ of the total $W^{\pm}Z$ background in the signal region.

other processes subtracted. The uncertainty of the reweighting function is dominated by limited data statistics in the reweighting region and is represented by corresponding parameter variations of the exponential reweighting fit function.

All these uncertainties affecting the $W^{\pm}Z$ background are treated as uncorrelated in the combined fit. These uncertainties are listed in Table 7.8.

- **Same-sign WW background.** This background contribution is only included in the same-sign WW fit. The uncertainties originating from the renormalization and factorisation scales, as well as from the PDF and the chosen value of α_{s} are evaluated in a similar way as for the $W^{\pm}Z$ background. Since the fit constrains the $W^{\pm}W^{\pm}-\mathrm{EW}$ background normalization, only shape variations are considered for this template. The NLO EW effects on the $W^{\pm}W^{\pm}-\mathrm{EW}$ prediction were derived by the authors of Ref. [102], for the fiducial region of the same-sign WW measurement, and an uncertainty on the nominal model is estimated by using an m_{jj} dependent correction factor. In addition, a parton shower modelling uncertainty is included by taking the difference between Herwig and Pythia models. These uncertainties are listed in Table 7.8.

- **ZZ background.** In the WZ fit, the ZZ background normalization is constrained with a dedicated control region. Therefore, only the shape variations of the reconstructed m_{WZ} distribution are considered. The shape uncertainties originating from the renormalization and factorisation scales, as well as from the PDF and the chosen value of α_{s} are evaluated in a similar way as for the $W^{\pm}Z$ background. In the same-sign WW fit, a 20% [103] normalization uncertainty is applied on the cross-section of the ZZ production. These uncertainties are listed in Table 7.8 and are treated as uncorrelated in the combined fit.

- **Normalization of small backgrounds.** Normalization uncertainties of minor prompt lepton backgrounds are included. In the WZ fit, a normalization uncertainty of 20% is assigned to the $t\bar{t}V$ and VVV cross-sections from the QCD scale and PDF uncertainties [104, 105, 106]. In the same-sign WW fit, a 30% [103, 107] normalization uncertainty is applied on the cross-section of the VVV and top quark processes production. In addition, a 40% normalization is applied on the $V\gamma$ background MC estimation, motivated by the scale factor uncertainties of the electron charge selector tool [96]. Since different MC simulation samples were used for the estimation of the backgrounds described above, the uncertainties are treated as uncorrelated in the combined fit. These uncertainties are listed in Table 7.8.

- **Signal model.** Theory uncertainties affecting the $H_5^{\pm}$ and $H_5^{\pm\pm}$ signal simulations, which account for the effects of variations of renormalization and factorisation scales, PDF, and choice of α_s are propagated through the fit combination. These normalization uncertainties were estimated at NNLO in pQCD and reported in Tables 140 and 141 (Tables 142 and 143) of Ref. [74] for the $H_5^{\pm}$ ($H_5^{\pm\pm}$) signal[6]. The uncertainties were derived for a signal model using $\sin\theta_\mathrm{H} = 1$, however, since the cross-section is proportional to $\sin^2\theta_H$, the uncertainty does not depend on the $\sin\theta_\mathrm{H}$ parameter and can be applied to our model. These normalization uncertainties are treated as correlated between $H_5^{\pm}$ and $H_5^{\pm\pm}$ signal simulations in the combined fit. In addition, in the same-sign WW fit, shape uncertainties for the scale variations, PDF, and choice of α_s were derived with the MadGraph MC generator. These shape uncertainties are not available for the WZ analysis, and are included as well in the same-sign WW fit. Moreover, an uncertainty due to the uncalculated NLO EW corrections is adopted, as recommended in Ref. [74]. This is a ±7% flat normalization uncertainty, and it is treated as correlated in the combination. These uncertainties are listed in Table 7.8.

---

[6] Some of the mass points used in this analysis are not displayed in the Tables (multiples of 25, such as 225, 275, 325, 375, etc.). However, the granularity of the mass points provided is dense enough to do an interpolation by averaging the uncertainties of the adjacent mass points in each case.

Table 7.8: Theoretical systematic uncertainties. The abbreviations “S” and “B” stand for signal and background, respectively. The correlation treatment is indicated in the rightmost column.

	Channel		
Source of uncertainty	WZ	same-sign WW	Uncertainty treatment
$W^{\pm}W^{\pm}$ – EW scale		B	
$W^{\pm}W^{\pm}$ – EW PDF + α_{s}		B	
$W^{\pm}W^{\pm}$ – EW modelling		B	
$W^{\pm}W^{\pm}$ – EW NLO correction		B	
$W^{\pm}W^{\pm}$ – QCD scale		B	
$W^{\pm}W^{\pm}$ – QCD PDF + α_{s}		B	
$W^{\pm}W^{\pm}$ – QCD modelling		B	
$W^{\pm}W^{\pm}$ – QCD NLO correction		B	
$W^{\pm}Z$ – EW scale	B		
$W^{\pm}Z$ – EW PDF	B		
$W^{\pm}Z$ – EW modelling	B		
“MjjRewStat” (reweighting, same-sign WW)		B	
“MjjRewScale” (reweighting, same-sign WW)		B	
“MjjRewPDF” (reweighting, same-sign WW)		B	
$W^{\pm}Z$ – QCD scale	B	B	Uncorrelated
$W^{\pm}Z$ – QCD PDF	B	B	Uncorrelated
$W^{\pm}Z$ – QCD α_{s}		B	
$W^{\pm}Z$ – QCD modelling	B		
ZZ – QCD scale	B		
ZZ – QCD PDF	B		
Triboson normalization	B	B	Uncorrelated
ZZ normalization		B	
Top normalization		B	
$V\gamma$ normalization		B	
GM signal PDF + α_{s} (shape, same-sign WW)		S	
GM signal scale (shape, same-sign WW)		S	
GM signal NNLO scale	S	S	Correlated
GM signal NNLO PDF	S	S	Correlated
GM signal NNLO α_{s}	S	S	Correlated
GM signal NLO EW	S	S	Correlated

7.3 Statistical Analysis

Statistics is employed in this analysis to establish a quantitative connection between the observed number of events of signal and background and the theoretical cross section, σ_{phys} (see Eq. 7.1). This relationship serves as the foundation for interpreting the results by evaluating the compatibility of the observed data with different hypotheses using the framework of hypothesis testing. The cross section, σ_{phys}, is defined as:

$$\sigma_{\text{phys}} = \frac{(N_{\text{obs}} - N_{\text{bkgd}})}{L_{\text{int}}\, A\, \epsilon}, \tag{7.1}$$

where N_{obs} is measured by counting the number of events after the signal event selection, N_{bkgd} is estimated from data and/or the MC simulation samples, L_{int} is the integrated luminosity of the dataset, A is the acceptance of the event selection, and ϵ is the detection efficiency. This formula establishes a direct connection between the observed number of events and the theoretical cross section, accounting for experimental conditions and detector effects.

By incorporating the acceptance and efficiency factors, σ_{phys} provides a more accurate estimation of the signal production rate after correcting for detector-level effects. The resulting value of σ_{phys} is subsequently used as an input to the profile likelihood fit, allowing for the extraction of the signal strength parameter, μ, and the setting of exclusion limits.

In this chapter, the general statistical tools commonly used in high energy physics (HEP) analyses are introduced 7.3.2, followed by a detailed reproduction of the statistical methods used to analyze the two individual datasets 7.3.3, following the same approach as in the original studies. Subsequently, the results of the combined analysis are presented to provide a unified interpretation of the signal and background processes 7.3.4.

7.3.1 Combination Strategy

The strategy is to combine two orthogonal ATLAS analyses which are independently searching for final states in which a charged Higgs boson produced via VBF decays into a pair of WZ boson pairs (singly-charged Higgs) and same-sign WW (doubly-charged Higgs) in fully leptonic final states in association with two jets. Hence, this combination analysis leverages histograms from two distinct analyses. These histograms include both the signal and background MC simulations, as well as background estimations obtained through data-driven methods. Subsequent fitting studies utilize these histograms to perform simultaneous fits on both channels. The ultimate goal is to obtain more stringent constrains on the $\sin\theta_{\mathrm{H}}$ parameter of the Georgi-Machacek model described in Section 2. Once the statistical combination phase described in Section 7.3 is completed, the local and global p–values are extracted, and results are presented in the format of 1–dimensional exclusion limits. These limits are provided on the cross-section times branching fraction ($\sigma \times \mathcal{B}$) of the signal process versus the mass of the resonant charged Higgs signal under consideration. Therefore, these limits are provided separately for the $H_5^{\pm}$ and $H_5^{\pm\pm}$ cases. In addition, the results are also interpreted within the framework of the GM model, establishing constraints on the $\sin\theta_{\mathrm{H}}$ parameter as a function of the mass of the resonant charged Higgs, which is degenerate for the states of the custodial quintuplet ($H_5^{\pm\pm}$, $H_5^{\pm}$, and H_5^{0}).

Both analyses were optimised for the best sensitivity as standalone searches and orthogonality is evaluated when entering the combined result. Each individual analysis considers its own signal, control, and validation regions, which are not simultaneously normalised except for the $W^{\pm}Z$ – QCD and the charged Higgs signal contributions to both analyses. The orthogonality of the two analyses is already discussed in Section 7.1.4.

7.3.2 Statistics Tools

Profile Likelihood Fit

The profile likelihood fit is the primary statistical tool used to extract signal strengths and set exclusion limits on the cross sections of the signal processes. In this method, a likelihood function $\mathcal{L}(\mu, \theta)$ is constructed based on the observed event yields in the SR and CRs, as well as the expected yields predicted by the theoretical model. The likelihood is a function of the signal strength parameter, which is the Parameter of Interest (PoI), μ, and a set of nuisance parameters (NPs), θ, that account for systematic uncertainties. The signal strength parameter μ is defined as a multiplicative factor applied to the theoretical signal cross-section, while θ represents the uncertainties that affect both signal and background expectations.

The binned likelihood function $\mathcal{L}(\mu, \theta)$ is constructed as the product of Poisson probability terms over all bins considered in the analysis and a number of Gaussian and log-normal priors for the NPs associated with systematic uncertainties. The test statistic used for hypothesis testing is the profile likelihood ratio, defined as [108]:

$$\tilde{q}_\mu = \begin{cases} -2\ln \frac{\mathcal{L}(\mu,\hat{\hat{\theta}}(\mu))}{\mathcal{L}(0,\hat{\hat{\theta}}(0))} & \hat{\mu} < 0, \\ -2\ln \frac{\mathcal{L}(\mu,\hat{\hat{\theta}}(\mu))}{\mathcal{L}(\hat{\mu},\hat{\theta})} & 0 \leq \hat{\mu} \leq \mu, \\ 0 & \hat{\mu} > \mu, \end{cases}$$

where $\hat{\mu}$ and $\hat{\theta}$ are the values of the parameters that maximize the likelihood function, and $\hat{\hat{\theta}}(\mu)$ are the values of the nuisance parameters that maximize the likelihood function for a fixed value of μ. This test statistic is used to determine whether the observed data are compatible with the background-only hypothesis, i.e., $\mu = 0$.

Hypothesis Testing

Hypothesis testing is a fundamental tool used to evaluate whether the observed data are consistent with a given theoretical model. In this context, the null hypothesis (H_0) typically represents the background-only scenario, while the alternative hypothesis (H_1) includes the potential signal contribution.

The primary goal of hypothesis testing is to calculate a test statistic that quantifies the level of agreement between the data and each hypothesis. This test statistic, such as the profile likelihood ratio $\tilde{q}_\mu$, is then used to derive p-values, which indicate the probability of observing data as extreme as (or more extreme than) the actual data, assuming that the null hypothesis is true. If the p-value is below a predefined threshold, typically 0.05, the null hypothesis is rejected in favor of the alternative hypothesis.

In this analysis, the CL_s method [109] is used to set upper limits on the signal cross-section. This method modifies the traditional p-value calculation by taking into account the compatibility of both the null hypothesis and the alternative hypothesis, thereby providing a more conservative exclusion criterion. The CL_s value is calculated using the ratio of the confidence levels, ensuring that the resulting exclusion limits are not overly sensitive to fluctuations in the background estimation.

$$\mathrm{CL}_s = \frac{\mathrm{CL}_{s+b}}{\mathrm{CL}_b} = \frac{p_{s+b}}{1 - p_b} \tag{7.2}$$

The confidence levels CL_{s+b} and CL_b are defined as integrals over the probability density functions of the test statistic under the null and alternative hypotheses, respectively:

$$\mathrm{CL}_{s+b} = \int_{t_{\mathrm{obs}}}^{\infty} dt\, p_0(t|H_0) \qquad \mathrm{CL}_b = \int_{t_{\mathrm{obs}}}^{\infty} dt\, p_1(t|H_1) \tag{7.3}$$

7.3.3 Reproduction of the original separate fitting

To validate the combination, the original separate fits for the two individual analyses are reproduced. In the WZ $H_5^{\pm}$ analysis, the invariant mass of the WZ candidates, m_{WZ}, is used as the discriminating variable in the signal extraction fit. For the same-sign WW $H_5^{\pm\pm}$ analysis, the invariant mass of the two leading jets m_{jj}, along with the transverse mass distribution of the dilepton system and the missing transverse momentum m_{T}, is used[7].

In both separate analyses, the bin widths of the discriminating variables were chosen to optimize the sensitivity to the signal while minimizing the impact of statistical fluctuations. The binning scheme used for the distributions of m_{WZ}, m_{jj}, and m_{T} in these fits is identical to that in the original analyses of $H_5^{\pm}$ [79] and $H_5^{\pm\pm}$ [81]. The details of the binning are provided in Table 7.9.

The signal and control region definitions, as well as the normalization parameters in the fit, follow the same definitions as in the original WZ [79] and same-sign WW [81] analyses. The only exception is that the $W^{\pm}Z-$QCD CR of the same-sign WW analysis is dropped to guarantee orthogonality between both channels, as discussed in Section 7.1.4. The WZ (same-sign WW) fits are performed for each of the 20 (23) mass points between 200 GeV and 1 TeV (3 TeV). For illustration, fit results using the H_5 signal simulation corresponding to the mass point 375 GeV and $\sin\theta_{\mathrm{H}} = 0.5$ are shown in this section.

WZ $H_5^{\pm}$ signal extraction fit

The fit is performed in one dimension, using the invariant mass distributions of the $W^{\pm}Z$ candidates, m_{WZ}. A short summary of the fit model is provided in Table 7.10.

The post-fit m_{WZ} distribution in the signal region, as well as in the WZ-QCD and ZZ control regions, is shown in Figure 7.2. In the signal region (Figure 7.2a), a distinct peak in the data is observed in the bin range of 350 to 400 GeV. When excluding the signal

---

[7] The transverse mass is defined as $m_{\mathrm{T}} = \sqrt{(E_{\mathrm{T}}^{ll} + E_{\mathrm{T}}^{\mathrm{miss}})^2 - |\vec{p}_{\mathrm{T}}^{\,ll} + \vec{E}_{\mathrm{T}}^{\mathrm{miss}}|^2}$, where E_{T}^{ll} is the transverse energy of the dilepton system, $\vec{p}_{\mathrm{T}}^{\,ll}$ is the vector sum of the lepton transverse momenta, and $\vec{E}_{\mathrm{T}}^{\mathrm{miss}}$ is the missing transverse momentum vector. This observable provides good discrimination between resonant signal and non-resonant background processes.

Table 7.9: Summary of bin ranges used for the different regions entering the WZ $H_5^{\pm}$ and same-sign WW $H_5^{\pm\pm}$ signal extraction fits. The $W^{\pm}Z$ – QCD CR of the same-sign WW analysis is also displayed, though it is dropped for the fits presented in this section to guarantee orthogonality between both channels.

WZ $H_5^{\pm}$ signal extraction fit		
Region	Variable	Binning
SR	m_{WZ}	9 bins: $[150, 200, 230, 270, 310, 350, 390, 480, 660, 1200]$, plus overflow in the last bin.
CR $W^{\pm}Z$ – QCD	m_{WZ}	9 bins: $[150, 200, 230, 270, 310, 350, 390, 480, 660, 1200]$, plus overflow in the last bin.
CR ZZ	m_{WZ}	17 bins: $[150, 200, 250, 300, 350, 400, 450, 500, 550, 650, 750, 850, 950, 1100, 1250, 1400, 1700, 3000]$

Same-sign WW $H_5^{\pm\pm}$ signal extraction fit		
Region	Variable	Binning
SR	m_{jj}	5 bins: $[500, 850, 1450, 2100, 2550, 5000]$
	m_{T}	8 bins: $[0, 100, 180, 230, 280, 350, 500, 800, 1500]$, plus overflow in the last bin.
CR $W^{\pm}Z$ – QCD	m_{jj}	1 bin: $[200, 3000]$
CR Low-m_{jj}	m_{jj}	1 bin: $[200, 500]$
	m_{T}	8 bins: $[0, 100, 180, 230, 280, 350, 500, 800, 1500]$, plus overflow in the last bin.

contribution (shown in purple), the background prediction alone underestimates the observed data in this region. The inclusion of the signal component improves the overall agreement, demonstrating its necessity in describing the observed distribution. The post-fit distributions in the WZ-QCD and ZZ control regions, presented in Figures 7.2b and 7.2c, respectively, confirm the validity of the background modeling. Both control regions show good agreement between the data and the fit prediction within uncertainties, ensuring a reliable background estimation.

The normalization parameters for the $H^{\pm}$ signal, QCD WZ, and ZZ processes are displayed in Figure 7.3. These parameters, treated as freely floating in the fit, are well constrained by data in both the SRs and the dedicated CRs. The results remain consistent with the original analysis [79], reinforcing the robustness of the fit.

The impact of nuisance parameters on the fit is illustrated in Figure 7.4. The absence of significant pulls or over-constraining effects indicates a well-behaved fit, where systematic uncertainties are effectively accounted for and do not introduce significant bias.

The ranking of systematic uncertainties affecting the signal strength μ is presented in Figure 7.5. The figure compares the pre-fit (open bars) and post-fit (filled bars) impacts of

Table 7.10: Overview of the WZ $H_5^{\pm}$ signal extraction fit model described in this section.

WZ $H_5^{\pm}$ signal extraction fit	
Region	Description
SR	9 bins in m_{WZ}
CR $W^{\pm}Z$	9 bins in m_{WZ}
CR ZZ	17 bins in m_{WZ}
Parameter of interest	$\mu(H_5)$
Normalization parameters	$\mu(W^{\pm}Z-\mathrm{QCD})$ and $\mu(ZZ)$
Observables	One dimensional fit in m_{WZ}

the leading NPs, quantified as the shift in μ when each NP is varied by $\pm 1\sigma$ before and after fitting.

To better understand the cumulative effects of different uncertainty sources, individual NPs are further grouped into broader categories, with their combined impacts summarized in Table 7.11. This grouping provides a clearer picture of the dominant sources of uncertainty, revealing that jet-related uncertainties and background modeling contribute most significantly to the total systematic uncertainty. The data statistical uncertainty remains the largest single contributor to the total uncertainty, highlighting the importance of increased data statistics in future studies.

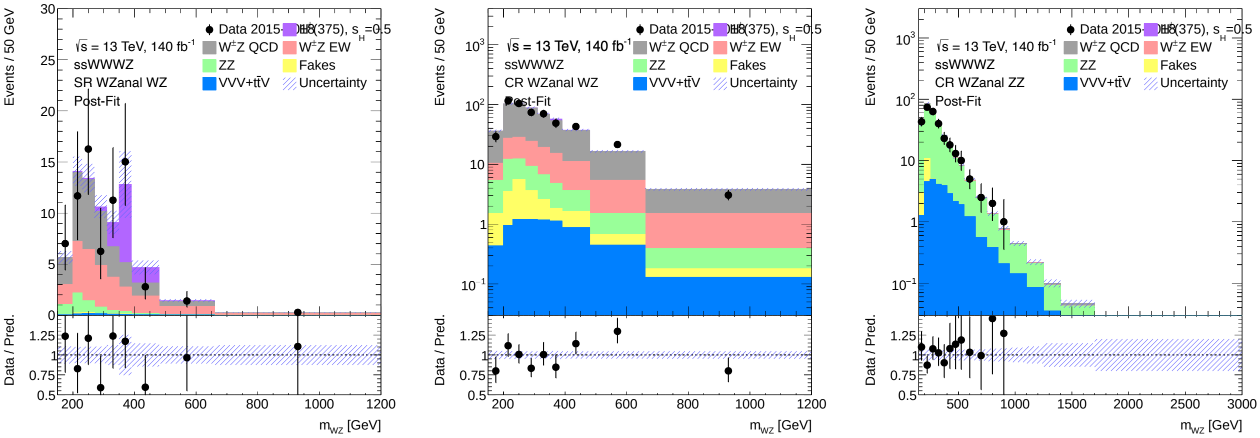

(a) (b) (c)

Figure 7.2: Post-fit m_{WZ} distributions in the $W^{\pm}Z$ signal region (a), $W^{\pm}Z-$QCD control region (b), and ZZ control region (c) for the signal-extraction fit using the $H_5^{\pm}$ signal simulations corresponding to the mass point 375 GeV and $\sin\theta_{\text{H}} = 0.5$. The hatched error band represents the total uncertainty of the model.

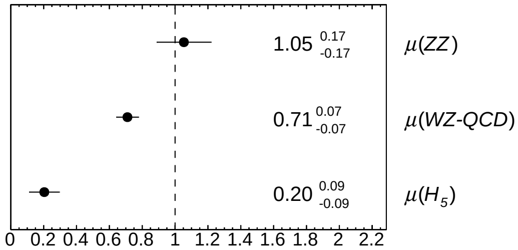

Figure 7.3: Normalization factors floating in the fit for a signal hypothesis of a singly charged Higgs boson with $m_{\text{H}_5} = 375$ GeV.

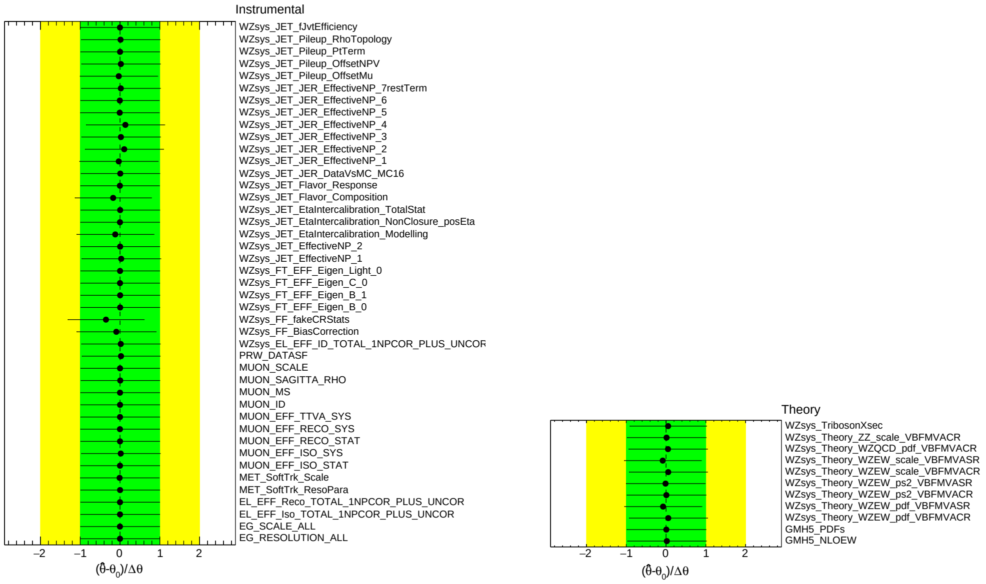

(a) (b)

Figure 7.4: Nuisance parameter pulls for the experimental (a) and theoretical (b) components.

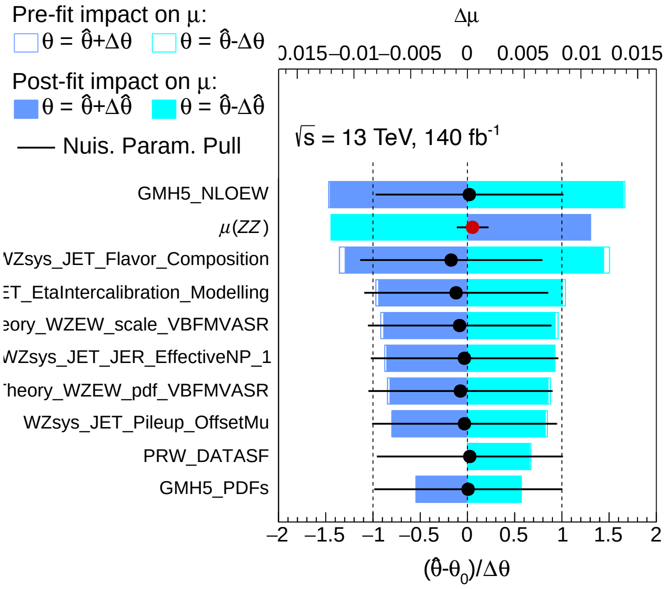

Figure 7.5: Ranking of the systematic nuisance parameters included in the fit according to their impact on the measured signal strength.

Table 7.11: Relative uncertainties in their best-fit signal-strength parameter, μ, for a GM signal of mass $m_{\mathrm{H}_5} = 375$ GeV.

Source of uncertainty	$\Delta\mu/\mu\,[\%]$
GM EW NLO	6
GM Scales	0 (pruned)
GM PDFs	2
$W^{\pm}Z$-QCD + ZZ normalization	6
$W^{\pm}Z$ background: theory unc.	5
ZZ background: theory unc.	0.1
Lepton	0.5
Jet uncertainty	10
MC statistical uncertainty	5
Fake/non-prompt	0.2
Other	1
Total systematic uncertainty	17
Data statistical uncertainty	42
Total	45

Same-sign WW $H_5^{\pm\pm}$ signal extraction fit

A two-dimensional fit is performed using the invariant mass of the two tagging jets m_{jj} and the transverse mass distribution of the dilepton system and the missing transverse momentum m_{T}, which provides good discrimination between resonant signal and non-resonant background processes. A short summary of the fit model is provided in Table 7.12.

Table 7.12: Overview of the same-sign WW $H_5^{\pm\pm}$ signal extraction fit model described in this section.

Same-sign WW $H_5^{\pm\pm}$ signal extraction fit	
Region	Description
SR	5 bins in m_{jj} and 8 bins in m_{T}
CR Low-m_{jj}	1 bin in m_{jj} and 8 bins in m_{T}
Parameter of interest	$\mu(H_5)$
Normalization parameters	$\mu(W^{\pm}Z-\mathrm{QCD})$ and $\mu(W^{\pm}W^{\pm}-\mathrm{EW})$
Observables	Two dimensional fit in m_{jj} and m_{T}

The post-fit distributions in the signal regions are shown in Figure 7.6 as a function of m_{jj} and m_T. Since the same-sign WW fit is performed using five m_{jj} regions, the m_T post-fit distributions for each of the m_{jj} regions are shown in Figure 7.7. The mismatch of data points to the known backgrounds allows the signal to be extracted. The post-fit distribution in the Low-m_{jj} control region of the same-sign WW fit is shown in Figure 7.8, overall the histograms are within the data error bars, confirming the background modeling accuracy.

The normalization parameters for the $H^{\pm\pm}$ signal, EW $ssWW$, and QCD WZ processes are shown in Figure 7.9. These parameters are freely floating in the fit and are constrained by the data in both the SRs and dedicated CRs. Compared to the original same-sign WW analysis [81], the absence of a dedicated WZ-QCD control region results in larger uncertainties for the WZ-QCD normalization factor compared to the original analysis.

The impact of the nuisance parameters on the fit is illustrated in Figure 7.10. No significant pulls or over-constraining effects are visible, suggesting a stable and reliable fit.

The ranking of systematic uncertainties affecting the signal strength μ is presented in Figure 7.11. The most impactful nuisance parameter is $\mu(W^{\pm}W^{\pm}-EW)$, indicating that the leading uncertainty stems from the normalization of the EW $ssWW$ process. Additionally, significant contributions arise from jet-related uncertainties and QCD background modeling, as shown in the ranking plot.

The grouped impact of systematic uncertainties on the extracted signal strength is summarized in Table 7.13. The dominant sources of uncertainty include the combined normalization uncertainty of WZ-QCD and EW $ssWW$ (40%), jet uncertainties (8%), and Monte Carlo statistical uncertainties (8%). The total systematic uncertainty is 45%, with the largest individual contribution coming from the normalization of diboson processes. Data statistical uncertainty remains substantial at 35%, highlighting the potential for future improvements with increased dataset size.

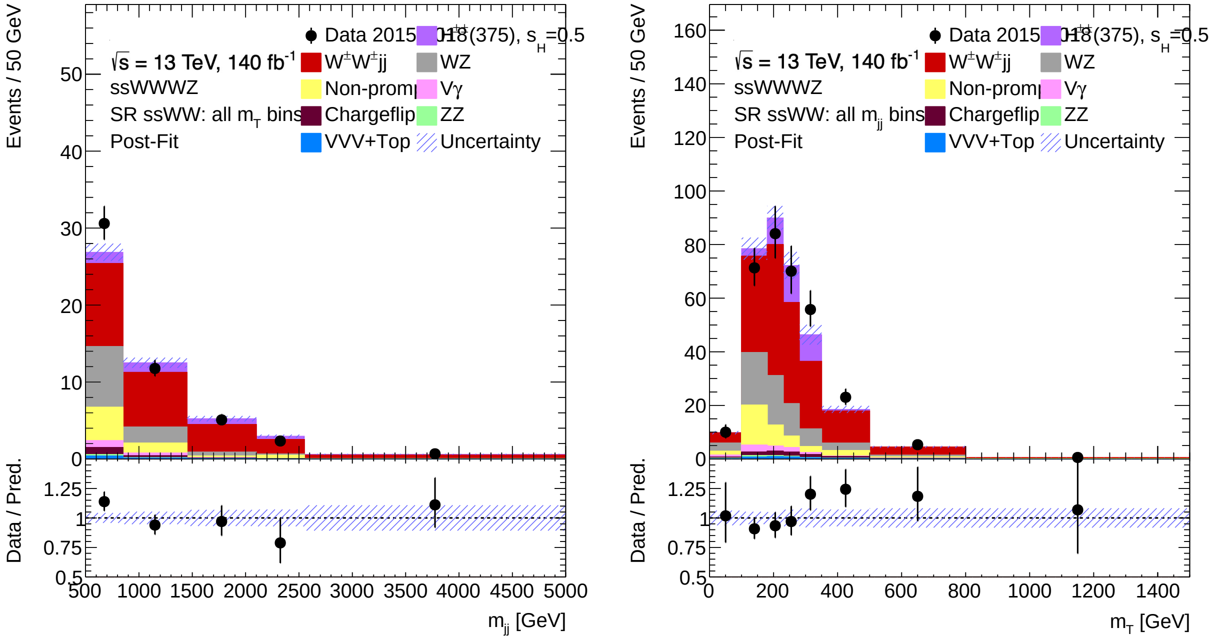

(a)

(b)

Figure 7.6: Post-fit m_{jj} (a), and m_{T} (b) inclusive distributions in the signal region for the signal-extraction fit using the $H_5^{\pm\pm}$ signal simulations corresponding to the mass point 375 GeV and $\sin\theta_{\mathrm{H}} = 0.5$. The hatched error band represents the total uncertainty of the model.

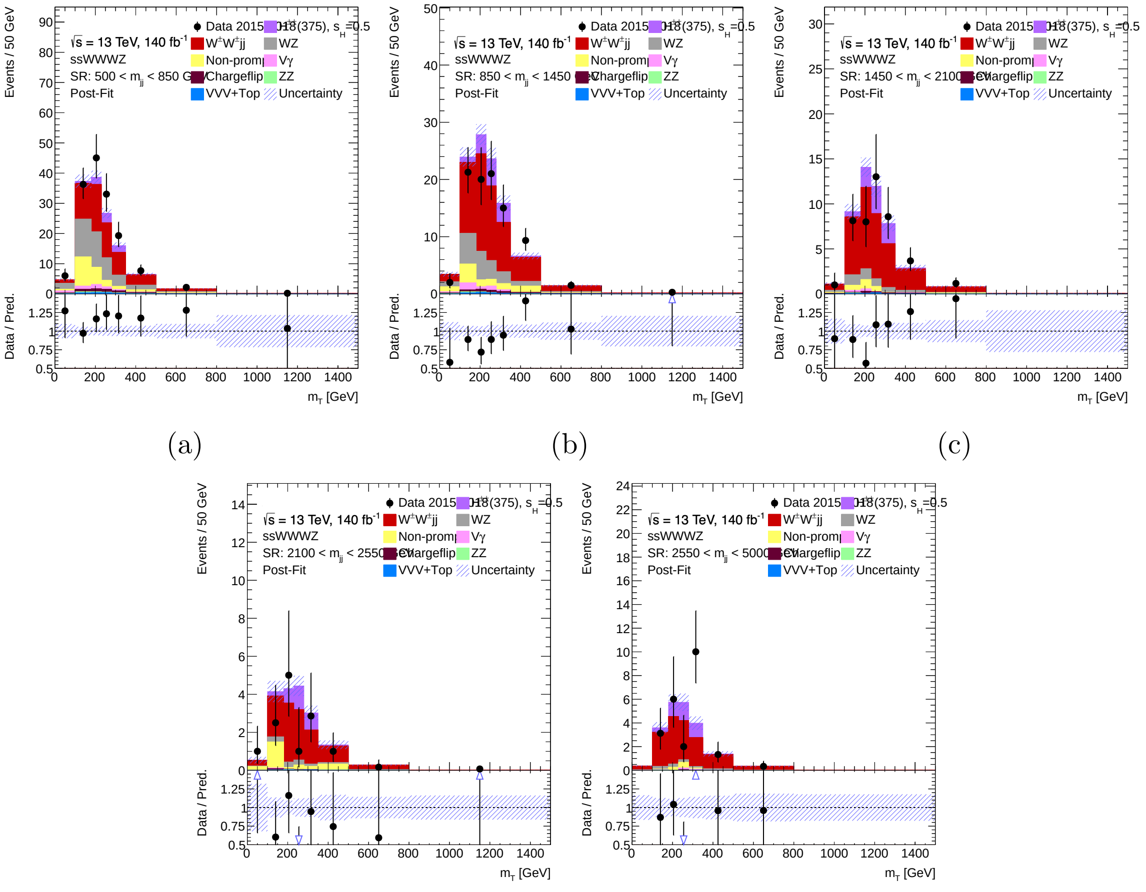

(a) (b) (c)

(d) (e)

Figure 7.7: Post-fit m_{T} distributions in the signal region in different ranges of the dijet invariant mass, m_{jj}, for the signal-extraction fit using the $H_5^{\pm\pm}$ signal simulations corresponding to the mass point 375 GeV and $\sin\theta_{\mathrm{H}} = 0.5$. The hatched error band represents the total uncertainty of the model.

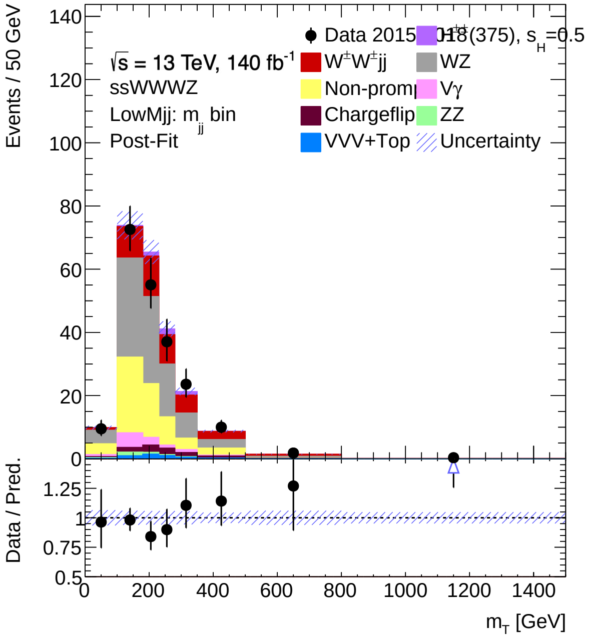

Figure 7.8: Post-fit m_T distribution in the Low-m_{jj} control region used for the signal-extraction fit. The fit is performed using the $H_5^{\pm\pm}$ signal simulations corresponding to the mass point 375 GeV and $\sin\theta_\mathrm{H} = 0.5$. The hatched error band represents the total uncertainty of the model.

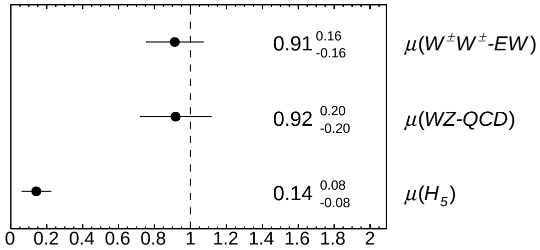

Figure 7.9: Normalization factors floating in the fit for a signal hypothesis of a doubly charged Higgs boson with $m_{\mathrm{H}_5} = 375$ GeV.

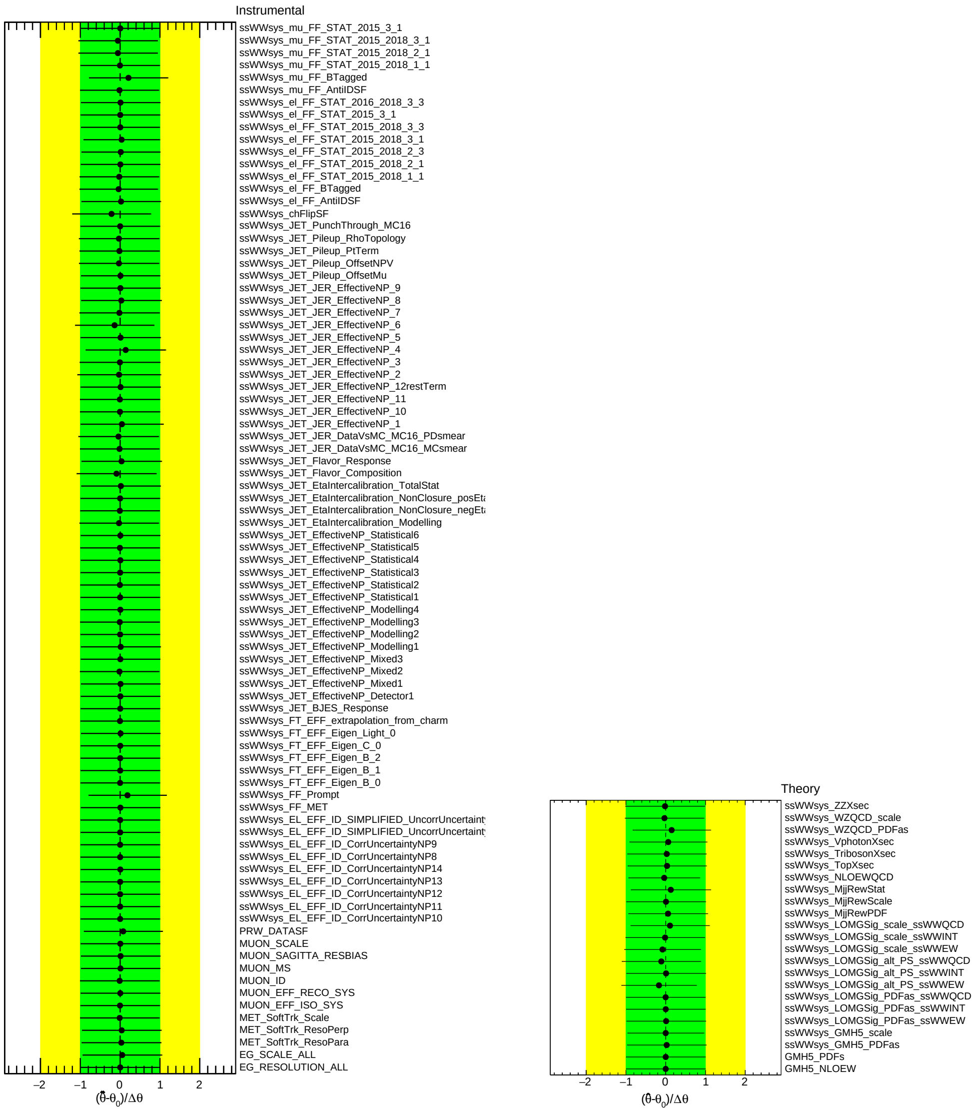

(a) (b)

Figure 7.10: Nuisance parameter pulls for the experimental (a) and theoretical (b) components.

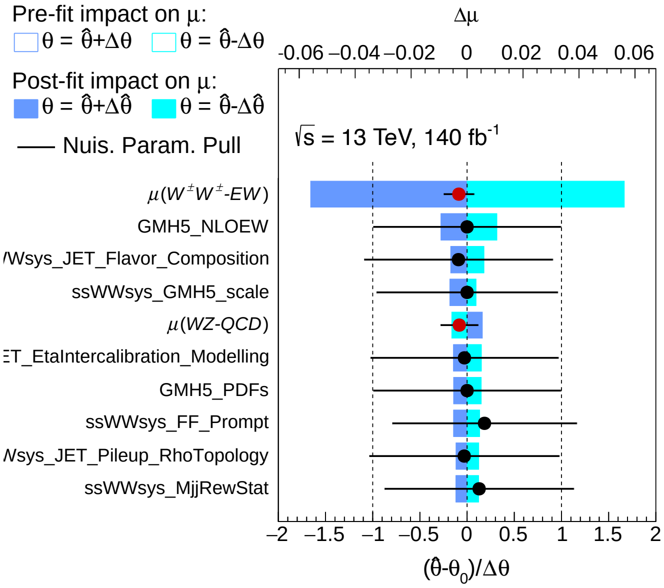

Figure 7.11: Ranking of the systematic nuisance parameters included in the fit according to their impact on the measured signal strength.

Table 7.13: Relative uncertainties in their best-fit signal-strength parameter, μ, for a GM signal of mass $m_{\mathrm{H}_5} = 375$ GeV.

Source of uncertainty	$\Delta\mu/\mu\,[\%]$
GM EW NLO	7
GM Scales	3
GM PDFs	3
$W^{\pm}Z$-QCD + $W^{\pm}W^{\pm}$-EW normalization	40
$W^{\pm}W^{\pm}$ background: theory unc.	2
$W^{\pm}Z$ background: theory unc.	3
Lepton	0.4
Jet uncertainty	8
MC statistical uncertainty	8
Fake/non-prompt	5
Charge-flip	0.8
Other	1
Total systematic uncertainty	45
Data statistical uncertainty	35
Total	57

7.3.4 Combination fit

The combination of the two separate analyses is achieved by constructing a joint likelihood function that incorporates the information from both channels. This combined likelihood function allows for a global fit, taking into account the shared and independent uncertainties between the two analyses. The combined fit provides a unified interpretation of the results and enhances the overall sensitivity to the signal processes compared to the individual fits alone. The individual fit workspaces for the WZ and same-sign WW fits are combined using the "Multifit" functionality available in the TRExFitter fitting framework [110]. This functionality provides a convenient way to compare and combine workspaces and results for individual config files[8]. A short summary of the fit model is provided in Table 7.14.

Table 7.14: Overview of the Combination signal extraction fit model described in this section.

Combination signal extraction fit	
Region	Description
SR WZ	9 bins in m_{WZ}
SR same-sign WW	5 bins in m_{jj} and 8 bins in m_{T}
CR ZZ	17 bins in m_{WZ}
CR $W^{\pm}Z-\mathrm{QCD}$	9 bins in m_{WZ}
CR Low-m_{jj}	1 bin in m_{jj} and 8 bins in m_{T}
Parameter of interest	$\mu(H_5)$
Normalization parameters	$\mu(W^{\pm}Z-\mathrm{QCD})$, $\mu(ZZ)$ and $\mu(W^{\pm}W^{\pm}-\mathrm{EW})$
Observables	m_{WZ}, m_{jj} and m_{T}

The normalization parameters for EW $ssWW$, and QCD WZ processes are shown in Table 7.15 for the separate fits and the combination. The normalization parameters from the combination exhibit significant overlap with the individual ones, given the associated uncertainties. Furthermore, the combined signal strength values, shown in Table 7.16, lie between the values extracted from the two individual channels, demonstrating the consistency of the combination approach. The post-fit distributions using the combination normalization parameters are shown in Figure 7.12 for the WZ distributions, and Figures 7.13, 7.14, and 7.15

---

[8] Details are provided in the TRExFitter documentation page: https://trexfitter-docs.web.cern.ch/trexfitter-docs/inference/multifit

for the same-sign WW distributions. Some deviations from the expected background model are observed.

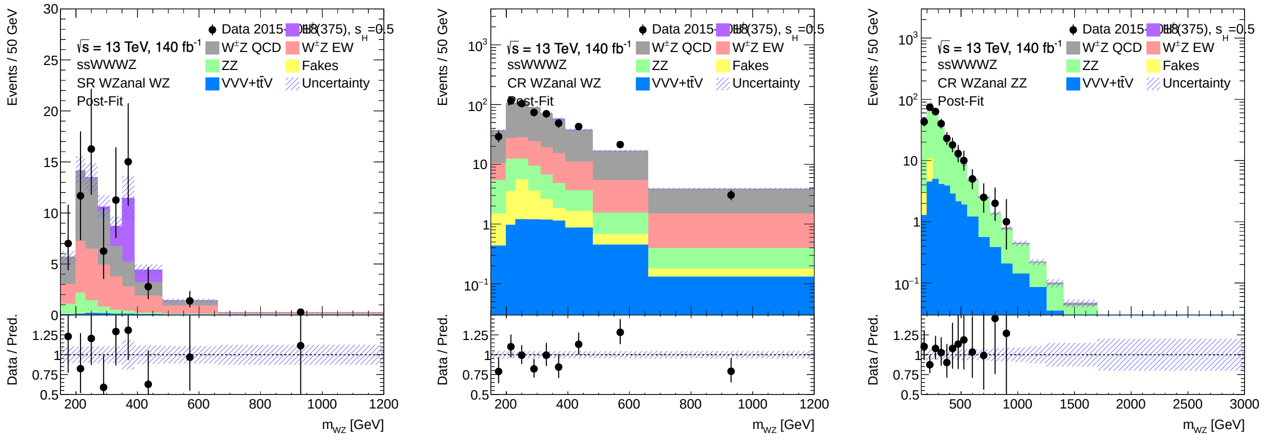

(a) (b) (c)

Figure 7.12: Post-fit m_{WZ} distributions with the combination normalization parameters in the $W^{\pm}Z$ signal region (a), $W^{\pm}Z-\mathrm{QCD}$ control region (b), and ZZ control region (c) for the signal-extraction fit using the $H_5^{\pm}$ signal simulations corresponding to the mass point 375 GeV and $\sin\theta_{\mathrm{H}} = 0.5$. The hatched error band represents the total uncertainty of the model.

Table 7.15: Normalization factors floating in the fit for a signal hypothesis of a singly or doubly charged Higgs boson with $m_{\mathrm{H}_5} = 375$ GeV.

Parameter / Fit	Same-sign WW	WZ	Combination
$\mu(W^{\pm}Z-\mathrm{QCD})$	0.92 ± 0.20	0.71 ± 0.07	0.73 ± 0.07
$\mu(W^{\pm}W^{\pm}-\mathrm{EW})$	0.91 ± 0.16		0.91 ± 0.13
$\mu(ZZ)$		1.05 ± 0.17	1.07 ± 0.17

The impact of the nuisance parameters on the fit is illustrated in Figure 7.16. The black lines indicate systematics that predominantly affect the same-sign WW analysis, while the red lines correspond to those from the WZ channel. The combined impact, represented by the blue lines, shows no evidence of significant pulls or overconstraints, suggesting that the fit remains healthy and that systematic uncertainties are well controlled.

The ranking of systematic uncertainties in the combination fit is presented in Figure 7.17. The dominant contributions arise from the signal strength of EW $ssWW$ and ZZ, which exhibit the largest impact. Additionally, theoretical uncertainties related to the GMH5 NLO

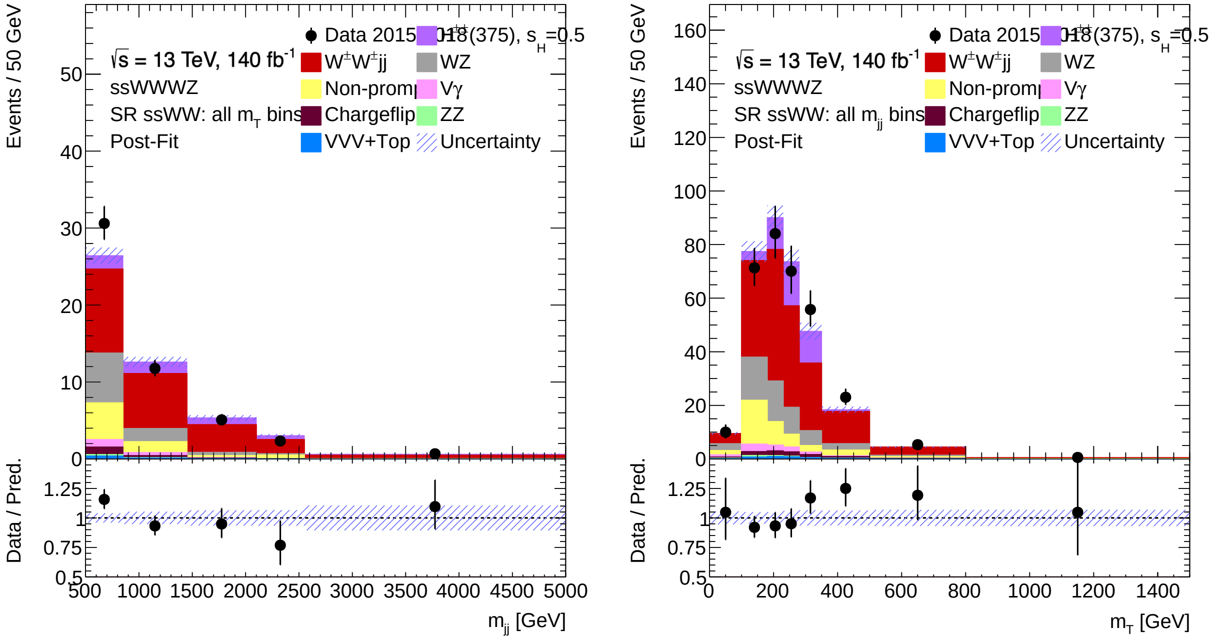

(a) (b)

Figure 7.13: Post-fit m_{jj} (a), and m_T (b) inclusive distributions with the combination normalization parameters in the signal region for the signal-extraction fit using the $H_5^{\pm\pm}$ signal simulations corresponding to the mass point 375 GeV and $\sin\theta_\mathrm{H} = 0.5$. The hatched error band represents the total uncertainty of the model.

corrections, PDFs, and scale variations for the doubly charged Higgs signal play a significant role. Jet-related uncertainties also contribute notably, as indicated in the ranking plot. This confirms that both theoretical modeling and experimental effects are key factors in the final signal extraction.

Table 7.16: Signal strength for a hypothesis of a singly or doubly charged Higgs boson with $m_{\mathrm{H}_5} = 375$ GeV.

Fit type	Signal strength
WZ	$\mu = 0.20 \pm 0.09$
Same-sign WW	$\mu = 0.14 \pm 0.08$
Combination	$\mu = 0.17 \pm 0.06$

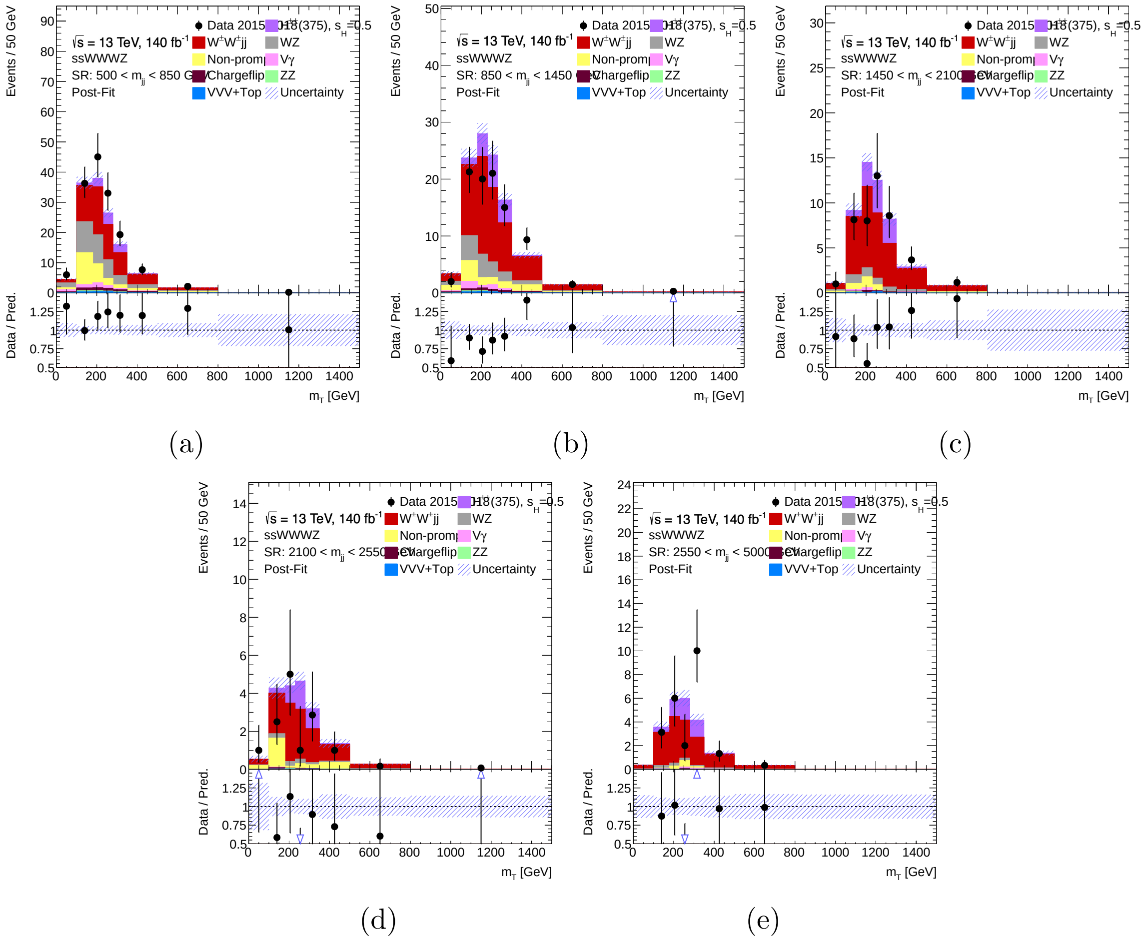

(a) (b) (c)

(d) (e)

Figure 7.14: Post-fit m_{T} distributions with the combination normalization parameters in the signal region in different ranges of the dijet invariant mass, m_{jj}, for the signal-extraction fit using the $H_5^{\pm\pm}$ signal simulations corresponding to the mass point 375 GeV and $\sin\theta_{\mathrm{H}} = 0.5$. The hatched error band represents the total uncertainty of the model.

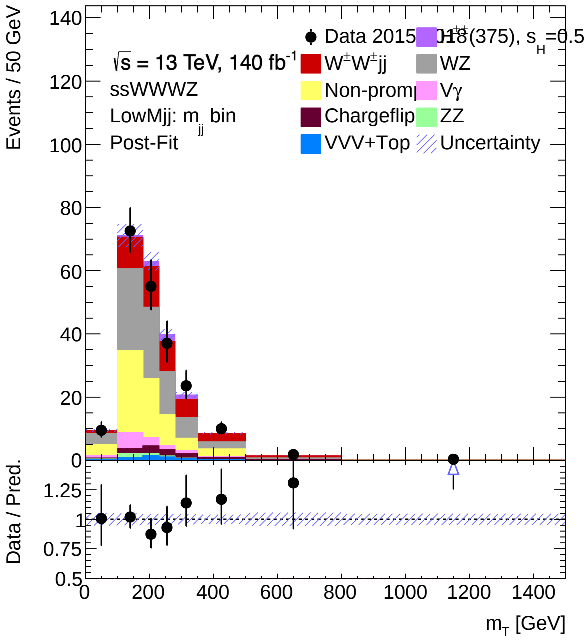

Figure 7.15: Post-fit m_{T} distribution with the combination normalization parameters in the Low-m_{jj} control region used for the signal-extraction fit. The fit is performed using the $H_5^{\pm\pm}$ signal simulations corresponding to the mass point 375 GeV and $\sin\theta_{\mathrm{H}} = 0.5$. The hatched error band represents the total uncertainty of the model.

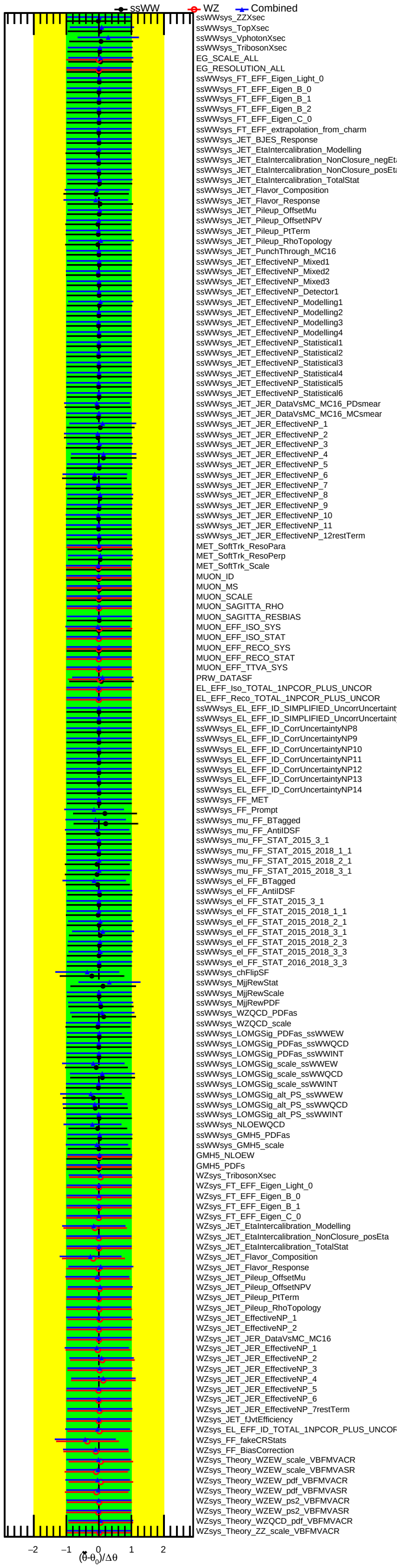

Figure 7.16: Nuisance parameter pulls for the experimental and theoretical components.

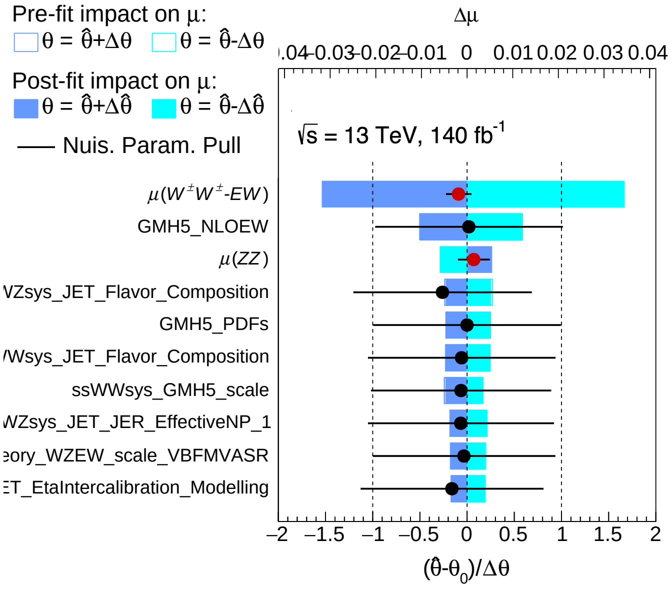

Figure 7.17: Ranking of the systematic nuisance parameters included in the fit according to their impact on the measured signal strength.

7.4 Results

This section presents the statistical results. In HEP, if an observed excess is not statistically significant, an upper limit is set. An upper limit represents the maximum value of a given parameter that is consistent with the observed data, typically at a certain confidence level. The combined results of the upper limits are summarized in Section 7.4.1. Comparisons with previously published results are provided in Section 7.4.2 for ATLAS and Section 7.4.3 for CMS. Some future improvements are discussed in Section 7.5.

7.4.1 Upper limit results with combination

In this section, the limits shown for the independent same-sign WW $H_5^{\pm\pm}$ channel are obtained from the fits performed by keeping the $W^{\pm}Z$ – QCD CR of the same-sign WW analysis. Otherwise comparisons with this separate channel are not meaningful. However, the limits obtained from the combined fits are performed by dropping this $W^{\pm}Z$ – QCD CR, as documented in Section 7.3.3.

Upper limits at 95% CL on the product of the cross-section and branching fraction $\sigma_{\text{VBF}}(H_5^{\pm}) \times \mathcal{B}(H_5^{\pm} \to W^{\pm}Z)$ and $\sigma_{\text{VBF}}(H_5^{\pm\pm}) \times \mathcal{B}(H_5^{\pm\pm} \to W^{\pm}W^{\pm})$ for vector boson fusion production of singly and doubly charged Higgs bosons as a function of m_{H_5} from 200 to 3000 GeV are presented in Figure 7.18a and Figure 7.18b, respectively.

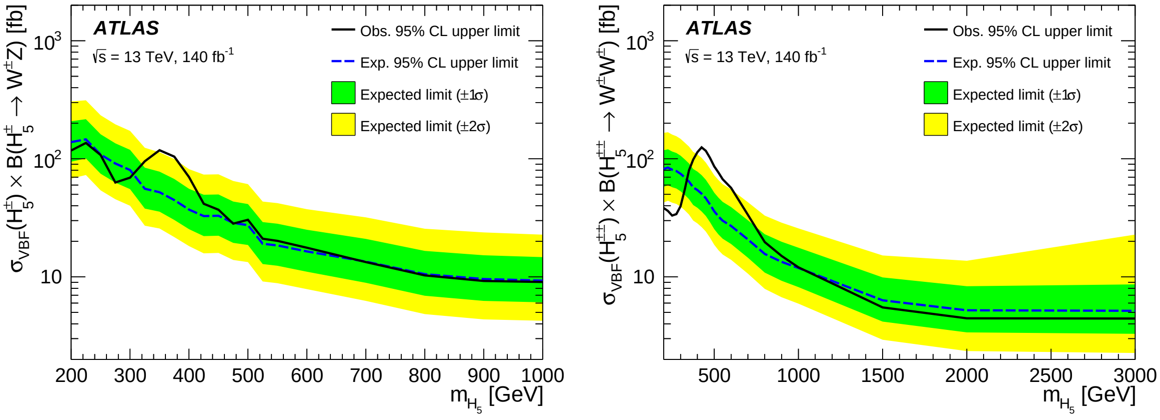

(a) (b)

Figure 7.18: Expected and observed exclusion limits at 95% CL for a $\sigma_{\text{VBF}}(H_5^{\pm}) \times \mathcal{B}(H_5^{\pm} \to W^{\pm}Z)$ and b $\sigma_{\text{VBF}}(H_5^{\pm\pm}) \times \mathcal{B}(H_5^{\pm\pm} \to W^{\pm}W^{\pm})$ as a function of m_{H_5}. The green (yellow) band represents the 68% (95%) confidence interval around the median expected limit.

The corresponding limits on the $\sin\theta_{\text{H}}$ parameter of the GM model as a function of m_{H_5}

are shown in Figure 7.19a for the $H_5^{\pm}$, 7.19b for the $H_5^{\pm\pm}$, and 7.19c for the combination fits. The black hatched region represents the parameter space for which the total width of the H$_5$ exceeds 10% of m_{H_5}, where the model is not applicable due to perturbativity and vacuum stability requirements [74]. For this reason, the limits are provided up to 1500 GeV. The comparison of the best GM exclusion expected limits from the separate $H_5^{\pm}$ or $H_5^{\pm\pm}$ analyses with respect to the combined results yields an improvement in the range $6\% - 22\%$, depending on the mass point.

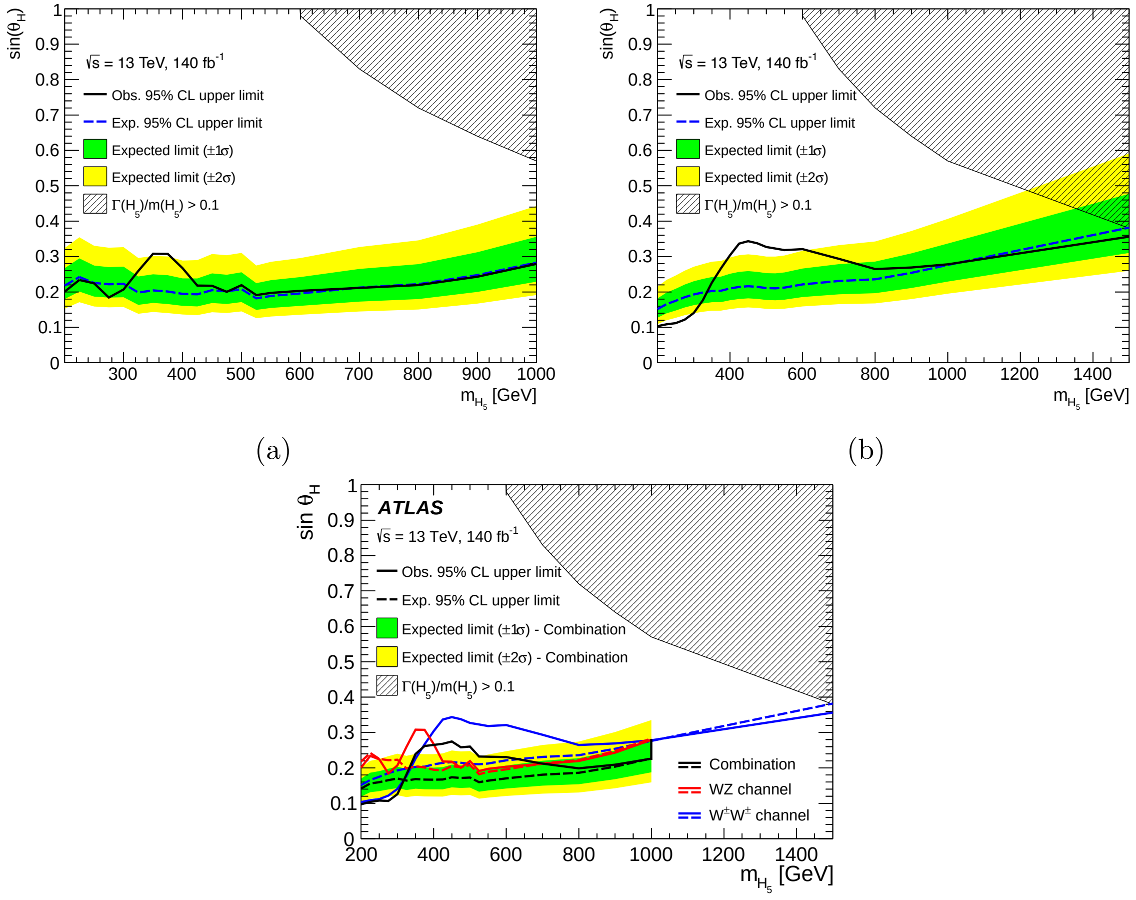

(a) (b)

(c)

Figure 7.19: Expected and observed exclusion limits at 95% CL for $\sin\theta_{\mathrm{H}}$ in the a $H_5^{\pm}$, b $H_5^{\pm\pm}$, and c combination analyses as a function of m_{H_5}. The green (yellow) band is the 68% (95%) confidence interval around the median expected limit. The hatched region covers the parameter space where the intrinsic width of the $H_5^{\pm}$ and $H_5^{\pm\pm}$ bosons would be larger than 10% of the mass and is excluded in the GM model [74].

The observed 95% CL limits exclude $\sin\theta_{\mathrm{H}}$ parameter values greater than $0.10 - 0.36$ for the m_{H_5} between 200 and 1500 GeV. These results show a local excess of events over the SM prediction at a resonance mass of around 400 GeV in Figure 7.19c. The significance of the excess has been evaluated for the different mass points in terms of the local p–value. The excess is largest for the 375 GeV mass point, for which a p–value of 5.7×10^{-4} is obtained, corresponding to a local significance of 3.3 standard deviations. The global significance of the excess was also evaluated [111]; it yields a global p–value of 5.6×10^{-3}, corresponding to a global significance of 2.5 standard deviations. In a similar, though less sensitive, search performed by the CMS Collaboration [112], no significant excess was observed in this mass region with respect to the SM background.

7.4.2 Comparison with the previously published ATLAS measurements

These results have been compared to those published by ATLAS in the independent $H_5^{\pm}$ [79] and $H_5^{\pm\pm}$ [81] searches during Run 2. The comparison of the new $H_5^{\pm}$ and $H_5^{\pm\pm}$ cross-section and GM exclusion limit results with the published ones is shown in Figure 7.20. The improvements in the GM exclusion limits of the $H_5^{\pm\pm}$ channel are driven by the application of higher order NNLO pQCD corrections to the input signal, as described in Section 5.3.1. This feature can be observed in Figure 7.20d. However, the cross-section exclusion limits can be directly compared, and they show a good agreement, with discrepancies below 1.0%, except for the last mass point where they increase up to 17%, as observed in Figure 7.20b. On the other hand, the limits obtained for the individual $H_5^{\pm}$ channel are worse than the published ones. Given the impossibility to obtain the exact inputs or workspace utilized for the published results, the source of the discrepancies remains unclear and we accept the level of agreement of typically $2\% - 5\%$ observed in Figure 7.20a for the cross-section expected exclusion limits as reasonable enough to proceed with the combination of both results. The level of agreement for the GM expected exclusion limits is better by construction, being typically in the range $1\% - 2\%$ as shown in Figure 7.20c.

An additional comparison is performed to illustrate the improvement of the combination GM exclusion limits with respect to the published limits for $H_5^{\pm}$ and $H_5^{\pm\pm}$. The result of this comparison is shown in Figure 7.21. The comparison of the best GM exclusion expected limits from the separate $H_5^{\pm}$ or $H_5^{\pm\pm}$ with respect to the combined results yields an improvement in the range $10\% - 26\%$, depending on the mass point. In this comparison, the $H_5^{\pm}$ prediction

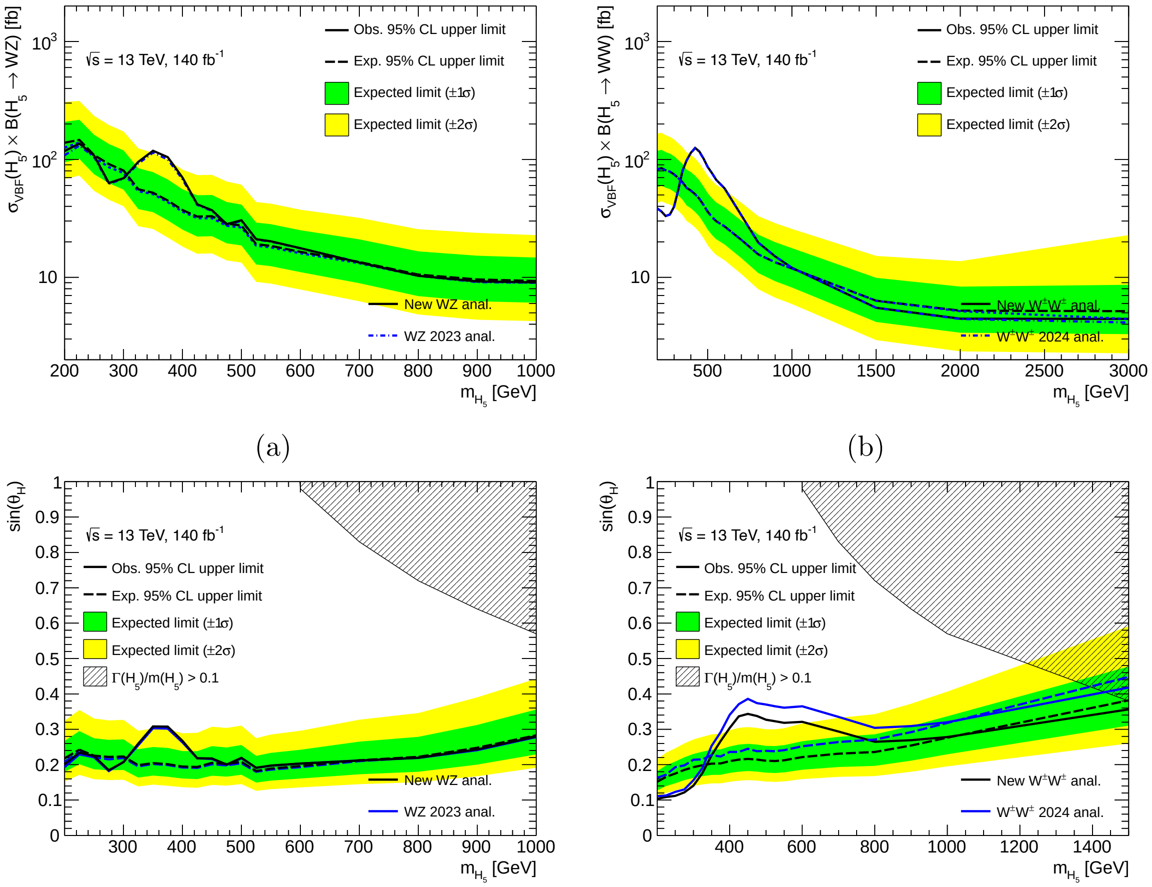

(a) (b)

(c) (d)

Figure 7.20: Expected and observed exclusion limits at 95% CL for a $\sigma_{\text{VBF}}(H_5^{\pm}) \times \mathcal{B}(H_5^{\pm} \to W^{\pm}Z)$ and b $\sigma_{\text{VBF}}(H_5^{\pm\pm}) \times \mathcal{B}(H_5^{\pm\pm} \to W^{\pm}W^{\pm})$ as a function of m_{H_5}. In addition, the expected and observed exclusion limits for $\sin\theta_{\text{H}}$ as a function of m_{H_5} are shown for the $H_5^{\pm}$ c and $H_5^{\pm\pm}$ d analyses. The green (yellow) band represents the 68% (95%) confidence interval around the median expected limit. In all figures, the new results are represented with black lines, compared to the previously published limits, represented in blue and varying the line style to aid for visibility in the cross-section limit plots.

was published at the NNLO order in pQCD, while the $H_5^{\pm\pm}$ was published at LO. This feature explains the big discrepancies between the blue line of Figure 7.21 compared to that of Figure 7.19c.

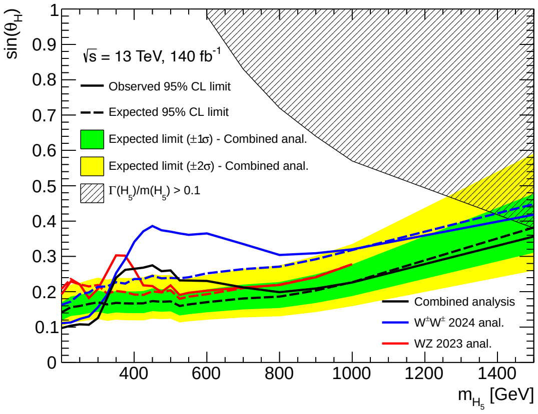

Figure 7.21: Expected and observed exclusion limits at 95% CL for $\sin\theta_{\mathrm{H}}$ in the combination analysis as a function of m_{H_5}. The green (yellow) band is the 68% (95%) confidence interval around the median expected limit. The hatched region covers the parameter space where the intrinsic width of the $H_5^{\pm}$ and $H_5^{\pm\pm}$ bosons would be larger than 10% of the mass and is disfavoured in the GM model [74]. For comparison, the expected and observed exclusion limits reported by the ATLAS Collaboration on Refs. [79, 81] are also included.

7.4.3 Comparison with the CMS full Run 2 results

These results are compared with those published by CMS in their simultaneous $H^{\pm}$ and $H^{\pm\pm}$ fit using the full Run 2 dataset [113]. The expected exclusion limits on the cross-section reported by CMS are compared to the previously published ATLAS limits, showing that the CMS expected limits are approximately 160% − 440% (20% − 70%) less stringent for the WZ (same-sign WW) channel, respectively[9].

The GM exclusion limits on the s_H parameter from the CMS simultaneous fit are compared with those obtained from the ATLAS combination of both channels in Figure 7.22. The comparison reveals that the ATLAS combination yields more stringent expected limits, with improvements ranging from 10% to 50%, depending on the mass point.

The superior sensitivity of the ATLAS combination compared to the CMS analysis can be attributed to two key factors:

---

[9] The values used for this comparison are taken from the HEPData [114] page of the CMS analysis.

1. The use of an ANN in the WZ channel, which provides better discrimination power compared to the conventional cut-based method used in the CMS analysis.

2. The inclusion of an additional WZ-QCD control region in the ATLAS analysis. Unlike the CMS analysis, which relies on a single WZ signal region, the ATLAS approach incorporates both a signal and a dedicated control region. This additional control region enhances the constraint on the WZ background, leading to improved sensitivity in the signal extraction.

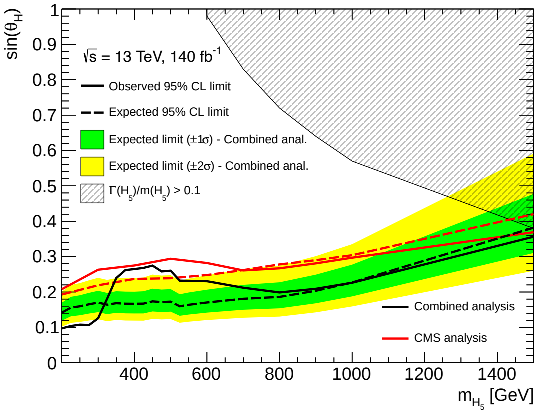

Figure 7.22: Expected and observed exclusion limits at 95% CL for $\sin\theta_{\mathrm{H}}$ in the combination analysis as a function of m_{H_5}. The green (yellow) band is the 68% (95%) confidence interval around the median expected limit. The hatched region covers the parameter space where the intrinsic width of the $H_5^{\pm}$ and $H_5^{\pm\pm}$ bosons would be larger than 10% of the mass and is disfavoured in the GM model [74]. For comparison, the expected and observed exclusion limits reported by the CMS Collaboration on Ref. [113] are also included.

7.5 Summary and Outlook

This chapter presents a combination of results from searches for singly and doubly charged Higgs bosons produced via VBF processes. The analyses focus on the decays into same-sign W bosons and WZ bosons in fully leptonic final states, accompanied by two jets. Using the full Run 2 ATLAS dataset of proton-proton collisions at $\sqrt{s} = 13$ TeV, corresponding to an integrated luminosity of 140 fb^{-1}, the combined results significantly strengthen constraints, surpassing the sensitivities of individual channel analyses.

The results were interpreted within the framework of the Georgi-Machacek model, yielding upper limits at the 95% confidence level on the $\sin\theta_{\mathrm{H}}$ parameter as a function of the five-plet Higgs boson mass, m_{H_5}. Compared to separate analyses of the $H_5^{\pm}$ and $H_5^{\pm\pm}$ channels, the combination improves the expected exclusion limits on the $\sin\theta_{\mathrm{H}}$ parameter by 6% to 22%, depending on the mass point, and excludes $\sin\theta_{\mathrm{H}}$ values greater than 0.10 to 0.36 for m_{H_5} in the range of 200 to 1500 GeV. Upper limits on the VBF production cross-sections $\sigma_{\mathrm{VBF}}(\mathrm{H}_5^{\pm}) \times \mathcal{B}(\mathrm{H}_5^{\pm} \to W^{\pm}Z)$ and $\sigma_{\mathrm{VBF}}(\mathrm{H}_5^{\pm\pm}) \times \mathcal{B}(\mathrm{H}_5^{\pm\pm} \to W^{\pm}W^{\pm})$ were also derived, extending to m_{H_5} masses of up to 3000 GeV. A local excess of events at a resonance mass around 375 GeV was observed, with a global significance of 2.5 standard deviations.

The comparison with previous ATLAS and CMS results demonstrates notable improvements in the exclusion limits on the $\sin\theta_{\mathrm{H}}$ parameter. Specifically, the combined ATLAS results show a $10\% - 26\%$ improvement over the best individual $H_5^{\pm}$ or $H_5^{\pm\pm}$ results and a $10\% - 50\%$ improvement relative to the latest CMS limits.

This study initially emerged as a spin-off from ongoing efforts to extend the search for charged Higgs bosons using the combined datasets from LHC Run 2 and early Run 3. Nevertheless, it demonstrates considerable potential for achieving significant sensitivity improvements in future analyses. These advancements are anticipated to result from increased statistical power and refined analytical techniques. The new combined dataset is expected to correspond to a total integrated luminosity of 250 fb^{-1}, thus the statistical uncertainty will be reduced.

Regarding analytical techniques, one promising direction involves enhanced event selection methods. Preliminary studies in Figure 7.23 suggest that replacing the two-dimensional cut-based method employed in the Run 2 same-sign W boson search [81] with a BDT approach could improve sensitivity by at least 20% in a stat-only fitting scenario. This demonstrates that an optimized tagger could surpass the performance of the 2D fitting strategy, leading to substantial sensitivity gains. Another potential improvement involves utilizing quark/gluon taggers to enhance the identification of quark-initiated jets in VBF events. Recent developments, such as a VBF tagger based on Recurrent Neural Network techniques [115], are expected to further refine event selection. At the object level, advancements including the refinement of the Zee tagger and close-by-isolation corrections could improve the selection efficiency for boosted charged Higgs signals.

Furthermore, a simultaneous search across multiple channels will facilitate a unified design of signal and control regions, along with a consistent treatment of systematic uncertainties, such as those associated with the Jet Energy Scale and Jet Energy Resolution.

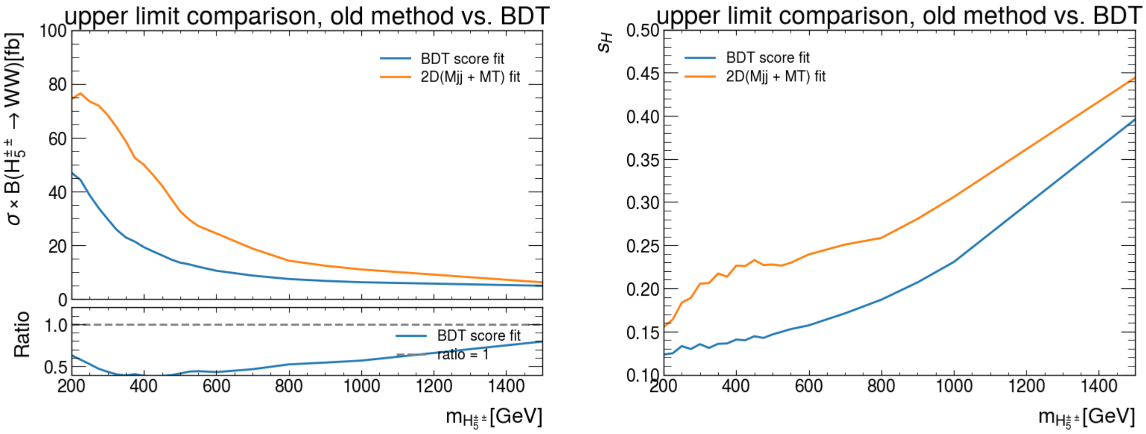

(a) (b)

Figure 7.23: Comparison of the expected limits on the production cross-section 7.23a and $\sin^2\theta_H$ parameter 7.23b for the same-sign WW channel in Run 2. The results are shown for two different fitting methods: the traditional 2D cut-based fitting and the BDT-based approach. The BDT method demonstrates improved sensitivity.

This study serves as a robust foundation for future analyses that aim to enhance the sensitivity to charged Higgs bosons in Run 3 and even the HL-LHC era.

Chapter 8

Conclusions

This thesis provides a comprehensive overview of the Standard Model, with particular focus on the Higgs mechanism and the potential extensions through additional fields to explore new physics. It also includes an overview of the Large Hadron Collider and the ATLAS detector, highlighting its design and upgrade phases. Furthermore, the fundamental experimental techniques, such as object reconstruction, are discussed to set the stage for the subsequent chapters on object performance studies and physics analyses.

Two major contributions form the core of this thesis: combined performance studies of objects and searches for Beyond the Standard Model physics, supplemented by a discussion of computing contributions in the appendix. The first key result involves the development and calibration of a BDT-based quark/gluon jet tagging method. For the first time in ATLAS, the matrix method is employed for the calibration of this ML technique for quark/gluon jets. My contributions includes the development of the BDT tagger, a complete redesign of the analysis framework, and the introduction of multiprocessing capabilities. These improvements significantly enhance calibration efficiency and systematic uncertainty management, leading to the publication of this work as the cover paper of *Chinese Physics C*, Volume 48, Number 2 [116].

The second contribution of this work focuses on the combination of two charged Higgs boson searches with the Vector Boson Fusion signature, achieving the most stringent constraints to date on the parameters of the Georgi–Machacek model. This analysis demonstrates a 10%–26% improvement in sensitivity compared to previous results [117]. My contributions encompass the implementation of statistical procedures, including the definition of fit regions, extraction of fit results, setting of cross-section limits, and conducting rigorous cross-checks to validate histogram inputs and assess systematic uncertainties. These efforts were crutial in ensuring the robustness and reliability of the statistical interpretation. Additionally, I served as one of the Internal Note editors, providing comprehensive documentation of the methodology and analysis steps.

Another set of contributions is detailed in the Appendix. One of these focuses on the optimization of the primary vertex reconstruction algorithm for future detectors (Appendix A). Through this work, I obtained ATLAS authorship. Another contribution (Appendix B) centers on the implementation of track reconstruction using a remote computing server, adopting an "as-a-Service" approach. This innovative method holds significant potential for future applications in both online and offline data processing workflows, particularly in the context of detector upgrades. In this project, I developed the technical programming components, implemented the initial backends to enable the execution of the deep learning model Exa-TrkX [118], and established the foundational infrastructure to support various other models. This work was presented at the Connecting the Dots 2023 workshop [119] and constitutes a key component of an upcoming publication [120].

In conclusion, the work presented in this thesis advances our understanding of SM extensions and improves methodologies in object performance and analysis frameworks. These efforts contribute to the ongoing search for new physics and provide tools and insights for future analyses in High Energy Physics.

Research Contributions

Journal Articles

- **ATLAS Collaboration**, "Combination of searches for singly and doubly charged Higgs bosons produced via vector-boson fusion in proton–proton collisions at $\sqrt{s} = 13$ TeV with the ATLAS detector," *Physics Letters B*, vol. 860, pp. 139137. DOI: 10.1016/j.physletb.2024.139137. [arXiv:2407.10798], 2025.
- **ATLAS Collaboration**, "Performance and calibration of quark/gluon-jet taggers using 140 fb^{-1} of pp collisions at $\sqrt{s} = 13$ TeV with the ATLAS detector," *Chinese Physics C*, vol. 48, no. 2, pp. 023001. DOI: 10.1088/1674-1137/acf701. [arXiv:2308.00716], 2024.
- **H. Zhao et al.**, "Track reconstruction as a service for collider physics," submitted to *JINST*. [arXiv:2501.05520], 2025.

Proceedings and PubNotes

- **H. Zhao et al.**, "AthenaTriton: A Tool for running Machine Learning Inference as a Service in Athena," *CERN Report* [ATL-SOFT-PROC-2025-026], 2025.
- **H. Zhao et al.**, "Graph Neural Network-based Tracking as a Service," *arXiv preprint* [arXiv:2402.09633], 2024.
- **ATLAS Collaboration**, "Expected tracking and related performance with the updated ATLAS Inner Tracker layout at the High-Luminosity LHC," *CERN Report* [ATL-COM-PHYS-2021-377], 2021.

Presentations

- “The ATLAS ITk Tracking and Vertexing performance at the HL-LHC,” *APS April Meeting* (2021) [link].
- “The ATLAS ITk Tracking and Vertexing performance at the HL-LHC,” *LHCC 11th LHC Students Poster Session* (2021) [link].
- “A novel ML-based method of primary vertex reconstruction in high pile-up condition,” *Seattle Snowmass Summer Meeting* (2022) [link].
- “Quark and Gluon Tagging Calibration with the ATLAS detector,” *APS April Meeting* (2022) [link].
- “A novel ML-based method of primary vertex reconstruction in high pile-up condition,” *Fast Machine Learning for Science Workshop*, Southern Methodist University (2022).
- “Developments of ITkPixV1.1 module Quality Control tools,” *CPAD Workshop*, Stony Brook University (2022) [link].
- “Charged Higgs Boson Searches in vector boson fusion processes with the ATLAS detector,” *LHCC* (CERN, 2023) [link].
- “Acts as a Service,” *ACTS Developers Workshop* (2023) [link].
- “Exploring Charged Higgs Bosons in the Georgi-Machacek Model: Latest Findings from the ATLAS Experiment at LHC,” *ICHEP*, Prague (2024) [link].

Appendices

Appendix A

Primary Vertex Reconstruction

A.1 Inner Tracker

The Inner Tracker (ITk) is an all-silicon tracking detector consisting of two subsystems: a Pixel Detector surrounded by a Strip Detector. The Strip Detector has four strip double-module layers in the barrel region and six end-cap disks, covering the pseudorapidity range up to $|\eta|= 2.7$. The Pixel Detector consists of five flat barrel layers and multiple inclined or vertical ring-shaped end-cap disks, extending the coverage up to $|\eta|= 4.0$ [46].

The geometry version of ITk I worked on is 23-00-03. This geometry is used as default for the later study. Recently there are two main changes to the evolution of ITk layout[46]:

- the radius of the innermost pixel layer from 39 to 34 mm
- the pixel pitch in the central part of this layer was fixed to 25×100 μm^2 while a pixel pitch of 50×50 μm^2 is used in the rest of the detector.

A.2 Adaptive Multi-Vertex Finding and Fitting

The vertexing reconstruction algorithm used in Run 2 is Iterative Vertex Finder (IVF)[121]. It was designed for Run 1 and Run 2, where much lower pp interaction multiplicity is expected than Run 3 and HL-LHC Run 4 condition. In this method one track only has one weight in the fits of only one vertex.

The Adaptive Multi Vertex Finder (AMVF) extends the single vertex fitter by allowing tracks to have weight in the fits of more than one nearby vertex. Through deterministic

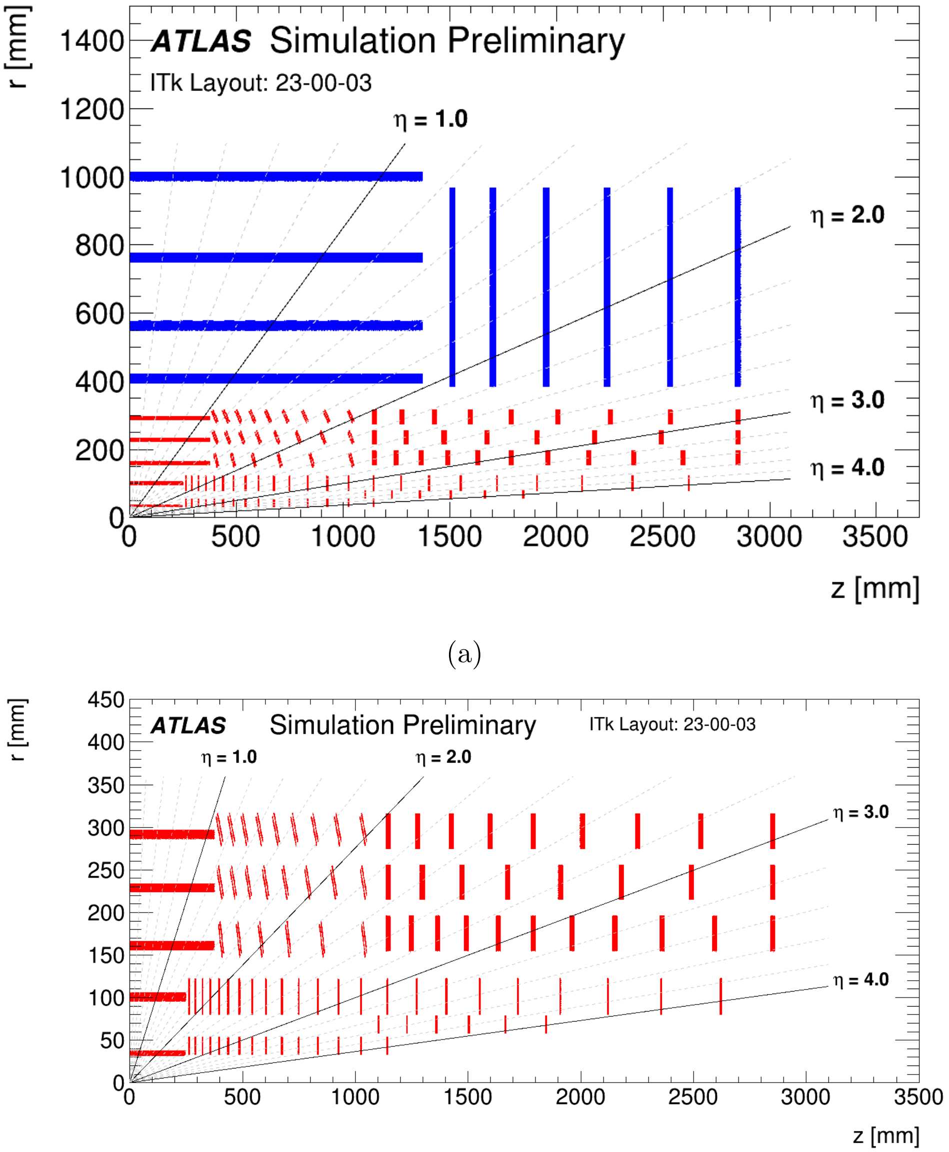

(a)

(b)

Figure A.1: [46] (a) A schematic depiction of the ITk Layout 23-00-03 as presented in this document. (b) A zoomed-in view of the pixel detector. In each case, only one quadrant and only active detector elements are shown. The active elements of the strip detector are shown in blue, and those of the pixel detector are shown in red. The horizontal axis is along the beam line with zero being the nominal interaction point. The vertical axis is the radius measured from the interaction point.

annealing, the weights generally evolve so that each track eventually only has non-negligible weight in a single compatible vertex. During this process, the vertex candidates compete for tracks by adjusting their positions. This technique was developed early in ATLAS but never used in production. It was originally recommissioned for studies of the phase-2 Pixel Detector upgrade, and showed considerable promise. The workflow of AMVF is illustrated in Figure A.2 [47].

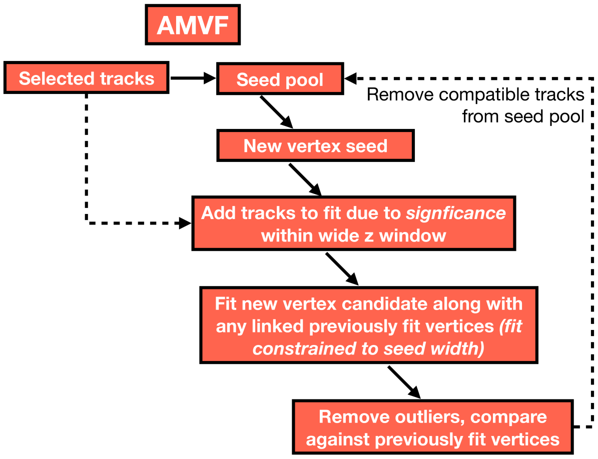

Figure A.2: AMVF workflow [46].

A.3 AMVF Performance for ITk

In this section, we discuss the current AMVF performance on ITk.

The Reconstruction Efficiency is defined as the fraction of events where the reconstructed HS vertex (identified via number of truth HS tracks) is reconstructed within 0.1 mm of the true hard-scatter position in the longitudinal direction. The combined reconstruction and selection efficiency is product of reconstruction and selection efficiency, which means an additional selection criteria the best reconstructed HS vertex identified via $\sum p_T^2$ is the best reconstructed HS vertex identified via number of truth HS tracks.

The following part contributes to the recent ITk PubNote [46]. Figure A.3 illustrate the robust performance of reconstruction efficiency as a function of pile-up density.

Figure A.4a shows the reconstruction and selection efficiency as a function of pile-up density and number of interactions, respectively. A comparison with Run 2 with 38 pile-up is shown. The left plot Figure A.4a shows comparable performance in the pile-up density region of 1 to 2.5.

The right plot Figure A.4b shows the combined reconstruction and selection efficiency as a function of interaction numbers. The trend of IVF algorithm will drop down dramatically in the high dense environment while the AMVF on ITk keeping a slower slope, indicating a robust performance with 200 interactions per bunch crossing.

The longitudinal resolution is pretty good compared to the Run 2 IVF performance. Twice better performance is achieved.

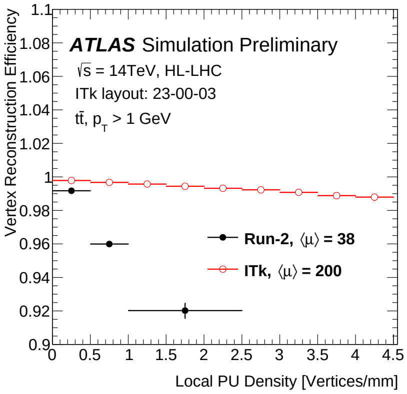

(a)

Figure A.3: Distribution of the local pileup density around the hard-scatter vertex and associated primary vertex reconstruction efficiency For comparison, the performance obtained with the Run 2 Inner Detector with the IVF algorithm and an average pileup of 38 is also shown.[46]

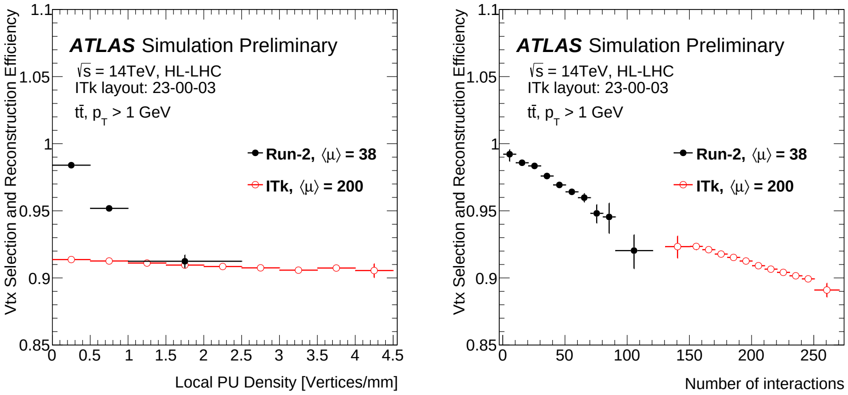

(a) (b)

Figure A.4: Primary vertex combined reconstruction and selection efficiency evaluated in $t\bar{t}$ events with 200 pileup events, obtained with the updated ITk layout and the AMVF algorithm. The efficiency is presented as a function of the local pileup density around the hard-scatter vertex (a) and the number of interactions (b). For comparison, the performance obtained with the Run 2 Inner Detector with the IVF algorithm and an average pileup of 38 is also shown.[46]

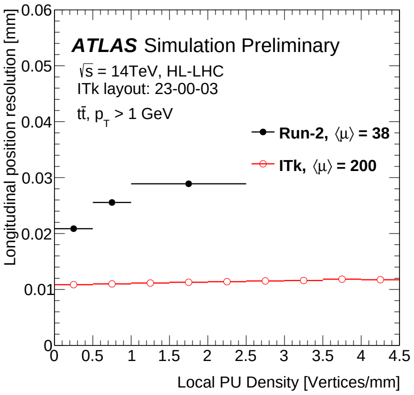

Figure A.5: Longitudinal position resolution of the reconstructed primary vertex, evaluated in $t\bar{t}$ events with 200 pileup events, obtained with the updated ITk layout and the AMVF algorithm. For comparison, the performance obtained with the Run 2 Inner Detector with the IVF algorithm and an average pileup of 38 is also shown.[46]

Appendix B

Tracking As A Service

B.1 Motivation

Among the various event reconstruction algorithms, tracking often dominates the computational resources, consuming approximately 45% of the total processing time [122, 123]. Enhancing the efficiency of this crucial component can significantly improve the overall throughput of the data processing pipeline. This advancement is particularly critical for the timely analysis and interpretation of the extensive datasets produced by the HL-LHC.

B.2 Exa.TrkX as a Service in ACTS

This section describes the implementation of the Exa.TrkX pipeline on a remote Triton™ server. To enable this, the ACTS Common Tracking Software integrates a client-side inference interface that communicates with the Triton Inference Server. The following subsections detail the custom backend integration and associated performance considerations.

B.2.1 Technical Developments in Porting Exa.TrkX as a Service

Standalone Pipeline Before integrating with the Triton backend API, a standalone version of the Exa.TrkX pipeline was developed for local validation. This lightweight implementation includes only the necessary deep learning dependencies and allows comprehensive functional testing prior to deployment on the server. A dedicated class structure was introduced, featuring a configuration-based constructor and functions for model loading and inference execution.

The GPU device ID can be specified through the configuration to ensure that both the model and input data are allocated to the correct GPU. This minimizes data transfer overhead and improves efficiency in multi-GPU environments. The streamlined design of the standalone pipeline simplifies subsequent integration with the Triton server. Once integrated, the server handles input requests and prepares output placeholders, thereby facilitating seamless inference execution.

Backend Lifecycle A clear understanding of the backend lifecycle is essential for effective integration. The backend operates through the following key phases [44]:

- **Initialization Phase:** The server loads model configurations and initializes the model object, which includes the input tensor shape, backend library reference, and model path. The model instance retrieves the designated GPU device ID from the configuration, ensuring that all computations are carried out on the same device as the input data to maximize performance.
- **Execution Phase:** Input data is transferred to GPU memory and processed by model instances. These instances are created based on the `instance_group` settings defined in the model configuration. The server opens specific ports to receive inference requests—typically in the form of 3D spatial coordinates of event spacepoints—via supported protocols such as HTTP or gRPC.
- **Termination Phase:** After inference execution, output responses are generated and transmitted to the client. System resources are then released to ensure efficient memory management and maintain server stability.

B.2.2 Standalone algorithm throughput tests

A standalone version of the Exa.TrkX pipeline is developed to evaluate the performance of the Triton server, focusing on both throughput and latency. The input consists of simulated events generated using the Fatras fast simulation framework [124], which employs Pythia 8 [125] to simulate $t\bar{t}$ MC events with an average pileup of 200 interactions per bunch crossing. This setup approximates the high-occupancy conditions expected at the HL-LHC.

The consistency of output track candidates is verified between local GPU inference and remote inference via the Triton server, ensuring correctness of the pipeline in both configurations. Tests are conducted on the Perlmutter system at the National Energy Research Scientific Computing Center (NERSC), which provides a heterogeneous computing environment.

For local inference tests, the pipeline runs directly on machines with attached GPUs. For remote inference, the Triton server is deployed on a GPU-enabled node, while the client runs on a separate CPU-only node. Communication between the client and server is performed via the gRPC protocol. Performance is benchmarked using Nvidia A100-SXM4 GPUs equipped with 40 GB and 80 GB of memory.

B.2.3 Multiple model instance scaling

To investigate scaling behavior, the pipeline throughput and GPU utilization are measured using Triton's Performance Analyzer. The client performs asynchronous inference requests, allowing it to issue new requests without waiting for previous responses to complete.

As shown in Figure B.1, the maximum throughput on a single GPU is observed to be approximately 1.75 events per second for both GPU memory configurations. Throughput saturation is reached when more than two model instances are deployed and the number of concurrent requests exceeds the number of Triton instances.

The observed increase in throughput with more model instances is attributed to improved GPU utilization, as illustrated in Figure B.2. When multiple Triton instances are active, the GPU hardware is more fully engaged.

Latency measurements indicate that the dominant contributions come from inference computation time and queue wait time. Other sources of latency—such as data transfer between client and server, network transmission, and server-side input/output handling—are found to be negligible. This is expected given the relatively simple and efficient network topology between the nodes.

B.2.4 Multiple GPUs scaling

The inference throughput of a Triton server using one GPU is compared to that using four GPUs. In both configurations, a single Triton instance is used, and all available GPUs are

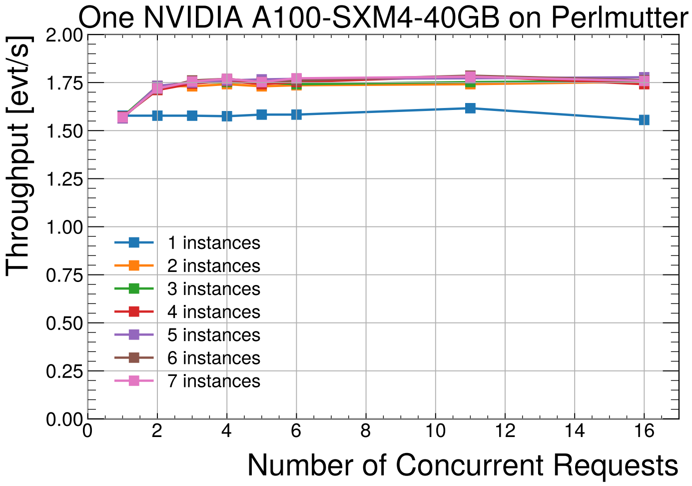

Figure B.1: Throughput of Exa.TrkX inference on an A100-SXM4-40GB GPU as a function of the number of concurrent requests. Each curve corresponds to a fixed number of Triton server instances running on a single GPU. As the number of concurrent requests increases, throughput improves until it saturates at approximately 1.75 events per second. Saturation is achieved when two or more Triton instances are deployed and all receive requests concurrently.

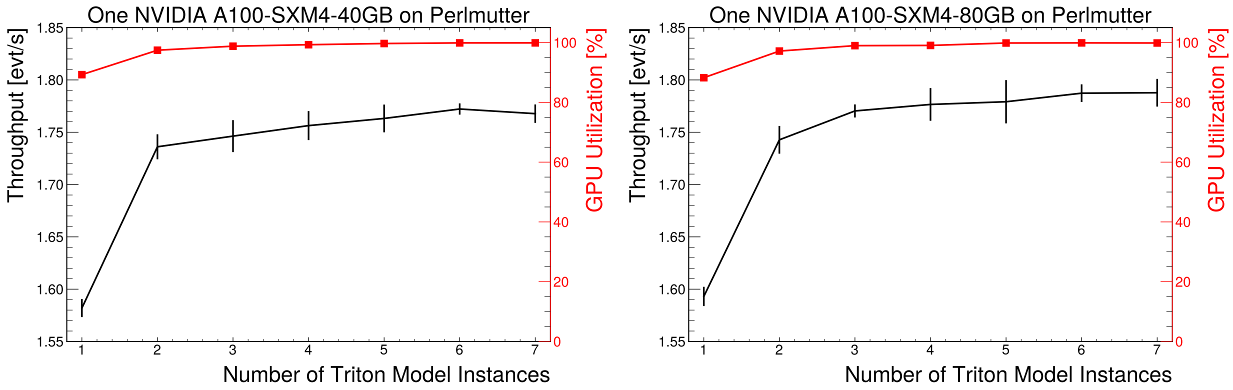

Figure B.2: Maximum throughput and GPU utilization measured on an A100-SXM4-40GB (left) and an A100-SXM4-80GB (right) GPU with 1 to 7 Triton server instances. No significant difference in throughput is observed between the two memory configurations. Each data point represents the average of 10 measurements under saturated conditions, where the number of concurrent requests ranges from matching the number of Triton instances to 10 above saturation. Throughput (black line) and GPU utilization (red line) both plateau when four or more instances are active.

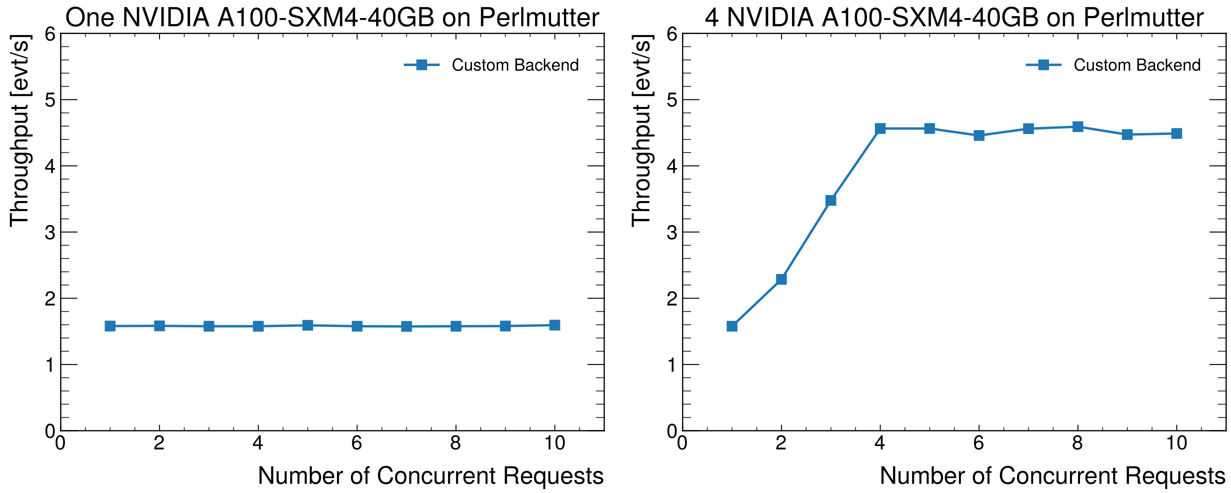

Figure B.3: Inference throughput of a single Triton server instance using one GPU (left) and four GPUs (right). The maximum throughput increases from approximately 1.6 events per second to 4.6 events per second as the number of GPUs increases. The improvement reflects increased parallel capacity, although perfect linear scaling is not achieved.

fully utilized. As shown in Figure B.3, the maximum throughput increases from approximately 1.6 events per second with one GPU to 4.6 events per second with four GPUs. This demonstrates improved parallelization; however, the scaling is sub-linear, indicating potential overheads or resource contention that prevent perfect scaling efficiency.

B.2.5 Integrated Throughput Tests with ACTS

In the ACTS reconstruction workflow, the Exa.TrkX model represents the most computationally intensive component, consuming a substantial fraction of the total processing time. The overall track reconstruction process can be divided into several stages. First, raw measurements from the Pixel and Strip detectors are converted into three-dimensional space points for pattern recognition. This step takes less than eight milliseconds on Perlmutter using an AMD EPYC 7763 CPU. These space points are then passed to the Exa.TrkX model, which identifies collections of proto-track candidates—groups of space points predicted to form tracks. The final stage is track fitting, performed using a Kalman filter.

Three implementations of the Exa.TrkX model are evaluated: direct CPU execution, direct GPU execution, and GPU-based inference served remotely via Triton. In the first two configurations, inference is performed locally on the device without interfacing with the Triton server. The ACTS execution sequence is designed to easily switch between direct and inference-as-a-service (IaaS) modes, offering flexibility for benchmarking and deployment.

The average processing time was measured over ten simulated $t\bar{t}$ events, with results summarized in Table B.1. Under baseline conditions, the CPU implementation—executed on a dedicated CPU node at Perlmutter—accounts for approximately 95% of the total processing time, from raw measurement to track fitting. A significant speedup is achieved when the model runs on a directly connected GPU, reducing inference time to 2.4 seconds. Both the direct GPU and IaaS configurations use an NVIDIA A100 GPU.

Importantly, deploying the Exa.TrkX model via the Triton server introduces no noticeable overhead. The inference time using the remote server is nearly identical to that of direct GPU execution, demonstrating the efficiency and robustness of the Triton-based service implementation. This supports the feasibility of using Triton for high-throughput track reconstruction under HL-LHC conditions.

The IaaS inference tests were conducted with both the client and server located at Perlmutter, where network latency is negligible. This setup reflects potential application in a High-Level Trigger (HLT) environment, where a nearby GPU cluster can minimize communication overhead. Alternatively, scenarios involving geographically remote GPU farms—such as the National Research Platform at UCSD—could be considered. In such cases, additional latency is expected and depends on the distance between the client and inference server. For example, the estimated network latency over a direct distance of approximately 730 km is around 1.1 s.

Implementation	Exa.TrkX Inference Time (s)
Direct CPU	9.65
Direct GPU	2.42
IaaS GPU	2.24

Table B.1: Average inference time for the Exa.TrkX model under different configurations [120].

Appendix C

Charged Higgs

C.1 Statistical-only fits results

A cross-check was performed to study the impact of the systematic uncertainties in the limits results. This cross-check was done by repeating the profile-likelihood fits for each of the signal mass points and comparing the exclusion limits with the nominal ones. This exercise is performed for the $H_5^{\pm}$, $H_5^{\pm\pm}$, and combination fits separately. The absolute relative difference obtained for the 95% CL expected exclusion limits for $\sin\theta_{\mathrm{H}}$ is shown in Figure C.1.

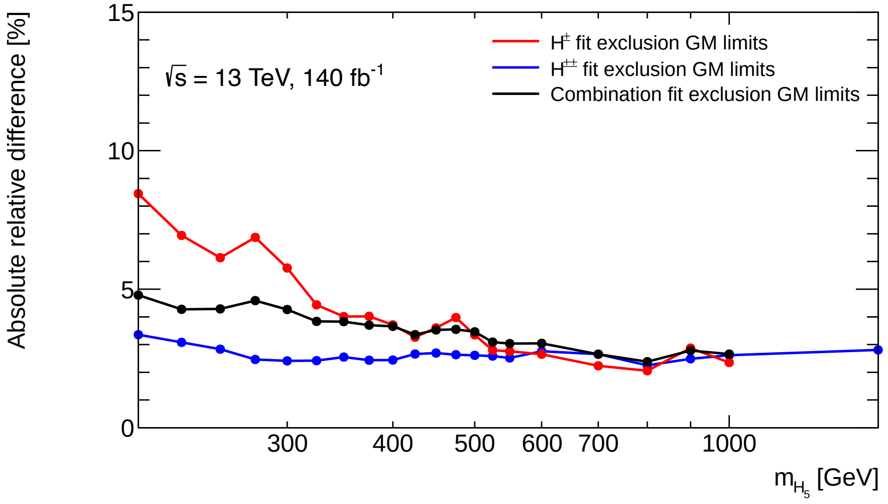

Figure C.1: Absolute relative difference between the nominal 95% CL expected exclusion limits for $\sin\theta_{\mathrm{H}}$ obtained in the $H_5^{\pm}$ (red), $H_5^{\pm\pm}$ (blue), and combination (black) fits and the ones obtained in a scenario where only the data statistical uncertainties are considered. The results are presented as a function of m_{H_5}.

C.2 Systematic uncertainties treatment

In this Appendix, the treatment applied to the different systematic uncertainties propagated in the fit is discussed. Specifically, the smoothing and symmetrization treatment applied is made explicit for all the systematic uncertainties entering the $H_5^{\pm}$ and $H_5^{\pm\pm}$ fits described in Section 7.3. The same treatment applied in the two original searches [79, 81] is followed in this analysis. The $H_5^{\pm}$ fit uncertainties are displayed in Table C.1, and the ones corresponding to the $H_5^{\pm\pm}$ fit are provided in Tables C.2 and C.3.

Table C.1: List of systematic uncertainties propagated through the $H_5^{\pm}$ fit. The information on the input type, smoothing, symmetrization, and normalization treatment is provided for each nuisance parameter.

Number	Uncertainty name	TRExFitter Type	Smoothing	Symmetrization	Drop normalization
1	Luminosity	“OVERALL”	No	No	No
2	EG_RESOLUTION_ALL	“HISTO”	“40”	“TWOSIDED”	No
3	EG_SCALE_ALL	“HISTO”	“40”	“TWOSIDED”	No
4	FT_EFF_Eigen_Light_0	“HISTO”	“40”	“TWOSIDED”	No
5	FT_EFF_Eigen_Light_1	“HISTO”	“40”	“TWOSIDED”	No
6	FT_EFF_Eigen_Light_2	“HISTO”	“40”	“TWOSIDED”	No
7	FT_EFF_Eigen_Light_3	“HISTO”	“40”	“TWOSIDED”	No
8	FT_EFF_Eigen_B_0	“HISTO”	“40”	“TWOSIDED”	No
9	FT_EFF_Eigen_B_1	“HISTO”	“40”	“TWOSIDED”	No
10	FT_EFF_Eigen_B_2	“HISTO”	“40”	“TWOSIDED”	No
11	FT_EFF_Eigen_B_3	“HISTO”	“40”	“TWOSIDED”	No
12	FT_EFF_Eigen_B_4	“HISTO”	“40”	“TWOSIDED”	No
13	FT_EFF_Eigen_B_5	“HISTO”	“40”	“TWOSIDED”	No
14	FT_EFF_Eigen_B_6	“HISTO”	“40”	“TWOSIDED”	No
15	FT_EFF_Eigen_B_7	“HISTO”	“40”	“TWOSIDED”	No
16	FT_EFF_Eigen_B_8	“HISTO”	“40”	“TWOSIDED”	No
17	FT_EFF_Eigen_C_0	“HISTO”	“40”	“TWOSIDED”	No
18	FT_EFF_Eigen_C_1	“HISTO”	“40”	“TWOSIDED”	No
19	FT_EFF_Eigen_C_2	“HISTO”	“40”	“TWOSIDED”	No
20	FT_EFF_Eigen_C_3	“HISTO”	“40”	“TWOSIDED”	No
21	FT_EFF_extrapolation	“HISTO”	“40”	“TWOSIDED”	No
22	FT_EFF_extrapolation_from_charm	“HISTO”	“40”	“TWOSIDED”	No
23	JET_BJES_Response	“HISTO”	“40”	“TWOSIDED”	No
24	JET_EffectiveNP_1	“HISTO”	“40”	“TWOSIDED”	No
25	JET_EffectiveNP_2	“HISTO”	“40”	“TWOSIDED”	No
26	JET_EffectiveNP_3	“HISTO”	“40”	“TWOSIDED”	No
27	JET_EffectiveNP_4	“HISTO”	“40”	“TWOSIDED”	No
28	JET_EffectiveNP_5	“HISTO”	“40”	“TWOSIDED”	No
29	JET_EffectiveNP_6	“HISTO”	“40”	“TWOSIDED”	No
30	JET_EffectiveNP_7	“HISTO”	“40”	“TWOSIDED”	No
31	JET_EffectiveNP_8restTerm	“HISTO”	“40”	“TWOSIDED”	No
32	JET_EtaIntercalibration_Modelling	“HISTO”	“40”	“TWOSIDED”	No
33	JET_EtaIntercalibration_NonClosure_2018data	“HISTO”	“40”	“TWOSIDED”	No
34	JET_EtaIntercalibration_NonClosure_highE	“HISTO”	“40”	“TWOSIDED”	No
35	JET_EtaIntercalibration_NonClosure_negEta	“HISTO”	“40”	“TWOSIDED”	No
36	JET_EtaIntercalibration_NonClosure_posEta	“HISTO”	“40”	“TWOSIDED”	No
37	JET_EtaIntercalibration_TotalStat	“HISTO”	“40”	“TWOSIDED”	No
38	JET_Flavor_Composition	“HISTO”	“40”	“TWOSIDED”	No
39	JET_Flavor_Response	“HISTO”	“40”	“TWOSIDED”	No
40	JET_Pileup_OffsetMu	“HISTO”	“40”	“TWOSIDED”	No
41	JET_Pileup_OffsetNPV	“HISTO”	“40”	“TWOSIDED”	No
42	JET_Pileup_PtTerm	“HISTO”	“40”	“TWOSIDED”	No
43	JET_Pileup_RhoTopology	“HISTO”	“40”	“TWOSIDED”	No
44	JET_PunchThrough_MC16	“HISTO”	“40”	“TWOSIDED”	No
45	JET_SingleParticle_HighPt	“HISTO”	“40”	“TWOSIDED”	No
46	JET_JER_DataVsMC_MC16	“HISTO”	“40”	“ONESIDED”	No
47	JET_JER_EffectiveNP_1	“HISTO”	“40”	“ONESIDED”	No
48	JET_JER_EffectiveNP_2	“HISTO”	“40”	“ONESIDED”	No
49	JET_JER_EffectiveNP_3	“HISTO”	“40”	“ONESIDED”	No
50	JET_JER_EffectiveNP_4	“HISTO”	“40”	“ONESIDED”	No
51	JET_JER_EffectiveNP_5	“HISTO”	“40”	“ONESIDED”	No
52	JET_JER_EffectiveNP_6	“HISTO”	“40”	“ONESIDED”	No
53	JET_JER_EffectiveNP_7restTerm	“HISTO”	“40”	“ONESIDED”	No
54	JET_JvtEfficiency	“HISTO”	“40”	“TWOSIDED”	No
55	JET_fJvtEfficiency	“HISTO”	“40”	“TWOSIDED”	No
56	MET_SoftTrk_ResoPara	“HISTO”	“40”	“TWOSIDED”	No
57	MET_SoftTrk_ResoPerp	“HISTO”	“40”	“TWOSIDED”	No
58	MET_SoftTrk_Scale	“HISTO”	“40”	“TWOSIDED”	No
59	MUON_EFF_ISO_STAT	“HISTO”	“40”	“TWOSIDED”	No
60	MUON_EFF_ISO_SYS	“HISTO”	“40”	“TWOSIDED”	No
61	MUON_EFF_RECO_STAT	“HISTO”	“40”	“TWOSIDED”	No
62	MUON_EFF_RECO_STAT_LOWPT	“HISTO”	“40”	“TWOSIDED”	No
63	MUON_EFF_RECO_SYS	“HISTO”	“40”	“TWOSIDED”	No
64	MUON_EFF_RECO_SYS_LOWPT	“HISTO”	“40”	“TWOSIDED”	No
65	MUON_EFF_TTVA_STAT	“HISTO”	“40”	“TWOSIDED”	No
66	MUON_EFF_TTVA_SYS	“HISTO”	“40”	“TWOSIDED”	No
67	MUON_ID	“HISTO”	“40”	“TWOSIDED”	No
68	MUON_MS	“HISTO”	“40”	“TWOSIDED”	No
69	MUON_SAGITTA_RESBIAS	“HISTO”	“40”	“TWOSIDED”	No
70	MUON_SAGITTA_RHO	“HISTO”	“40”	“ONESIDED”	No
71	MUON_SCALE	“HISTO”	“40”	“TWOSIDED”	No
72	PRW_DATASF	“HISTO”	“40”	No	No
73	EL_EFF_ID_TOTAL_1NPCOR_PLUS_UNCOR	“HISTO”	“40”	“TWOSIDED”	No
74	EL_EFF_Iso_TOTAL_1NPCOR_PLUS_UNCOR	“HISTO”	“40”	“TWOSIDED”	No
75	EL_EFF_Reco_TOTAL_1NPCOR_PLUS_UNCOR	“HISTO”	“40”	“TWOSIDED”	No
76	FF_fakeCRStats	“HISTO”	“40”	“TWOSIDED”	No
77	FF_BiasCorrection	“HISTO”	“40”	“ONESIDED”	No
78	Theory_WZEW_scale_VBFMVACR	“HISTO”	“40”	“TWOSIDED”	No
79	Theory_WZEW_scale_VBFMVASR	“HISTO”	“40”	“TWOSIDED”	No
80	Theory_WZEW_pdf_VBFMVACR	“HISTO”	“40”	“TWOSIDED”	No
81	Theory_WZEW_pdf_VBFMVASR	“HISTO”	“40”	“TWOSIDED”	No
82	Theory_WZEW_ps2_VBFMVACR	“HISTO”	“40”	“TWOSIDED”	No
83	Theory_WZEW_ps2_VBFMVASR	“HISTO”	“40”	“TWOSIDED”	No
84	Theory_WZQCD_scale_VBFMVACR	“HISTO”	“40”	“TWOSIDED”	Yes
85	Theory_WZQCD_scale_VBFMVASR	“HISTO”	“40”	“TWOSIDED”	Yes
86	Theory_WZQCD_pdf_VBFMVACR	“HISTO”	“40”	“TWOSIDED”	Yes
87	Theory_WZQCD_pdf_VBFMVASR	“HISTO”	“40”	“TWOSIDED”	Yes
88	Theory_WZQCD_ps2_VBFMVACR	“HISTO”	“40”	“TWOSIDED”	Yes
89	Theory_WZQCD_ps2_VBFMVASR	“HISTO”	“40”	“TWOSIDED”	Yes
90	Theory_ZZ_scale_VBFMVACR	“HISTO”	“40”	“TWOSIDED”	Yes
91	Theory_ZZ_scale_VBFMVASR	“HISTO”	“40”	“TWOSIDED”	Yes
92	Theory_ZZ_pdf_VBFMVACR	“HISTO”	“40”	“TWOSIDED”	Yes
92	Theory_ZZ_pdf_VBFMVASR	“HISTO”	“40”	“TWOSIDED”	Yes
93	GMH5_NNLO_PDFs	“OVERALL”	No	No	No
94	GMH5_NNLO_ALPHAs	“OVERALL”	No	No	No
95	GMH5_NNLO_scale	“OVERALL”	No	No	No
96	GMH5_NLOEW	“OVERALL”	No	No	No
97	TribosonXsec	“OVERALL”	No	No	No

Table C.2: List of systematic uncertainties propagated through the $H_5^{\pm\pm}$ fit. The information on the input type, smoothing, symmetrization, and normalization treatment is provided for each nuisance parameter.

Number	Uncertainty name	TRExFitter Type	Smoothing	Symmetrization	Drop normalization
1	Luminosity	“OVERALL”	No	No	No
2	EG_SCALE_ALL	“HISTO”	“40”	“TWOSIDED”	No
3	EG_RESOLUTION_ALL	“HISTO”	“40”	“TWOSIDED”	No
4	FT_EFF_Eigen_Light_0	“HISTO”	“40”	“TWOSIDED”	No
5	FT_EFF_Eigen_Light_1	“HISTO”	“40”	“TWOSIDED”	No
6	FT_EFF_Eigen_Light_2	“HISTO”	“40”	“TWOSIDED”	No
7	FT_EFF_Eigen_Light_3	“HISTO”	“40”	“TWOSIDED”	No
8	FT_EFF_Eigen_B_0	“HISTO”	“40”	“TWOSIDED”	No
9	FT_EFF_Eigen_B_1	“HISTO”	“40”	“TWOSIDED”	No
10	FT_EFF_Eigen_B_2	“HISTO”	“40”	“TWOSIDED”	No
11	FT_EFF_Eigen_C_0	“HISTO”	“40”	“TWOSIDED”	No
12	FT_EFF_Eigen_C_1	“HISTO”	“40”	“TWOSIDED”	No
13	FT_EFF_Eigen_C_2	“HISTO”	“40”	“TWOSIDED”	No
14	FT_EFF_extrapolation	“HISTO”	“40”	“TWOSIDED”	No
15	FT_EFF_extrapolation_from_charm	“HISTO”	“40”	“TWOSIDED”	No
16	JET_PunchThrough_MC16	“HISTO”	“40”	“TWOSIDED”	No
17	JET_Flavor_Composition	“HISTO”	“40”	“TWOSIDED”	No
18	JET_Flavor_Response	“HISTO”	“40”	“TWOSIDED”	No
19	JET_Pileup_RhoTopology	“HISTO”	“40”	“TWOSIDED”	No
20	JET_Pileup_OffsetMu	“HISTO”	“40”	“TWOSIDED”	No
21	JET_Pileup_OffsetNPV	“HISTO”	“40”	“TWOSIDED”	No
22	JET_Pileup_PtTerm	“HISTO”	“40”	“TWOSIDED”	No
23	JET_BJES_Response	“HISTO”	“40”	“TWOSIDED”	No
24	JET_EtaIntercalibration_Modelling	“HISTO”	“40”	“TWOSIDED”	No
25	JET_EtaIntercalibration_NonClosure_posEta	“HISTO”	“40”	“TWOSIDED”	No
26	JET_EtaIntercalibration_NonClosure_negEta	“HISTO”	“40”	“TWOSIDED”	No
27	JET_EtaIntercalibration_NonClosure_highE	“HISTO”	“40”	“TWOSIDED”	No
28	JET_EtaIntercalibration_TotalStat	“HISTO”	“40”	“TWOSIDED”	No
29	JET_EffectiveNP_Mixed1	“HISTO”	“40”	“TWOSIDED”	No
30	JET_EffectiveNP_Mixed2	“HISTO”	“40”	“TWOSIDED”	No
31	JET_EffectiveNP_Mixed3	“HISTO”	“40”	“TWOSIDED”	No
32	JET_EffectiveNP_Detector1	“HISTO”	“40”	“TWOSIDED”	No
33	JET_EffectiveNP_Detector2	“HISTO”	“40”	“TWOSIDED”	No
34	JET_EffectiveNP_Modelling1	“HISTO”	“40”	“TWOSIDED”	No
35	JET_EffectiveNP_Modelling2	“HISTO”	“40”	“TWOSIDED”	No
36	JET_EffectiveNP_Modelling3	“HISTO”	“40”	“TWOSIDED”	No
37	JET_EffectiveNP_Modelling4	“HISTO”	“40”	“TWOSIDED”	No
38	JET_EffectiveNP_Statistical1	“HISTO”	“40”	“TWOSIDED”	No
39	JET_EffectiveNP_Statistical2	“HISTO”	“40”	“TWOSIDED”	No
40	JET_EffectiveNP_Statistical3	“HISTO”	“40”	“TWOSIDED”	No
41	JET_EffectiveNP_Statistical4	“HISTO”	“40”	“TWOSIDED”	No
42	JET_EffectiveNP_Statistical5	“HISTO”	“40”	“TWOSIDED”	No
43	JET_EffectiveNP_Statistical6	“HISTO”	“40”	“TWOSIDED”	No
44	JET_SingleParticle_HighPt	“HISTO”	“40”	“TWOSIDED”	No
45	JET_JER_DataVsMC_MC16_PDsmear	“HISTO”	“40”	“TWOSIDED”	No
46	JET_JER_DataVsMC_MC16_MCsmear	“HISTO”	“40”	“TWOSIDED”	No
47	JET_JER_EffectiveNP_1	“HISTO”	“40”	“TWOSIDED”	No
48	JET_JER_EffectiveNP_2	“HISTO”	“40”	“TWOSIDED”	No
49	JET_JER_EffectiveNP_3	“HISTO”	“40”	“TWOSIDED”	No
50	JET_JER_EffectiveNP_4	“HISTO”	“40”	“TWOSIDED”	No
51	JET_JER_EffectiveNP_5	“HISTO”	“40”	“TWOSIDED”	No
52	JET_JER_EffectiveNP_6	“HISTO”	“40”	“TWOSIDED”	No
53	JET_JER_EffectiveNP_7	“HISTO”	“40”	“TWOSIDED”	No
54	JET_JER_EffectiveNP_8	“HISTO”	“40”	“TWOSIDED”	No
55	JET_JER_EffectiveNP_9	“HISTO”	“40”	“TWOSIDED”	No
56	JET_JER_EffectiveNP_10	“HISTO”	“40”	“TWOSIDED”	No
57	JET_JER_EffectiveNP_11	“HISTO”	“40”	“TWOSIDED”	No
58	JET_JER_EffectiveNP_12restTerm	“HISTO”	“40”	“TWOSIDED”	No
59	JET_JvtEfficiency	“HISTO”	“40”	“TWOSIDED”	No
60	MET_JetTrk_Scale	“HISTO”	“40”	“TWOSIDED”	No
61	MET_SoftTrk_Scale	“HISTO”	“40”	“TWOSIDED”	No
62	MET_SoftTrk_ResoPerp	“HISTO”	“40”	“ONESIDED”	No
63	MET_SoftTrk_ResoPara	“HISTO”	“40”	“ONESIDED”	No
64	MUON_ID	“HISTO”	“40”	“TWOSIDED”	No
65	MUON_MS	“HISTO”	“40”	“TWOSIDED”	No
66	MUON_SCALE	“HISTO”	“40”	“TWOSIDED”	No
67	MUON_SAGITTA_RHO	“HISTO”	“40”	“TWOSIDED”	No
68	MUON_SAGITTA_RESBIAS	“HISTO”	“40”	“TWOSIDED”	No
69	MUON_EFF_ISO_SYS	“HISTO”	“40”	“TWOSIDED”	No
70	MUON_EFF_ISO_STAT	“HISTO”	“40”	“TWOSIDED”	No
71	MUON_EFF_RECO_SYS	“HISTO”	“40”	“TWOSIDED”	No
72	MUON_EFF_RECO_SYS_LOWPT	“HISTO”	“40”	“TWOSIDED”	No
73	MUON_EFF_RECO_STAT	“HISTO”	“40”	“TWOSIDED”	No
74	MUON_EFF_RECO_STAT_LOWPT	“HISTO”	“40”	“TWOSIDED”	No
75	MUON_EFF_TrigSystUncertainty	“HISTO”	“40”	“TWOSIDED”	No
76	MUON_EFF_TrigStatUncertainty	“HISTO”	“40”	“TWOSIDED”	No
77	MUON_EFF_TTVA_SYS	“HISTO”	“40”	“TWOSIDED”	No
78	MUON_EFF_TTVA_STAT	“HISTO”	“40”	“TWOSIDED”	No
79	PRW_DATASF	“HISTO”	“40”	“TWOSIDED”	No
80	EL_EFF_Trigger_TOTAL_1NPCOR_PLUS_UNCOR	“HISTO”	“40”	“TWOSIDED”	No
81	EL_EFF_TriggerEff_TOTAL_1NPCOR_PLUS_UNCOR	“HISTO”	“40”	“TWOSIDED”	No
82	EL_EFF_Iso_TOTAL_1NPCOR_PLUS_UNCOR	“HISTO”	“40”	“TWOSIDED”	No
83	EL_EFF_Reco_TOTAL_1NPCOR_PLUS_UNCOR	“HISTO”	“40”	“TWOSIDED”	No
84	EL_EFF_ID_SIMPLIFIED_UncorrUncertaintyNP0	“HISTO”	“40”	“TWOSIDED”	No
85	EL_EFF_ID_SIMPLIFIED_UncorrUncertaintyNP1	“HISTO”	“40”	“TWOSIDED”	No
86	EL_EFF_ID_SIMPLIFIED_UncorrUncertaintyNP2	“HISTO”	“40”	“TWOSIDED”	No
87	EL_EFF_ID_SIMPLIFIED_UncorrUncertaintyNP3	“HISTO”	“40”	“TWOSIDED”	No
88	EL_EFF_ID_SIMPLIFIED_UncorrUncertaintyNP4	“HISTO”	“40”	“TWOSIDED”	No
89	EL_EFF_ID_SIMPLIFIED_UncorrUncertaintyNP5	“HISTO”	“40”	“TWOSIDED”	No
90	EL_EFF_ID_SIMPLIFIED_UncorrUncertaintyNP6	“HISTO”	“40”	“TWOSIDED”	No
91	EL_EFF_ID_SIMPLIFIED_UncorrUncertaintyNP7	“HISTO”	“40”	“TWOSIDED”	No
92	EL_EFF_ID_SIMPLIFIED_UncorrUncertaintyNP8	“HISTO”	“40”	“TWOSIDED”	No

Table C.3: List of systematic uncertainties propagated through the $H_5^{\pm\pm}$ fit. The information on the input type, smoothing, symmetrization, and normalization treatment is provided for each nuisance parameter.

Number	**Uncertainty name**	**TRExFitter Type**	**Smoothing**	**Symmetrization**	**Drop normalization**
93	EL_EFF_ID_SIMPLIFIED_UncorrUncertaintyNP9	"HISTO"	"40"	"TWOSIDED"	No
94	EL_EFF_ID_SIMPLIFIED_UncorrUncertaintyNP10	"HISTO"	"40"	"TWOSIDED"	No
95	EL_EFF_ID_SIMPLIFIED_UncorrUncertaintyNP11	"HISTO"	"40"	"TWOSIDED"	No
96	EL_EFF_ID_SIMPLIFIED_UncorrUncertaintyNP12	"HISTO"	"40"	"TWOSIDED"	No
97	EL_EFF_ID_SIMPLIFIED_UncorrUncertaintyNP13	"HISTO"	"40"	"TWOSIDED"	No
98	EL_EFF_ID_SIMPLIFIED_UncorrUncertaintyNP14	"HISTO"	"40"	"TWOSIDED"	No
99	EL_EFF_ID_SIMPLIFIED_UncorrUncertaintyNP15	"HISTO"	"40"	"TWOSIDED"	No
100	EL_EFF_ID_SIMPLIFIED_UncorrUncertaintyNP16	"HISTO"	"40"	"TWOSIDED"	No
101	EL_EFF_ID_SIMPLIFIED_UncorrUncertaintyNP17	"HISTO"	"40"	"TWOSIDED"	No
102	EL_EFF_ID_CorrUncertaintyNP0	"HISTO"	"40"	"TWOSIDED"	No
103	EL_EFF_ID_CorrUncertaintyNP1	"HISTO"	"40"	"TWOSIDED"	No
104	EL_EFF_ID_CorrUncertaintyNP2	"HISTO"	"40"	"TWOSIDED"	No
105	EL_EFF_ID_CorrUncertaintyNP3	"HISTO"	"40"	"TWOSIDED"	No
106	EL_EFF_ID_CorrUncertaintyNP4	"HISTO"	"40"	"TWOSIDED"	No
107	EL_EFF_ID_CorrUncertaintyNP5	"HISTO"	"40"	"TWOSIDED"	No
108	EL_EFF_ID_CorrUncertaintyNP6	"HISTO"	"40"	"TWOSIDED"	No
109	EL_EFF_ID_CorrUncertaintyNP7	"HISTO"	"40"	"TWOSIDED"	No
110	EL_EFF_ID_CorrUncertaintyNP8	"HISTO"	"40"	"TWOSIDED"	No
111	EL_EFF_ID_CorrUncertaintyNP9	"HISTO"	"40"	"TWOSIDED"	No
112	EL_EFF_ID_CorrUncertaintyNP10	"HISTO"	"40"	"TWOSIDED"	No
113	EL_EFF_ID_CorrUncertaintyNP11	"HISTO"	"40"	"TWOSIDED"	No
114	EL_EFF_ID_CorrUncertaintyNP12	"HISTO"	"40"	"TWOSIDED"	No
115	EL_EFF_ID_CorrUncertaintyNP13	"HISTO"	"40"	"TWOSIDED"	No
116	EL_EFF_ID_CorrUncertaintyNP14	"HISTO"	"40"	"TWOSIDED"	No
117	EL_EFF_ID_CorrUncertaintyNP15	"HISTO"	"40"	"TWOSIDED"	No
118	FF_MET	"HISTO"	"40"	"TWOSIDED"	No
119	FF_Prompt	"HISTO"	"40"	"TWOSIDED"	No
120	mu_FF_BTagged	"HISTO"	"40"	"TWOSIDED"	No
121	mu_FF_AntiIDSF	"HISTO"	"40"	"TWOSIDED"	No
122	mu_FF_STAT_2015_1_1	"HISTO"	"40"	"TWOSIDED"	No
123	mu_FF_STAT_2015_2_1	"HISTO"	"40"	"TWOSIDED"	No
124	mu_FF_STAT_2015_3_1	"HISTO"	"40"	"TWOSIDED"	No
125	mu_FF_STAT_2015_2018_1_1	"HISTO"	"40"	"TWOSIDED"	No
126	mu_FF_STAT_2015_2018_2_1	"HISTO"	"40"	"TWOSIDED"	No
127	mu_FF_STAT_2015_2018_3_1	"HISTO"	"40"	"TWOSIDED"	No
128	mu_FF_STAT_2016_2018_1_1	"HISTO"	"40"	"TWOSIDED"	No
129	mu_FF_STAT_2016_2018_2_1	"HISTO"	"40"	"TWOSIDED"	No
130	mu_FF_STAT_2016_2018_3_1	"HISTO"	"40"	"TWOSIDED"	No
131	el_FF_BTagged	"HISTO"	"40"	"TWOSIDED"	No
132	el_FF_AntiIDSF	"HISTO"	"40"	"TWOSIDED"	No
133	el_FF_STAT_2015_1_1	"HISTO"	"40"	"TWOSIDED"	No
134	el_FF_STAT_2015_2_1	"HISTO"	"40"	"TWOSIDED"	No
135	el_FF_STAT_2015_3_1	"HISTO"	"40"	"TWOSIDED"	No
136	el_FF_STAT_2015_1_2	"HISTO"	"40"	"TWOSIDED"	No
137	el_FF_STAT_2015_2_2	"HISTO"	"40"	"TWOSIDED"	No
138	el_FF_STAT_2015_3_2	"HISTO"	"40"	"TWOSIDED"	No
139	el_FF_STAT_2015_1_3	"HISTO"	"40"	"TWOSIDED"	No
140	el_FF_STAT_2015_2_3	"HISTO"	"40"	"TWOSIDED"	No
141	el_FF_STAT_2015_3_3	"HISTO"	"40"	"TWOSIDED"	No
142	el_FF_STAT_2015_2018_1_1	"HISTO"	"40"	"TWOSIDED"	No
143	el_FF_STAT_2015_2018_2_1	"HISTO"	"40"	"TWOSIDED"	No
144	el_FF_STAT_2015_2018_3_1	"HISTO"	"40"	"TWOSIDED"	No
145	el_FF_STAT_2015_2018_1_2	"HISTO"	"40"	"TWOSIDED"	No
146	el_FF_STAT_2015_2018_2_2	"HISTO"	"40"	"TWOSIDED"	No
147	el_FF_STAT_2015_2018_3_2	"HISTO"	"40"	"TWOSIDED"	No
148	el_FF_STAT_2015_2018_1_3	"HISTO"	"40"	"TWOSIDED"	No
149	el_FF_STAT_2015_2018_2_3	"HISTO"	"40"	"TWOSIDED"	No
150	el_FF_STAT_2015_2018_3_3	"HISTO"	"40"	"TWOSIDED"	No
151	el_FF_STAT_2016_2018_1_1	"HISTO"	"40"	"TWOSIDED"	No
152	el_FF_STAT_2016_2018_2_1	"HISTO"	"40"	"TWOSIDED"	No
153	el_FF_STAT_2016_2018_3_1	"HISTO"	"40"	"TWOSIDED"	No
154	el_FF_STAT_2016_2018_1_2	"HISTO"	"40"	"TWOSIDED"	No
155	el_FF_STAT_2016_2018_2_2	"HISTO"	"40"	"TWOSIDED"	No
156	el_FF_STAT_2016_2018_3_2	"HISTO"	"40"	"TWOSIDED"	No
157	el_FF_STAT_2016_2018_1_3	"HISTO"	"40"	"TWOSIDED"	No
158	el_FF_STAT_2016_2018_2_3	"HISTO"	"40"	"TWOSIDED"	No
159	el_FF_STAT_2016_2018_3_3	"HISTO"	"40"	"TWOSIDED"	No
160	chFlipSF	"HISTO"	"40"	"TWOSIDED"	No
161	MjjRewStat	"HISTO"	"40"	"TWOSIDED"	No
162	MjjRewScale	"HISTO"	"40"	"TWOSIDED"	No
163	MjjRewPDF	"HISTO"	"40"	"TWOSIDED"	No
164	WZQCD_PDFas	"HISTO"	"40"	"TWOSIDED"	Yes
165	WZQCD_scale	"HISTO"	"40"	"TWOSIDED"	Yes
166	LOMGSig_PDFas_EW	"HISTO"	"40"	"TWOSIDED"	Yes
167	LOMGSig_PDFas_QCD	"HISTO"	"40"	"TWOSIDED"	No
168	LOMGSig_PDFas_INT	"HISTO"	"40"	"TWOSIDED"	No
169	LOMGSig_scale_EW	"HISTO"	"40"	"TWOSIDED"	Yes
170	LOMGSig_scale_QCD	"HISTO"	"40"	"TWOSIDED"	No
171	LOMGSig_scale_INT	"HISTO"	"40"	"TWOSIDED"	No
172	LOMGSig_alt_PS_EW	"HISTO"	"40"	"ONESIDED"	Yes
173	LOMGSig_alt_PS_QCD	"HISTO"	"40"	"ONESIDED"	No
174	LOMGSig_alt_PS_INT	"HISTO"	"40"	"ONESIDED"	No
175	NLOEWQCD	"HISTO"	"40"	"ONESIDED"	No
176	GMH5_PDFs+ALPHAs	"HISTO"	"40"	"TWOSIDED"	Yes
177	GMH5_scale	"HISTO"	"40"	"TWOSIDED"	Yes
178	GMH5_NNLO_PDFs	"OVERALL"	No	No	No
179	GMH5_NNLO_ALPHAs	"OVERALL"	No	No	No
180	GMH5_NNLO_scale	"OVERALL"	No	No	No
181	GMH5_NLOEW	"OVERALL"	No	No	No
182	ZZXsec	"OVERALL"	No	No	No
183	TopXsec	"OVERALL"	No	No	No
184	VphotonXsec	"OVERALL"	No	No	No
185	TribosonXsec	"OVERALL"	No	No	No

C.3 Cross-check on the impact of the JES/JER systematics

This section investigates the impact of jet energy systematic uncertainties on the combined exclusion expected limits, aiming to offer more insight into the JES and JER incompatibility issue between the two channels entering the combination, as discussed in Section 7.2.1. We apply a methodical approach to evaluate the variations in the final combined exclusion expected limits by analysing four specific scenarios. The first scenario, referred to as `nominal`, considers the JES and JER uncertainties as uncorrelated between the channels. The next two scenarios, referred to as `NoJET_WZ` and `NoJET_ssWW`, individually exclude jet systematic uncertainties from the WZ and same-sign WW channels, respectively, thereby isolating the impact of a single variable. The final scenario, referred to as `NoJET_all`, assesses the consequences of concurrently removing jet systematic uncertainties from both channels. Each scenario is summarized as follows:

- **Scenario 1**: `Nominal`. Where all the JES and JER uncertainties are treated as uncorrelated between channels.
- **Scenario 2**: `NoJET_WZ`. Where all the JES and JER uncertainties are excluded in the WZ channel, comprising 31 terms.
- **Scenario 3**: `NoJET_ssWW`. Where all the JES and JER uncertainties are excluded in the same-sign WW channel, comprising 43 terms.
- **Scenario 4**: `NoJET_all`. Where all the JES and JER uncertainties are excluded simultaneously in both channels.

The specific uncertainty terms excluded are detailed in Table C.8.

The results presented in Tables C.4 and C.5 demonstrate the impact of excluding the jet energy systematic uncertainties on the combined exclusion expected limits for the different signal mass points in the various scenarios considered. These combined exclusion expected limits are obtained from TRExFitter directly, and do differ from the cross-section exclusion limits presented in Section 7.4 only by the application of constant factors. For completeness, similar results are provided for the combined exclusion expected limits on the

$\sin\theta_{\rm H}$ parameter of the GM model in Tables C.6 and C.7. The impact from the changes is smaller, by construction, on the GM limit results.

From the results, several important observations can be made:

- Including the jet energy uncertainties typically leads to an increase in the combined exclusion expected limit values for across the different mass points, as evidenced by Table C.4 (C.6 for the GM limits). This increase is consistent with expectations when systematic uncertainties are considered in the analysis.

- As detailed in Table C.5 (C.7 for the GM limits), the exclusion of jet energy uncertainties results in decreasing in limit values, with the magnitude of these decreases reaching up to approximately −3.0% (−1.5% for the GM limits) when uncertainties are removed from all channels.

- The jet energy uncertainties in the WZ channel have a more pronounced effect compared to those in the same-sign WW channel, often resulting in substantially greater impact when excluded, suggesting that the WZ uncertainties are more influential[1].

- The effect of excluding jet energy uncertainties on the combined exclusion expected limits varies with the mass point considered. For higher mass points, particularly those beyond 800 GeV, the relative differences are smaller, indicating a diminished sensitivity to jet energy uncertainties at these higher masses.

---

[1] There might be different reasons contributing to this behaviour. The tighter dijet mass cuts utilised in the same-sign WW regions definitions, the different correlation models for the JES and JER uncertainties (being more simplistic for the WZ channel), or the fact that the jet uncertainties are also propagated for the training of the ANN discriminant variable in the WZ analysis are some possible explanations for this higher sensitivity observed.

Table C.4: Combined exclusion expected limits obtained from TRExFitter for the 4 scenarios under study, namely: `Nominal`, `NoJET_WZ`, `NoJET_ssWW`, and `NoJET_all`.

m_{H_5} [GeV]	`Nominal`	`NoJET_WZ`	`NoJET_ssWW`	`NoJET_all`
200	0.080250	0.078882	0.079863	0.078547
225	0.097278	0.095873	0.096903	0.095552
250	0.101958	0.099833	0.101621	0.099564
275	0.109345	0.106188	0.109072	0.106019
300	0.115747	0.112928	0.115465	0.112747
325	0.107799	0.105159	0.107682	0.105096
350	0.113479	0.111127	0.113394	0.111095
375	0.111526	0.108935	0.111527	0.108969
400	0.111133	0.109273	0.111210	0.109367
425	0.111844	0.109863	0.111956	0.109976
450	0.120425	0.118729	0.120697	0.118860
475	0.117708	0.116827	0.117887	0.116997
500	0.119401	0.118043	0.119552	0.118188
525	0.101979	0.100999	0.102107	0.101118
550	0.107455	0.106311	0.107542	0.106387
600	0.116164	0.115184	0.116301	0.115307
700	0.130858	0.130061	0.130961	0.130140
800	0.138647	0.138066	0.138749	0.138146
900	0.662722	0.656110	0.663046	0.656337
1000	0.823648	0.821281	0.823950	0.821421

Table C.5: Relative differences in the combined exclusion expected limits obtained from TRExFitter in the `NoJET_WZ`, `NoJET_ssWW`, and `NoJET_all` scenarios with respect to those limits obtained in the `Nominal` scenario.

m_{H_5} [GeV]	`Nominal`	`NoJET_WZ`	`NoJET_ssWW`	`NoJET_all`
200	0.000%	-1.705%	-0.482%	-2.122%
225	0.000%	-1.444%	-0.386%	-1.774%
250	0.000%	-2.084%	-0.330%	-2.348%
275	0.000%	-2.887%	-0.249%	-3.042%
300	0.000%	-2.435%	-0.244%	-2.592%
325	0.000%	-2.449%	-0.109%	-2.507%
350	0.000%	-2.073%	-0.075%	-2.101%
375	0.000%	-2.324%	0.000%	-2.293%
400	0.000%	-1.674%	0.069%	-1.590%
425	0.000%	-1.772%	0.100%	-1.670%
450	0.000%	-1.408%	0.226%	-1.299%
475	0.000%	-0.748%	0.152%	-0.604%
500	0.000%	-1.138%	0.126%	-1.016%
525	0.000%	-0.961%	0.125%	-0.844%
550	0.000%	-1.064%	0.081%	-0.993%
600	0.000%	-0.843%	0.118%	-0.737%
700	0.000%	-0.610%	0.078%	-0.549%
800	0.000%	-0.419%	0.074%	-0.361%
900	0.000%	-0.998%	0.049%	-0.963%
1000	0.000%	-0.287%	0.037%	-0.270%

Table C.6: Combined exclusion expected limits on the $\sin\theta_{\mathrm{H}}$ parameter of the GM model for the 4 scenarios under study, namely: `Nominal`, `NoJET_WZ`, `NoJET_ssWW`, and `NoJET_all`.

m_{H_5} [GeV]	`Nominal`	`NoJET_WZ`	`NoJET_ssWW`	`NoJET_all`
200	0.141642	0.140429	0.141300	0.140131
225	0.155947	0.154817	0.155646	0.154558
250	0.159654	0.157982	0.159390	0.157769
275	0.165337	0.162933	0.165131	0.162803
300	0.170108	0.168024	0.169901	0.167889
325	0.164164	0.162141	0.164074	0.162093
350	0.168433	0.166678	0.168370	0.166655
375	0.166978	0.165026	0.166978	0.165052
400	0.166683	0.165282	0.166741	0.165353
425	0.167216	0.165728	0.167299	0.165813
450	0.173511	0.172285	0.173707	0.172381
475	0.171543	0.170900	0.171673	0.171024
500	0.172772	0.171787	0.172881	0.171893
525	0.159671	0.158901	0.159771	0.158996
550	0.163901	0.163027	0.163968	0.163085
600	0.170414	0.169694	0.170514	0.169785
700	0.180872	0.180320	0.180943	0.180374
800	0.186176	0.185786	0.186245	0.185840
900	0.203519	0.202502	0.203569	0.202537
1000	0.226888	0.226561	0.226929	0.226581

Table C.7: Relative differences in the combined exclusion expected limits on the $\sin\theta_{\mathrm{H}}$ parameter of the GM model in the `NoJET_WZ`, `NoJET_ssWW`, and `NoJET_all` scenarios with respect to those limits obtained in the `Nominal` scenario.

m_{H_5} [GeV]	`Nominal`	`NoJET_WZ`	`NoJET_ssWW`	`NoJET_all`
200	0.000%	-0.856%	-0.241%	-1.067%
225	0.000%	-0.725%	-0.193%	-0.891%
250	0.000%	-1.048%	-0.165%	-1.181%
275	0.000%	-1.454%	-0.125%	-1.533%
300	0.000%	-1.225%	-0.122%	-1.305%
325	0.000%	-1.232%	-0.055%	-1.262%
350	0.000%	-1.042%	-0.038%	-1.056%
375	0.000%	-1.169%	0.000%	-1.153%
400	0.000%	-0.840%	0.035%	-0.798%
425	0.000%	-0.890%	0.050%	-0.839%
450	0.000%	-0.707%	0.113%	-0.652%
475	0.000%	-0.375%	0.076%	-0.302%
500	0.000%	-0.570%	0.063%	-0.509%
525	0.000%	-0.482%	0.063%	-0.423%
550	0.000%	-0.533%	0.040%	-0.498%
600	0.000%	-0.422%	0.059%	-0.369%
700	0.000%	-0.305%	0.039%	-0.275%
800	0.000%	-0.210%	0.037%	-0.181%
900	0.000%	-0.500%	0.024%	-0.483%
1000	0.000%	-0.144%	0.018%	-0.135%

Table C.8: Jet energy uncertainties propagated through the WZ and same-sign WW channels.

WZ channel jet energy uncertainties	**Same-sign WW channel jet energy uncertainties**
WZsys_JET_BJES_Response	ssWWsys_JET_BJES_Response
WZsys_JET_EtaIntercalibration_Modelling	ssWWsys_JET_EtaIntercalibration_Modelling
WZsys_JET_EtaIntercalibration_NonClosure_2018data	ssWWsys_JET_EtaIntercalibration_NonClosure_highE
WZsys_JET_EtaIntercalibration_NonClosure_highE	ssWWsys_JET_EtaIntercalibration_NonClosure_negEta
WZsys_JET_EtaIntercalibration_NonClosure_negEta	ssWWsys_JET_EtaIntercalibration_NonClosure_posEta
WZsys_JET_EtaIntercalibration_NonClosure_posEta	ssWWsys_JET_EtaIntercalibration_TotalStat
WZsys_JET_EtaIntercalibration_TotalStat	ssWWsys_JET_Flavor_Composition
WZsys_JET_Flavor_Composition	ssWWsys_JET_Flavor_Response
WZsys_JET_Flavor_Response	ssWWsys_JET_Pileup_OffsetMu
WZsys_JET_Pileup_OffsetMu	ssWWsys_JET_Pileup_OffsetNPV
WZsys_JET_Pileup_OffsetNPV	ssWWsys_JET_Pileup_PtTerm
WZsys_JET_Pileup_PtTerm	ssWWsys_JET_Pileup_RhoTopology
WZsys_JET_Pileup_RhoTopology	ssWWsys_JET_PunchThrough_MC16
WZsys_JET_PunchThrough_MC16	ssWWsys_JET_SingleParticle_HighPt
WZsys_JET_SingleParticle_HighPt	ssWWsys_JET_EffectiveNP_Mixed1
WZsys_JET_EffectiveNP_1	ssWWsys_JET_EffectiveNP_Mixed2
WZsys_JET_EffectiveNP_2	ssWWsys_JET_EffectiveNP_Mixed3
WZsys_JET_EffectiveNP_3	ssWWsys_JET_EffectiveNP_Detector1
WZsys_JET_EffectiveNP_4	ssWWsys_JET_EffectiveNP_Detector2
WZsys_JET_EffectiveNP_5	ssWWsys_JET_EffectiveNP_Modelling1
WZsys_JET_EffectiveNP_6	ssWWsys_JET_EffectiveNP_Modelling2
WZsys_JET_EffectiveNP_7	ssWWsys_JET_EffectiveNP_Modelling3
WZsys_JET_EffectiveNP_8restTerm	ssWWsys_JET_EffectiveNP_Modelling4
WZsys_JET_JER_DataVsMC_MC16	ssWWsys_JET_EffectiveNP_Statistical1
WZsys_JET_JER_EffectiveNP_1	ssWWsys_JET_EffectiveNP_Statistical2
WZsys_JET_JER_EffectiveNP_2	ssWWsys_JET_EffectiveNP_Statistical3
WZsys_JET_JER_EffectiveNP_3	ssWWsys_JET_EffectiveNP_Statistical4
WZsys_JET_JER_EffectiveNP_4	ssWWsys_JET_EffectiveNP_Statistical5
WZsys_JET_JER_EffectiveNP_5	ssWWsys_JET_EffectiveNP_Statistical6
WZsys_JET_JER_EffectiveNP_6	ssWWsys_JET_JER_DataVsMC_MC16_PDsmear
WZsys_JET_JER_EffectiveNP_7restTerm	ssWWsys_JET_JER_DataVsMC_MC16_MCsmear
-	ssWWsys_JET_JER_EffectiveNP_1
-	ssWWsys_JET_JER_EffectiveNP_2
-	ssWWsys_JET_JER_EffectiveNP_3
-	ssWWsys_JET_JER_EffectiveNP_4
-	ssWWsys_JET_JER_EffectiveNP_5
-	ssWWsys_JET_JER_EffectiveNP_6
-	ssWWsys_JET_JER_EffectiveNP_7
-	ssWWsys_JET_JER_EffectiveNP_8
-	ssWWsys_JET_JER_EffectiveNP_9
-	ssWWsys_JET_JER_EffectiveNP_10
-	ssWWsys_JET_JER_EffectiveNP_11
-	ssWWsys_JET_JER_EffectiveNP_12restTerm

References

[1] ATLAS Collaboration. “Observation of a new particle in the search for the Standard Model Higgs boson with the ATLAS detector at the LHC”. In: *Phys. Lett. B* 716 (2012), p. 1. DOI: 10.1016/j.physletb.2012.08.020. arXiv: 1207.7214 [hep-ex].

[2] CMS Collaboration. “Observation of a New Boson at a Mass of 125 GeV with the CMS Experiment at the LHC”. In: *Phys. Lett. B* 716 (2012), pp. 30–61. DOI: 10.1016/j.physletb.2012.08.021. arXiv: 1207.7235 [hep-ex].

[3] ATLAS Collaboration. “A detailed map of Higgs boson interactions by the ATLAS experiment ten years after the discovery”. In: *Nature* 607 (2022), pp. 52–59. DOI: 10.1038/s41586-022-04893-w. arXiv: 2207.00092 [hep-ex].

[4] CMS Collaboration. “A portrait of the Higgs boson by the CMS experiment ten years after the discovery”. In: *Nature* 607 (2022), pp. 60–68. DOI: 10.1038/s41586-022-04892-x. arXiv: 2207.00043 [hep-ex].

[5] Asher Berlin, Tongyan Lin, and Lian-Tao Wang. “Mono-Higgs detection of dark matter at the LHC”. In: *Journal of High Energy Physics* 2014.6 (2014), p. 78. DOI: 10.1007/JHEP06(2014)078. URL: https://doi.org/10.1007/JHEP06(2014)078.

[6] Tomohiro Abe et al. “LHC Dark Matter Working Group: Next-generation spin-0 dark matter models”. In: *Phys. Dark Univ.* 27 (2020), p. 100351. DOI: 10.1016/j.dark.2019.100351. arXiv: 1810.09420 [hep-ex].

[7] Martin Bauer, Ulrich Haisch, and Felix Kahlhoefer. “Simplified dark matter models with two Higgs doublets: I. Pseudoscalar mediators”. In: *Journal of High Energy Physics* 2017.5 (2017), p. 138. DOI: 10.1007/JHEP05(2017)138. URL: https://doi.org/10.1007/JHEP05(2017)138.

[8] John F. Gunion and Chris Hays. “Higgs triplets”. In: *Meeting on CP Violation and Non-standard Higgs Physics*. 2006, pp. 497–526. DOI: 10.5170/CERN-2006-009.497.

[9] T. D. Lee. “A Theory of Spontaneous T Violation”. In: *Phys. Rev. D* 8 (1973), p. 1226. DOI: 10.1103/PhysRevD.8.1226.

[10] P. Fayet. “A gauge theory of weak and electromagnetic interactions with spontaneous parity breaking”. In: *Nucl. Phys. B* 78 (1974), p. 14. DOI: 10.1016/0550-3213(74)90113-8.

[11] Rabindra N. Mohapatra and Jogesh C. Pati. “Left-right gauge symmetry and an “isoconjugate” model of CP violation”. In: *Phys. Rev. D* 11 (1975), pp. 566–571. DOI: 10.1103/PhysRevD.11.566.

[12] N. Arkani-Hamed et al. "The Littlest Higgs". In: *JHEP* 07 (2002), p. 034. DOI: 10.1088/1126-6708/2002/07/034. arXiv: hep-ph/0206021.

[13] Tao Han et al. "Phenomenology of the little Higgs model". In: *Phys. Rev. D* 67 (2003), p. 095004. DOI: 10.1103/PhysRevD.67.095004. arXiv: hep-ph/0301040.

[14] Christoph Englert, Emanuele Re, and Michael Spannowsky. "Pinning down Higgs triplets at the LHC". In: *Phys. Rev. D* 88 (2013), p. 035024. DOI: 10.1103/PhysRevD.88.035024. arXiv: 1306.6228 [hep-ph].

[15] Howard Georgi and Marie Machacek. "Doubly charged Higgs bosons". In: *Nucl. Phys. B* 262 (1985), pp. 463–477. DOI: 10.1016/0550-3213(85)90325-6.

[16] Michael S. Chanowitz and Mitchell Golden. "Higgs boson triplets with $M_\mathrm{W} = M_\mathrm{Z} \cos\theta_\mathrm{W}$". In: *Phys. Lett. B* 165 (1985), pp. 105–108. DOI: 10.1016/0370-2693(85)90700-2.

[17] Katy Hartling, Kunal Kumar, and Heather E. Logan. "Indirect constraints on the Georgi-Machacek model and implications for Higgs boson couplings". In: *Phys. Rev. D* 91.1 (2015), p. 015013. DOI: 10.1103/PhysRevD.91.015013. arXiv: 1410.5538 [hep-ph].

[18] Ben Keeshan, Heather E. Logan, and Terry Pilkington. "Custodial symmetry violation in the Georgi-Machacek model". In: *Phys. Rev. D* 102.1 (2020), p. 015001. DOI: 10.1103/PhysRevD.102.015001. arXiv: 1807.11511 [hep-ph].

[19] ATLAS Collaboration. "Luminosity determination in pp collisions at $\sqrt{s} = 13$ TeV using the ATLAS detector at the LHC". In: *Eur. Phys. J. C* 83 (2023), p. 982. DOI: https://doi.org/10.1140/epjc/s10052-023-11747-w. arXiv: 2212.09379 [hep-ex].

[20] ATLAS Collaboration. "The new LUCID-2 detector for luminosity measurement and monitoring in ATLAS". In: *JINST* 13 (2018), P07017. DOI: https://doi.org/10.1088/1748-0221/13/07/P07017.

[21] Wikimedia Commons Contributors. *Standard Model of Elementary Particles*. Accessed: December 10, 2024. 2018. URL: https://en.wikipedia.org/wiki/File:Standard_Model_of_Elementary_Particles.svg.

[22] David J Griffiths. *Introduction to elementary particles; 2nd rev. version*. Physics textbook. New York, NY: Wiley, 2008. URL: https://cds.cern.ch/record/111880.

[23] Torbjorn Sjostrand, Stephen Mrenna, and Peter Z. Skands. "A Brief Introduction to PYTHIA 8.1". In: *Comput. Phys. Commun.* 178 (2008), p. 852. DOI: 10.1016/j.cpc.2008.01.036. arXiv: 0710.3820.

[24] Peter W. Higgs. "Broken Symmetries and the Masses of Gauge Bosons". In: *Phys. Rev. Lett.* 13 (16 Oct. 1964), pp. 508–509. DOI: 10.1103/PhysRevLett.13.508. URL: https://link.aps.org/doi/10.1103/PhysRevLett.13.508.

[25] Howard Georgi and Marie Machacek. "Doubly charged Higgs bosons". In: *Nuclear Physics B* 262.3 (1985), pp. 463–477. ISSN: 0550-3213. DOI: https://doi.org/10.1016/0550-3213(85)90325-6. URL: https://www.sciencedirect.com/science/article/pii/0550321385903256.

[26] Michael S. Chanowitz and Mitchell Golden. “Higgs boson triplets with Mw=Mzcosθw”. In: *Physics Letters B* 165.1 (1985), pp. 105–108. ISSN: 0370-2693. DOI: https://doi.org/10.1016/0370-2693(85)90700-2. URL: https://www.sciencedirect.com/science/article/pii/0370269385907002.

[27] Katy Hartling, Kunal Kumar, and Heather E. Logan. “The decoupling limit in the Georgi-Machacek model”. In: *Physical Review D* 90.1 (July 2014). ISSN: 1550-2368. DOI: 10.1103/physrevd.90.015007. URL: http://dx.doi.org/10.1103/PhysRevD.90.015007.

[28] Heather E. Logan. *Lectures on perturbative unitarity and decoupling in Higgs physics.* 2022. arXiv: 2207.01064 [hep-ph]. URL: https://arxiv.org/abs/2207.01064.

[29] Heather E. Logan. *TASI 2013 lectures on Higgs physics within and beyond the Standard Model.* 2022. arXiv: 1406.1786 [hep-ph]. URL: https://arxiv.org/abs/1406.1786.

[30] K. A. Olive et al. “Review of Particle Physics”. In: *Chin. Phys. C* 38 (2014), p. 090001. DOI: 10.1088/1674-1137/38/9/090001.

[31] Heather E. Logan and Mark B. Reimer. “Characterizing a benchmark scenario for heavy Higgs boson searches in the Georgi-Machacek model”. In: *Phys. Rev. D* 96.9 (2017), p. 095029. DOI: 10.1103/PhysRevD.96.095029. arXiv: 1709.01883 [hep-ph].

[32] Esma Mobs. *The CERN accelerator complex - 2019. Complexe des accélérateurs du CERN - 2019.* General Photo. July 2019. URL: https://cds.cern.ch/record/2684277.

[33] Joao Pequenao. “Computer generated image of the whole ATLAS detector”. 2008. URL: https://cds.cern.ch/record/1095924.

[34] Giles Strong. “On the impact of selected modern deep-learning techniques to the performance and celerity of classification models in an experimental high-energy physics use case”. In: *Machine Learning: Science and Technology* 1 (Sept. 2020). DOI: 10.1088/2632-2153/ab983a.

[35] ATLAS Collaboration. “Experiment Briefing: Keeping the ATLAS Inner Detector in perfect alignment”. 2020. URL: https://cds.cern.ch/record/2723878.

[36] Joao Pequenao. “Computer Generated image of the ATLAS calorimeter”. 2008. URL: https://cds.cern.ch/record/1095927.

[37] Joao Pequenao. “Computer generated image of the ATLAS Muons subsystem”. 2008. URL: https://cds.cern.ch/record/1095929.

[38] Lyndon Evans and Lyn Evans. *The Large Hadron Collider: a marvel of technology; 2nd ed.* Physics (EPFL Press). On the cover : Including the discovery of the higgs boson. Lausanne: EPFL Press, 2018. URL: https://cds.cern.ch/record/2645935.

[39] ATLAS Collaboration. “Operation of the ATLAS trigger system in Run 2”. In: *Journal of Instrumentation* 15.10 (Oct. 2020), P10004. DOI: 10.1088/1748-0221/15/10/P10004. URL: https://dx.doi.org/10.1088/1748-0221/15/10/P10004.

[40] CERN High-Luminosity LHC Project. *The High-Luminosity LHC Project*. Online. Accessed: 2024-11-19. 2024. URL: https://hilumilhc.web.cern.ch/content/hl-lhc-project.

[41] O. Aberle et al. *High-Luminosity Large Hadron Collider (HL-LHC): Technical Design Report*. CERN Yellow Reports: Monographs. Geneva: CERN, 2020. DOI: 10.23731/CYRM-2020-0010. URL: https://cds.cern.ch/record/2749422.

[42] ATLAS Collaboration et al. *Expected tracking and related performance with the updated ATLAS Inner Tracker layout at the High-Luminosity LHC*. Tech. rep. All figures including auxiliary figures are available at https://atlas.web.cern.ch/Atlas/GROUPS/PHYSICS/PU
PHYS-PUB-2021-024. Geneva: CERN, 2021. URL: https://cds.cern.ch/record/2771992.

[43] Collaboration ATLAS. *Technical Design Report for the Phase-II Upgrade of the ATLAS Trigger and Data Acquisition System - Event Filter Tracking Amendment*. Tech. rep. Geneva: CERN, 2022. DOI: 10.17181/CERN.ZK85.5TDL. URL: https://cds.cern.ch/record/2802799.

[44] NVIDIA Corporation. *Triton Inference Server: An Optimized Cloud and Edge Inferencing Solution*. https://github.com/triton-inference-server. If you use this software, please cite it as below. 2024.

[45] The Acts Team. *Tracking in a nutshell*. Accessed: December 10, 2024. 2024. URL: https://acts.readthedocs.io/en/latest/tracking.html.

[46] The ATLAS collaboration. *Expected tracking and related performance with the updated ATLAS Inner Tracker layout at the High-Luminosity LHC*. ATL-PHYS-PUB-2021-024. 2021. URL: https://cds.cern.ch/record/2776651.

[47] The ATLAS collaboration. *Development of ATLAS Primary Vertex Reconstruction for LHC Run 3*. ATL-PHYS-PUB-2019-015. 2019. URL: https://cds.cern.ch/record/2670380.

[48] ATLAS Collaboration. *EGamma Recommendations for R21*. https://twiki.cern.ch/twiki/bin/view/AtlasProtected/EGammaRecommendationsR21.

[49] ATLAS Collaboration. "Muon reconstruction performance of the ATLAS detector in proton–proton collision data at $\sqrt{s} = 13\,\text{TeV}$". In: *Eur. Phys. J. C* 76 (2016), p. 292. DOI: 10.1140/epjc/s10052-016-4120-y. arXiv: 1603.05598 [hep-ex].

[50] ATLAS Collaboration. "Muon reconstruction and identification efficiency in ATLAS using the full Run 2 pp collision data set at $\sqrt{s} = 13\,\text{TeV}$". In: (2020). arXiv: 2012.00578 [hep-ex].

[51] Eric M. Metodiev. *The Fractal Lives of Jets*. Accessed: December 10, 2024. 2020. URL: https://www.ericmetodiev.com/post/jetformation/.

[52] ATLAS Collaboration. "The anti-k_t jet clustering algorithm". In: *JHEP* 04 (2008), p. 063. DOI: https://doi.org/10.1088/1126-6708/2008/04/063. arXiv: 0802.1189 [hep-ph].

[53] ATLAS Collaboration. "Jet energy scale and resolution measured in proton–proton collisions at $\sqrt{s} = 13$ TeV with the ATLAS detector". In: *Eur. Phys. J. C* 81 (2021), p. 689. DOI: `https://doi.org/10.1140/epjc/s10052-021-09402-3`. arXiv: `2007.02645 [hep-ex]`.

[54] ATLAS Collaboration. "ATLAS b-jet identification performance and efficiency measurement with $t\bar{t}$ events in pp collisions at $\sqrt{s} = 13\,\text{TeV}$". In: *Eur. Phys. J. C* 79 (2019), p. 970. DOI: `10.1140/epjc/s10052-019-7450-8`. arXiv: `1907.05120 [hep-ex]`.

[55] ATLAS Collaboration. *Measurement of the b-jet identification efficiency for high transverse momentum jets in $t\bar{t}$ events in the lepton + jets channel with the ATLAS detector using Run 2 data.* ATL-PHYS-PUB-2021-004. 2021. URL: `https://cds.cern.ch/record/2753734`.

[56] ATLAS Collaboration. *Pileup jet recommendations.* `https://twiki.cern.ch/twiki/bin/viewauth/AtlasProtected/PileupJetRecommendations`.

[57] ATLAS Collaboration. "Performance of pile-up mitigation techniques for jets in pp collisions at $\sqrt{s} = 8$ TeV using the ATLAS detector". In: *Eur. Phys. J. C* 76 (2016), p. 581. DOI: `https://doi.org/10.1140/epjc/s10052-016-4395-z`. arXiv: `1510.03823 [hep-ex]`.

[58] ATLAS Collaboration. "Identification and rejection of pile-up jets at high pseudorapidity with the ATLAS detector". In: *Eur. Phys. J. C* 77 (2017), p. 580. DOI: `https://doi.org/10.1140/epjc/s10052-017-5081-5`. arXiv: `1705.02211 [hep-ex]`.

[59] ATLAS. *Small-R (R=0.4) jet energy scale and jet energy resolution uncertainties for full run 2 analyses (release 21).* 2022. URL: `https://twiki.cern.ch/twiki/bin/view/AtlasProtected/JetUncertaintiesRel21Summer2018SmallR`.

[60] ATLAS Collaboration. *Overlap Removal Tools.* `https://indico.cern.ch/event/631313/contributions/2683959/attachments/1518878/2373377/Farrell_ORTools_ftaghbb.pdf`.

[61] ATLAS Collaboration. *Overlap Removal Tools git repository.* `https://gitlab.cern.ch/atlas/athena/tree/21.2/PhysicsAnalysis/AnalysisCommon/AssociationUtils`.

[62] ATLAS Collaboration. *LuminosityForPhysics.* `https://twiki.cern.ch/twiki/bin/view/Atlas/LuminosityForPhysics`. Accessed: 2024-04-07. Section: 2015 - 2018 13 TeV proton-proton (final).

[63] ATLAS Collaboration. *GoodRunListsForAnalysisRun2.* `https://twiki.cern.ch/twiki/bin/viewauth/AtlasProtected/GoodRunListsForAnalysisRun2`.

[64] PhysicsModellingGroup. *PmgJetAndPhotonProcesses.* Accessed: December 17, 2024. 2020. URL: `https://twiki.cern.ch/twiki/bin/viewauth/AtlasProtected/PmgJetAndPhotonProcesses#Process_specific_uncertainties`.

[65] ATLAS Collaboration. "Performance and calibration of quark/gluon-jet taggers using 140 fb^{-1} of pp collisions at $\sqrt{s} = 13$ TeV with the ATLAS detector". In: *Chinese Physics C* 48.2 (Feb. 2024), p. 023001. DOI: `10.1088/1674-1137/acf701`. URL: `https://dx.doi.org/10.1088/1674-1137/acf701`.

[66] ATLAS Collaboration. "The ATLAS Simulation Infrastructure". In: *Eur. Phys. J. C* 70 (2010), p. 823. DOI: `10.1140/epjc/s10052-010-1429-9`. arXiv: `1005.4568 [physics.ins-det]`.

[67] S. Agostinelli et al. "GEANT4 – a simulation toolkit". In: *Nucl. Instrum. Meth. A* 506 (2003), p. 250. DOI: `10.1016/S0168-9002(03)01368-8`.

[68] Torbjorn Sjöstrand, Stephen Mrenna, and Peter Z. Skands. "A brief introduction to PYTHIA 8.1". In: *Comput. Phys. Commun.* 178 (2008), pp. 852–867. DOI: `10.1016/j.cpc.2008.01.036`. arXiv: `0710.3820 [hep-ph]`.

[69] Richard D. Ball et al. "Parton distributions with LHC data". In: *Nucl. Phys. B* 867 (2013), p. 244. DOI: `10.1016/j.nuclphysb.2012.10.003`. arXiv: `1207.1303 [hep-ph]`.

[70] ATLAS Collaboration. *The Pythia 8 A3 tune description of ATLAS minimum bias and inelastic measurements incorporating the Donnachie–Landshoff diffractive model*. ATL-PHYS-PUB-2016-017. 2016. URL: `https://cds.cern.ch/record/2206965`.

[71] *VBF GM NLO signal samples for WZ Analysis*. `https://its.cern.ch/jira/browse/ATLMCPROD-7487`.

[72] *Request for new GM NLO samples, H5 -¿ WZ -¿ lvll*. `https://its.cern.ch/jira/browse/ATLMCPROD-8753`.

[73] *H++ samples for interpretation in ssWWjj analysis*. `https://its.cern.ch/jira/browse/ATLMCPROD-9798`.

[74] D. de Florian et al. *Handbook of LHC Higgs Cross Sections: 4. Deciphering the Nature of the Higgs Sector*. CERN-2017-002-M. 2017. DOI: `10.23731/CYRM-2017-002`. arXiv: `1610.07922 [hep-ph]`.

[75] T. Gleisberg et al. "Event generation with SHERPA 1.1". In: *JHEP* 02 (2009), p. 007. DOI: `10.1088/1126-6708/2009/02/007`. arXiv: `0811.4622 [hep-ph]`.

[76] ATLAS Collaboration. *ATLAS Pythia 8 tunes to 7 TeV data*. ATL-PHYS-PUB-2014-021. 2014. URL: `https://cds.cern.ch/record/1966419`.

[77] Enrico Bothmann et al. "Event generation with Sherpa 2.2". In: *SciPost Phys.* 7.3 (2019), p. 034. DOI: `10.21468/SciPostPhys.7.3.034`. arXiv: `1905.09127 [hep-ph]`.

[78] J. Alwall et al. "The automated computation of tree-level and next-to-leading order differential cross sections, and their matching to parton shower simulations". In: *JHEP* 07 (2014), p. 079. DOI: `10.1007/JHEP07(2014)079`. arXiv: `1405.0301 [hep-ph]`.

[79] ATLAS Collaboration. "Search for resonant WZ production in the fully leptonic final state in proton–proton collisions at $\sqrt{s} = 13$ TeV with the ATLAS detector". In: *Eur. Phys. J. C* 83 (2023), p. 633. DOI: `10.1140/epjc/s10052-023-11437-7`. arXiv: `2207.03925 [hep-ex]`.

[80] Pierre Artoisenet et al. “Automatic spin-entangled decays of heavy resonances in Monte Carlo simulations”. In: *JHEP* 03 (2013), p. 015. DOI: `10.1007/JHEP03(2013)015`. arXiv: `1212.3460 [hep-ph]`.

[81] ATLAS Collaboration. “Measurement and interpretation of same-sign W boson pair production in association with two jets in pp collisions at $\sqrt{s}$ = 13 TeV with the ATLAS detector”. In: *JHEP* 04 (2024), p. 026. DOI: `https://doi.org/10.1007/JHEP04(2024)026`. arXiv: `2312.00420 [hep-ex]`.

[82] ATLAS Collaboration. “Search for new resonances in mass distributions of jet pairs using 139 fb^{-1} of pp collisions at $\sqrt{s} = 13$ TeV with the ATLAS detector”. In: *JHEP* 03 (2020), p. 145. DOI: `10.1007/JHEP03(2020)145`. arXiv: `1910.08447 [hep-ex]`.

[83] Albert M Sirunyan et al. “Electroweak production of two jets in association with a Z boson in proton–proton collisions at $\sqrt{s} = 13$ TeV”. In: *Eur. Phys. J. C* 78.7 (2018), p. 589. DOI: `10.1140/epjc/s10052-018-6049-9`. arXiv: `1712.09814 [hep-ex]`.

[84] ATLAS Collaboration. “Search for the Standard Model Higgs boson produced by vector-boson fusion and decaying to bottom quarks in $\sqrt{s} = 8$ TeV pp collisions with the ATLAS detector”. In: *JHEP* 11 (2016), p. 112. DOI: `10.1007/JHEP11(2016)112`. arXiv: `1606.02181 [hep-ex]`.

[85] ATLAS Collaboration. “Search for dijet resonances in events with an isolated charged lepton using $\sqrt{s} = 13$ TeV proton–proton collision data collected by the ATLAS detector”. In: *JHEP* 06 (2020), p. 151. DOI: `10.1007/JHEP06(2020)151`. arXiv: `2002.11325 [hep-ex]`.

[86] CMS Collaboration. “Search for high mass dijet resonances with a new background prediction method in proton–proton collisions at $\sqrt{s} = 13$ TeV”. In: *JHEP* 05 (2020), p. 033. DOI: `10.1007/JHEP05(2020)033`. arXiv: `1911.03947 [hep-ex]`.

[87] CMS Collaboration. “Search for new physics in multijet events with at least one photon and large missing transverse momentum in proton–proton collisions at 13 TeV”. In: (2023). arXiv: `2307.16216 [hep-ex]`.

[88] ATLAS Collaboration. “Search for R-parity-violating supersymmetric particles in multi-jet final states produced in pp collisions at $\sqrt{s} = 13$ TeV using the ATLAS detector at the LHC”. In: *Phys. Lett. B* 785 (2018), p. 136. DOI: `10.1016/j.physletb.2018.08.021`. arXiv: `1804.03568 [hep-ex]`.

[89] CMS Collaboration. “Search for top squarks in final states with two top quarks and several light-flavor jets in proton–proton collisions at $\sqrt{s} = 13$ TeV”. In: (2021). arXiv: `2102.06976 [hep-ex]`.

[90] ATLAS Collaboration. “Jet energy scale and resolution measured in proton–proton collisions at $\sqrt{s} = 13$ TeV with the ATLAS detector”. In: (2020). arXiv: `2007.02645 [hep-ex]`.

[91] Guolin Ke et al. “LightGBM: A Highly Efficient Gradient Boosting Decision Tree”. In: *Advances in Neural Information Processing Systems 30 (NIPS 2017)*. Curran Associates, Inc. URL: `https://proceedings.neurips.cc/paper_files/paper/2017/file/6449f44a102fde848669bdd9eb6b76fa-Paper.pdf`.

[92] Takuya Akiba et al. *Optuna: A Next-generation Hyperparameter Optimization Framework*. 2019. arXiv: 1907.10902 [cs.LG].

[93] ATLAS Collaboration. *Constituent-Based Quark Gluon Tagging using Transformers with the ATLAS detector*. Tech. rep. All figures including auxiliary figures are available at https://atlas.web.cern.ch/Atlas/GROUPS/PHYSICS/PUBNOTES/ATL-PHYS-PUB-2023-032. Geneva: CERN, 2023. URL: https://cds.cern.ch/record/2878932.

[94] François Chollet et al. *Keras*. 2015. URL: https://keras.io.

[95] Martín Abadi et al. *TensorFlow: Large-Scale Machine Learning on Heterogeneous Distributed Systems*. 2016. arXiv: 1603.04467 [cs.DC]. URL: https://arxiv.org/abs/1603.04467.

[96] ATLAS Collaboration. "Electron and photon performance measurements with the ATLAS detector using the 2015–2017 LHC proton-proton collision data". In: *JINST* 14 (2019), P12006. DOI: https://doi.org/10.1088/1748-0221/14/12/P12006. arXiv: 1908.00005 [hep-ex].

[97] ATLAS Collaboration. "Muon reconstruction and identification efficiency in ATLAS using the full Run 2 pp collision data set at $\sqrt{s} = 13$ TeV". In: *Eur. Phys. J. C* 81 (2021), p. 578. DOI: https://doi.org/10.1140/epjc/s10052-021-09233-2. arXiv: 2012.00578 [hep-ex].

[98] ATLAS Collaboration. "Performance of electron and photon triggers in ATLAS during LHC Run 2". In: *Eur. Phys. J. C* 80 (2020), p. 47. DOI: https://doi.org/10.1140/epjc/s10052-019-7500-2. arXiv: 1909.00761 [hep-ex].

[99] ATLAS Collaboration. "Performance of the ATLAS muon triggers in Run 2". In: *JINST* 15 (2020), P09015. DOI: https://doi.org/10.1088/1748-0221/15/09/P09015. arXiv: 2004.13447 [hep-ex].

[100] ATLAS Collaboration. "Performance of missing transverse momentum reconstruction with the ATLAS detector using proton–proton collisions at $\sqrt{s} = 13$ TeV". In: *Eur. Phys. J. C* 78 (2018), p. 903. DOI: https://doi.org/10.48550/arXiv.1802.08168. arXiv: 1802.08168 [hep-ex].

[101] ATLAS Collaboration. *Optimisation and performance studies of the ATLAS b-tagging algorithms for the 2017-18 LHC run*. ATL-PHYS-PUB-2017-013. 2017. URL: https://cds.cern.ch/record/2273281.

[102] Benedikt Biedermann, Ansgar Denner, and Mathieu Pellen. "Complete NLO corrections to W^+W^+ scattering and its irreducible background at the LHC". In: *JHEP* 10 (2017), p. 124. DOI: 10.1007/JHEP10(2017)124. arXiv: 1708.00268 [hep-ph].

[103] ATLAS Collaboration. *Multi-Boson Simulation for* 13 *TeV ATLAS Analyses*. ATL-PHYS-PUB-2017-005. 2017. URL: https://cds.cern.ch/record/2261933.

[104] ATLAS Collaboration. *Multi-boson simulation for* 13 *TeV ATLAS analyses*. ATL-PHYS-PUB-2016-002. 2016. URL: https://cds.cern.ch/record/2119986.

[105] ATLAS Collaboration. “Measurement of the $t\bar{t}Z$ and $t\bar{t}W$ cross sections in proton-proton collisions at $\sqrt{s} = 13$ TeV with the ATLAS detector”. In: *Phys. Rev. D* 99 (2019), p. 072009. DOI: https://doi.org/10.1103/PhysRevD.99.072009. arXiv: 1901.03584 [hep-ex].

[106] ATLAS Collaboration. “Evidence for the production of three massive vector bosons with the ATLAS detector”. In: *Physics Letters B* 798 (2019), p. 134913. DOI: https://doi.org/10.1016/j.physletb.2019.134913. arXiv: 1903.10415 [hep-ex].

[107] ATLAS Collaboration. “Measurements of the inclusive and differential production cross sections of a top-quark–antiquark pair in association with a Z boson at $\sqrt{s} = 13$ TeV with the ATLAS detector”. In: *Eur. Phys. J. C* 81 (2021), p. 737. DOI: https://doi.org/10.1140/epjc/s10052-021-09439-4. arXiv: 2103.12603 [hep-ex].

[108] Glen Cowan et al. “Asymptotic formulae for likelihood-based tests of new physics”. In: *The European Physical Journal C* 71.2 (Feb. 2011). ISSN: 1434-6052. DOI: 10.1140/epjc/s10052-011-1554-0. URL: http://dx.doi.org/10.1140/epjc/s10052-011-1554-0.

[109] Alexander L. Read. “Presentation of search results: The CL(s) technique”. In: *J. Phys. G* 28 (2002), p. 2693. DOI: 10.1088/0954-3899/28/10/313.

[110] ATLAS Collaboration. *The TRExFitter framework*. https://trexfitter-docs.web.cern.ch/trexfitter-docs/.

[111] Eilam Gross and Ofer Vitells. “Trial factors for the look elsewhere effect in high energy physics”. In: *Eur. Phys. J. C* 70 (2010), pp. 525–530. DOI: 10.1140/epjc/s10052-010-1470-8. arXiv: 1005.1891 [hep-ex].

[112] CMS Collaboration. “Search for charged Higgs bosons produced in vector boson fusion processes and decaying into vector boson pairs in proton–proton collisions at $\sqrt{s} = 13\,\text{TeV}$”. In: (2021). arXiv: 2104.04762 [hep-ex].

[113] CMS Collaboration. “Search for charged Higgs bosons produced in vector boson fusion processes and decaying into vector boson pairs in proton–proton collisions at $\sqrt{s} = 13$ TeV”. In: *Eur. Phys. J. C* 81 (2021), p. 723. DOI: https://doi.org/10.1140/epjc/s10052-021-09472-3. arXiv: 2104.04762 [hep-ex].

[114] CMS Collaboration. *HEPData for the CMS charged Higgs analysis*. https://www.hepdata.net/record/ins1857811.

[115] Antonio Giannini. *VBF RNN tagger*. Accessed: December 10, 2024. 2024. URL: https://indico.cern.ch/event/1430931/contributions/6047625/attachments/2898545/5082402/VBFTagger_DBL_17Jul24.pdf.

[116] Georges Aad et al. “Performance and calibration of quark/gluon-jet taggers using 140 fb^{-1} of pp collisions at TeV with the ATLAS detector*”. In: *Chin. Phys. C* 48.2 (2024), p. 023001. DOI: 10.1088/1674-1137/acf701. arXiv: 2308.00716 [hep-ex].

[117] H. Zhao et. "Combination of searches for singly and doubly charged Higgs bosons produced via vector-boson fusion in proton–proton collisions at s=13 TeV with the ATLAS detector". In: *Physics Letters B* 860 (2025), p. 139137. ISSN: 0370-2693. DOI: `https://doi.org/10.1016/j.physletb.2024.139137`. URL: `https://www.sciencedirect.com/science/article/pii/S0370269324006956`.

[118] Xiangyang Ju et al. *Graph Neural Networks for Particle Reconstruction in High Energy Physics detectors*. 2020. arXiv: `2003.11603 [physics.ins-det]`. URL: `https://arxiv.org/abs/2003.11603`.

[119] Haoran Zhao et al. *Graph Neural Network-based Tracking as a Service*. 2024. arXiv: `2402.09633 [physics.comp-ph]`. URL: `https://arxiv.org/abs/2402.09633`.

[120] Haoran Zhao et al. *Track reconstruction as a service for collider physics*. 2025. arXiv: `2501.05520 [physics.ins-det]`. URL: `https://arxiv.org/abs/2501.05520`.

[121] The ATLAS collaboration. *Reconstruction of primary vertices at the ATLAS experiment in Run 1 proton–proton collisions at the LHC*. 2017. URL: `https://link.springer.com/article/10.1140/epjc/s10052-017-4887-5`.

[122] *ATLAS HL-LHC Computing Conceptual Design Report*. Tech. rep. Geneva: CERN, 2020. URL: `https://cds.cern.ch/record/2729668`.

[123] CMS Offline Software and Computing. *CMS Phase-2 Computing Model: Update Document*. Tech. rep. Geneva: CERN, 2022. URL: `https://cds.cern.ch/record/2815292`.

[124] K. Edmonds et al. "The fast ATLAS track simulation (FATRAS)". In: (Mar. 2008).

[125] Christian Bierlich et al. "A comprehensive guide to the physics and usage of PYTHIA 8.3". In: *SciPost Phys. Codeb.* 2022 (2022), p. 8. DOI: `10.21468/SciPostPhysCodeb.8`. arXiv: `2203.11601 [hep-ph]`.